ISSN 2432-8375

BULLETIN OF THE
LABORATORY FOR ADVANCED NUCLEAR ENERGY

VOL. 1 2016

LABORATORY FOR ADVANCED NUCLEAR ENERGY
INSTITUTE OF INNOVATIVE RESEARCH
TOKYO INSTITUTE OF TECHNOLOGY

BULLETIN OF THE LABORATORY FOR ADVANCED NUCLEAR ENERGY

(Formerly, BULLETIN OF THE RESEARCH LABORATORY
FOR NUCLEAR REACTORS)

Editor: *Toyohiko YANO*
Editorial Board: *Yukitaka KATO*
Hiroaki TSUTSUI and
Hiroshi SAGARA

Abbreviation of the ”**BULLETIN OF THE LABORATORY FOR ADVANCED NUCLEAR ENERGY**” is BULL. LAB. ADV. NUCL. ENERGY

All communications should be addressed to the editor, Laboratory for Advanced Nuclear Energy, Institute of Innovative Research, Tokyo Institute of Technology (Tokyo Kogyo Daigaku),
2-12-1-N1-16, O-okayama, Meguro-ku, Tokyo 152-8550, Japan.

TEL. +81-3-5734-3052, FAX. +81-3-5734-2959, E-mail bulletin@lane.iir.titech.ac.jp

http://www.lane.iir.titech.ac.jp/

BULLETIN OF THE LABORATORY FOR ADVANCED NUCLEAR ENERGY

BULL. LAB. ADV. NUCL. ENERGY, Vol.1, 2016

CONTENTS

D. Advanced Medical Application Division

E. Fundamental Research Division

III. Co-operative Researches

Research staffs of
THE LABORATORY FOR ADVANCED NUCLEAR ENERGY, TOKYO INSTITUTE OF TECHONOGY
AS OF 2016 JAPANESE FISCAL YEAR

Director

Toyohiko YANO	Professor

Innovative Nuclear Energy System Division

Masayuki IGASHIRA	Professor
Toru OBARA	Professor
Yukitaka KATO	Professor
Yoshinao KOBAYASHI	Professor
Minoru TAKAHASHI	Professor
Tatsuya KATABUCHI	Associate Professor
Hiroshige KIKURA	Associate Professor
Masatoshi KONDO	Assistant Professor
Jun NISHIYAMA	Assistant Professor

Actinide Management Division

Kenji TAKESHITA	Professor
Koichiro TAKAO	Associate Professor
Takehiko TSUKAHARA	Associate Professor
Masayuki HARADA	Assistant Professor

Global Nuclear Security Division

Toshihiko OHNUKI	Professor
Osamu ODAWARA	Professor
Toyohiko YANO	Professor
Hiroshi SAGARA	Associate Professor
Katsumi YOSHIDA	Associate Professor
Tetsuo SAWADA	Assistant Professor
Anna Gubarevich	Assistant Professor

Advanced Medical Application Division

Yoshiyuki OGURI	Professor
Noriyosu HAYASHIZAKI	Associate Professor
Yoshihisa MATSUMOTO	Associate Professor
Mikio SHIMADA	Assistant Professor

Fundamental Research Division

Shunji IIO	Professor
Satoshi CHIBA	Professor
Hiroshi AKATSUKA	Associate Professor
Hiroaki TSUTSUI	Associate Professor

Advanced Research and Education Program

Akira NISHIMURA	Specially Appointed Professor
Isamu SATO	Specially Appointed Associate Professor
Saishun YAMAZAKI	Specially Appointed Assistant Professor

Common Staffs

Hirotake MORIYAMA	Specially Appointed Professor
Eiichi ASANO	Visiting Professor
Takatoshi TAKEMOTO	Visiting Associate Professor
Toshihiko KAWANO	Specially Appointed Professor
Fedir Alexeevich IVANIUK	Specially Appointed Professor
Matovic BRANKO	Specially Appointed Professor
Reda Ahmed Abdelhafeez El-KORAMY	Specially Appointed Professor
Maletaskic JELENA	Specially Appointed Assistant Professor

Technical Staffs

Ken-ichi TOSAKA	Senior Technical Specialist
Atsushi NEZU	Senior Technical Specialist
Keizo MATSUMURA	Senior Technical Specialist
Masamitsu IMAI	Senior Technical Specialist
Hitoshi FUKUDA	Senior Technical Specialist
Mitsuo MATSUZAKI	Senior Technical Specialist

I. Special Articles in Commemoration of Retiring Professors

I.1 Study on Neutron Capture Reaction

Masayuki Igashira

Study on neutron capture reaction by a group of the Tokyo Institute of Technology has been performed for about forty years and is reviewed briefly. In particular, E1 and/or M1 gamma-ray strength functions derived from measured keV-neutron capture gamma-ray spectra of medium and heavy nuclei, non-resonant p-wave neutron capture by light nuclei, and measurements of neutron capture cross sections of minor actinides and long-lived fission products are reviewed.

1. Introduction

Neutron capture reaction plays important roles in nuclear energy systems, nucleosynthesis in the universe, etc. Therefore, its related physical quantities, *e.g.* cross sections, capture gamma-ray spectra, are indispensable for the research and development of innovative nuclear energy systems, study on the nucleosynthesis in the universe, etc. From this view point, we have measured those physical quantities using the 3UH-HC (3 Units, Horizontal and High Current) Pelletron accelerator of the Tokyo Institute of Technology and the ANNRI (Accurate Neutron-Nucleus Reaction Measurement Instrument) of the MLF (Materials and Life Science Experimental Facility) of the J-PARC (Japan Proton Accelerator Research Complex).

In the present paper, E1 (Electric Dipole) and/or M1 (Magnetic Dipole) gamma-ray strength functions derived from measured keV-neutron capture gamma-ray spectra of medium and heavy nuclei, non-resonant p-wave neutron capture by light nuclei, and neutron capture cross sections of minor actinides and long-lived fission products are briefly reviewed.

2. Study using 3UH-HC Pelletron

2.1. 3UH-HC Pelletron accelerator and gamma-ray spectrometers

The 3UH-HC Pelletron accelerator with the maximum high voltage of 3 MV was installed at the Tokyo Institute of Technology in 1976 JFY (Japanese Fiscal Year), but it required more three years to succeed in accelerating ns (nano second) pulsed proton beams, which were used for keV-neutron generation by the ^{7}Li(p,n)^{7}Be reaction. At present, the width and peak current of the pulsed proton beam are typically 1.5 ns (FWHM) and 2 mA, respectively. As for the pulse repetition rate, 4 or 2 MHz is usually used.

An anti-Compton NaI(Tl) gamma-ray spectrometer with a heavy shield was developed for fast-neutron experiment [1], and has been improved several times. The size of the present main NaI(Tl) detector is 15.2 cm in diameter and 30.5 cm in length. The outer diameter and length of the present Compton suppression NaI(Tl) detector are 33.0 cm and 35.6 cm, respectively. The present NaI(Tl) gamma-ray spectrometer has better sensitivity than the original one by about ten times.

Moreover, an anti-Compton high purity Ge spectrometer with a heavy shield and a pair of large NaI(Tl) detectors were also developed. The anti-Compton Ge spectrometer has been used mainly for detecting gamma rays from neutron resonance capture. The pair of NaI(Tl) detectors is now installed in ANNRI to measure neutron capture cross sections of minor actinides and long-lived fission products.

2.2. E1 and/or M1 gamma-ray strength functions of medium and heavy nuclei

The capture gamma-ray spectra of Ag, In, Sb, I, Cs, Pr, Tb, Ho, Lu, Ta, and Au were measured at the neutron energies of 10 to 800 keV, using a TOF (Time Of Flight) method with the ^{7}Li(p,n)^{7}Be reaction pulsed neutron source and the original anti-Compton NaI(Tl) gamma-ray spectrometer [2,3]. A part of the spectra are shown in **Fig. 1**, where an anomalous bump, so-called the pygmy resonance, is clearly observed in all spectra. Combining the present data with the previous ones for Gd, ^{169}Tm, Re, Hg, Tl, and ^{206}Pb [4-7], remarkable features of the pygmy resonance were found to be that the resonance energy and the E1 strength exhausted in the resonance increase with neutron number but these quantities decrease precipitously around the neutron magic number N = 82, as shown in **Fig. 2**. Dots in the figure show the pygmy resonance energies (E_p) and vertical bars show the resonance widths (Γ_p).

Mohan *et al*. [8] proposed a three-fluid model for the E1 pygmy resonance. In their model, all the protons in a nucleus form one proton fluid, and neutrons form two fluids: one is called the blocked neutron fluid, which is formed by the neutrons that fulfil the same orbits as the protons, the other is called the excess neutron fluid, which is formed by the neutrons that are above the highest proton orbit. The E1 pygmy resonance was explained as the oscillation of the excess neutron fluid against the proton and blocked neutron fluids in their model.

Since the neutron magic number effect was observed in the systematics of the pygmy resonance, as shown in Fig. 2, we revised the three-fluid model of Mohan *et al.*: the excess neutron fluid was formed by the neutrons above the highest major shell in the nucleus. Calculated pygmy resonance energies by the revised model are shown by lines in Fig. 2. Solid lines show the calculated results with the same coupling constants among the three fluids as Mohan *et al*. By changing the coupling constants between the excess neutron and proton fluids and between the excess neutron and blocked neutron fluids, the calculation was also performed. The calculated results are shown by dashed lines and dash-dotted lines. The solid lines well reproduce the observed pygmy resonance energies. Concerning the ratios of the E1 pygmy resonance strength to the E1 sum rule [9], the calculation overestimated by about one order.

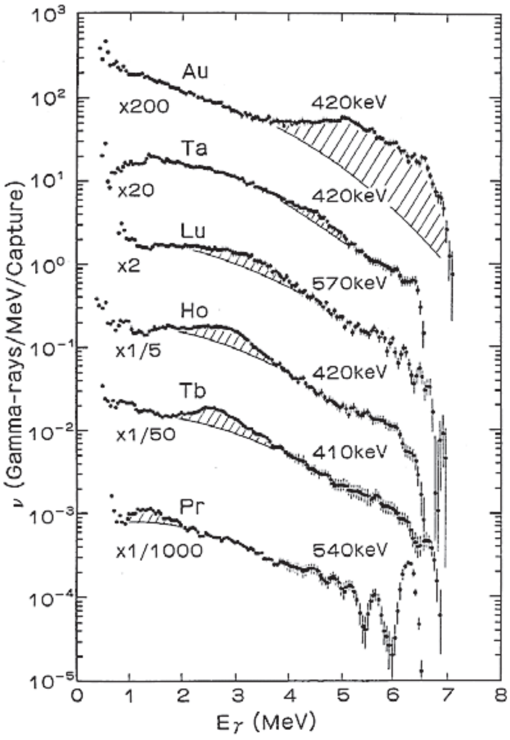

Fig. 1 Typical keV-neutron capture gamma-ray spectra

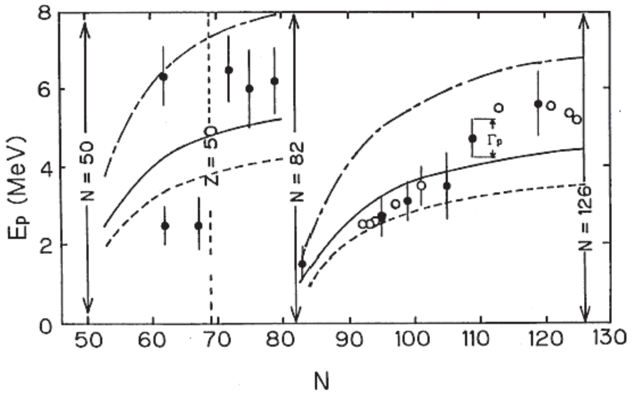

Fig. 2 Systematics of pygmy E1 resonance energy

The anomalous bump around 3 MeV as well as that around 5.5 MeV was attributed to the E1 pygmy resonance in the above discussion. However, an M1 scissors mode excitation was theoretically predicted around 3 MeV [10], and the M1 excitations from the ground state to excited states around 3 MeV were observed for deformed nuclei through (e,e'), (γ,γ'), and (n,n'γ) reactions [11]. Then, we measured the keV-neutron capture gamma-ray spectra of deformed nuclei such as ^{145}Nd [12], ^{161}Dy [13], and ^{167}Er [14], and analyzed the anomalous bump around 3 MeV as the M1 scissors mode [15]. For example, the statistical model calculation of capture gamma-ray spectrum for ^{161}Dy is compared with the experimental spectrum in **Fig. 3**. In the calculation, a small resonance was introduced in the M1 gamma-ray strength function so as to reproduce the experimental spectrum. From the fitted parameters of the M1 small resonance, *i.e.* energy (E_s), width (Γ_s), and peak cross section (σ_s), the reduced M1 transition strength, B(M1), was derived for each residual nucleus, as shown in **Fig. 4**, where the horizontal axis shows the square of the ground state quadrupole deformation parameter, β_2 [16], of the residual nucleus. Solid dots show the present (n,γ) results and open dots show the results through (γ,γ') experiment [17]. Both results well agree with each other, which means the anomalous bump around 3 MeV in the gamma-ray spectra of ^{145}Nd, ^{161}Dy, and ^{167}Er should be attributed to the M1 scissors mode excitation.

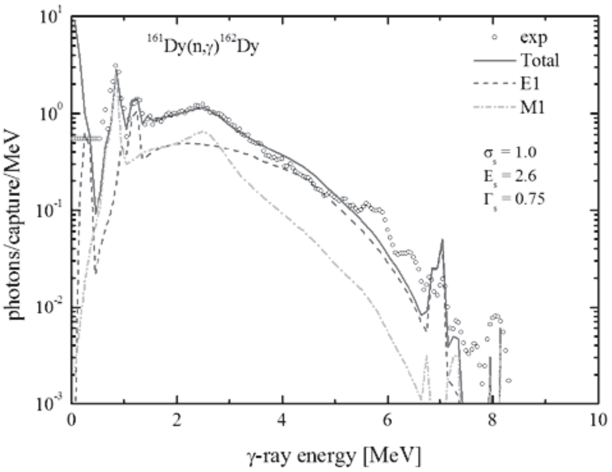

Fig. 3 40-keV neutron capture gamma-ray spectra of ^{161}Dy

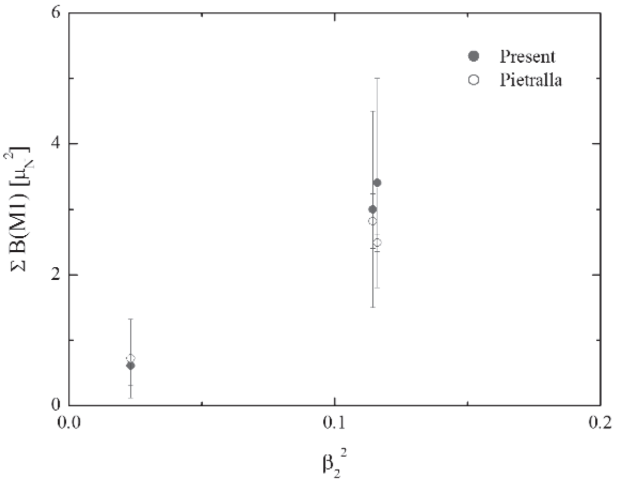

Fig. 4 ΣB(M1) versus β_2^2

2.3. Non-resonant p-wave neutron capture by light nuclei

The neutron capture cross sections around 30 keV of ^{12}C and ^{16}O are very important for the study on the s-process (slow neutron-capture process) of the nucleosynthesis in stars, because those nuclei are very abundant in s-process sites. However, the situation of measurements for those cross sections was very poor, because those cross sections were very small and the measurement was very difficult. For example, the capture cross section of ^{12}C was measured around 30 keV as 200 +- 400 μb [18], although the theoretical prediction with the thermal neutron capture cross section and the 1/*v* law (*v*: the velocity of incident neutron) was about 3 μb. A new measurement for ^{12}C [19] gave an upper limit of 14 μb around 30 keV. Then, we tried to measure those cross sections by using the TOF method described above [20-23].

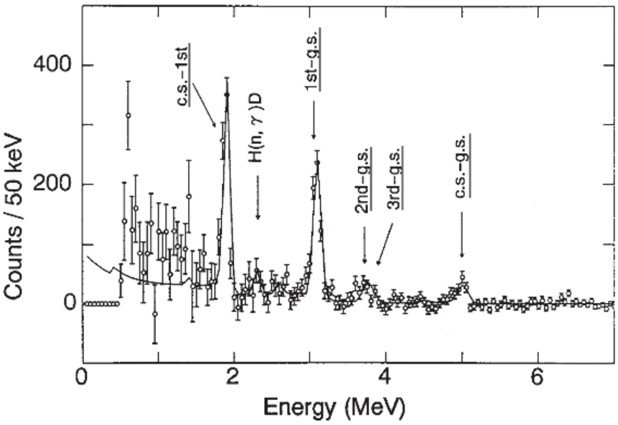

Fig. 5 ^{12}C(n,γ)^{13}C gamma-ray PH spectrum at 40 keV

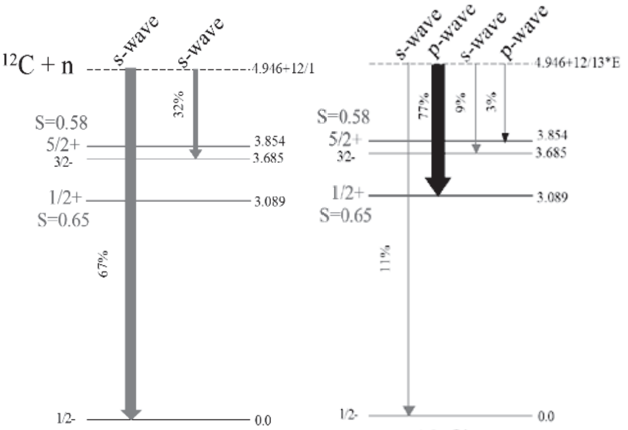

Fig. 6 Branching ratios of the capture state of ^{13}C for 40-keV (right) and thermal (left) neutrons

A capture gamma-ray PH (pulse-height) spectrum obtained from the measurement for ^{12}C is shown in **Fig. 5**, where the gamma rays due to the primary transitions from the capture state (c.s.) to the ground state (g.s.) and to the first excited state (1st) are clearly observed together with cascade transition gamma rays. From the analysis of the PH spectrum, the primary transitions from the 40-keV neutron capture state were derived, as shown in **Fig. 6**, where those from the thermal neutron capture state [24] are also shown. From the figure, it is found that the transition from the 40-keV neutron capture state to the first excited state ($1/2^+$) with a large neutron spectroscopic factor is dominant, whereas the ground state ($1/2^-$) transition is dominant in the case of the thermal neutron capture. It implies that the non-resonant p-wave neutron capture is important for the 40-keV neutron capture. **Figure 7** shows the neutron energy dependence of the partial capture cross sections to the ground and first excited states of ^{13}C. The partial capture cross section to the first excited state shows the *v* dependence, whereas that to the ground state shows the 1/*v* dependence. This *v* dependence of the dominant partial capture cross section to the first excited state indicates that non-resonant p-wave neutron capture is essential in the keV-neutron capture of ^{12}C. Summing up the measured partial capture cross sections, finally, the total capture cross section of ^{12}C was derived as15.4 +- 1.0 μb [21] for *kT* = 30 keV.

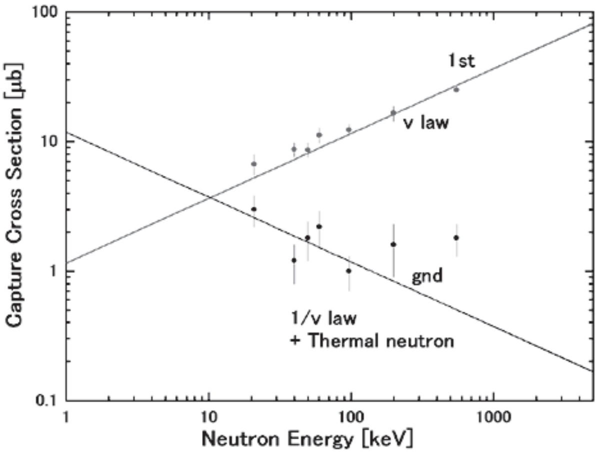

Fig. 7 Neutron energy dependences of the partial capture cross sections to the ground and first excited states of ^{13}C

As for the capture cross section of ^{16}O, using the same experimental technique as ^{12}C, it was derived as 34 +- 4 μb [23] for *kT* = 30 keV. The present value is larger than the previous measurement [25] by 170 times. The primary transitions from the 40-keV neutron capture state to the ground state ($5/2^+$) and to the first excited state ($1/2^+$) were 24% and 76%, respectively. Here, these states have a large neutron spectroscopy factor. These strong transitions mean that non-resonant p-wave neutron capture is also essential in the keV-neutron capture of ^{16}O. In the case of the thermal neutron capture of ^{16}O, the primary transition to the second excited state ($1/2^-$) is dominant, *i.e.* about 80%, and the total capture cross section is 0.190 +- 0.019 mb [26]. Evaluated values contained in nuclear data libraries such as JENDL and ENDF/B are compared with the present and previous experimental values in **Fig. 8**, where the evaluated values are identical except for those of

ENDF/B-VII.0, which adopted the previous experimental value. Recent evaluations have adopted the present measurement, as shown in Fig. 8.

It is worthy of note that, in the case of the keV-neutron capture of ^{7}Li, the s-wave, not p-wave, neutron capture is essential [27]. Since the residual nucleus, ^{8}Li, has only two bound states: the ground state (2^+) and the first excited state (1^+), and the spin and parity of the p-wave neutron capture state is 0^+, 1^+, 2^+, or 3^+, the E1 transition from the p-wave neutron capture state to the ground nor first excited state is forbidden. This is reason why the s-wave neutron capture is essential in the keV-neutron capture of ^{7}Li.

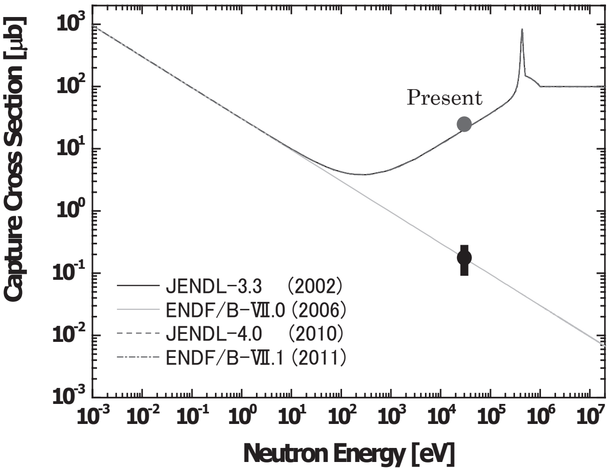

Fig. 8 Comparison of capture cross sections of ^{16}O. The red circle shows the present measurement and the black circle shows the previous measurement.

3. Study using ANNRI

3.1. ANNRI and gamma-ray spectrometers

ANNRI was installed at the BL04 (Beam Line #04) of MLF [28,29]. Two gamma-ray spectrometers were installed in ANNRI: one is a 4π Ge spectrometer at 22 m from the spallation neutron source of MLF and the other is the pair of large NaI(Tl) detectors described above at 27 m. The 4π Ge spectrometer is composed of two cluster Ge detectors and eight coaxial Ge detectors, *i.e.* totally 22 Ge crystals. The NaI(Tl) spectrometer is composed of two NaI(Tl) detectors: one with a diameter of 33.0 cm and a thickness of 20.3 cm at 90 degree with respect to the neutron beam direction, the other with a diameter of 20.3 cm and a thickness of 20.3 cm at 125 degree. Those spectrometers are surrounded by neutron and gamma-ray shields.

The aim of the maximum proton beam power at MLF is 1 MW, which is much higher than those of other facilities, *e.g.* LANSCE (Los Alamos Neutron Science Center: 80 kW) and n_TOF/CERN (9 kW), but the time resolution of proton beam, 100 ns, at MLF is worse compared to those of other facilities. Therefore, the design concept for ANNRI was to make the best use of the high proton beam power. The neutron intensity at the sample position for the 4π Ge spectrometer is compared with those at other facilities in **Fig. 9**, where the intensity corresponding to 200 kW proton beam power is shown for ANNRI. The neutron intensity at ANNRI is higher than those at the other facilities by one or two orders above 0.5 eV, as shown in Fig. 9.

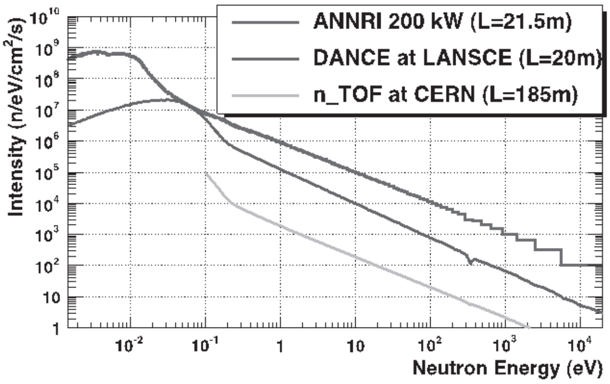

Fig. 9 Comparison of neutron intensities

3.2. Neutron capture cross sections of minor actinides and long-lived fission products

The neutron capture cross sections of minor actinides and long-lived fission products are very important for the research and development of nuclear transmutation technology for long-lived radioactive wastes which are generated in fission reactors. Therefore, the first mission of ANNRI is to measure those cross sections accurately.

The neutron capture cross sections of ^{237}Np, ^{241}Am, ^{243}Am, ^{244}Cm, and ^{246}Cm (minor actinides) and those of ^{93}Zr, ^{99}Tc, ^{107}Pd, and ^{129}I (long-lived fission products) have been measured, using the 4π Ge spectrometer and the NaI(Tl) spectrometer. Moreover, stable isotopes contained in the capture samples of long-lived fission products have been measured to correct for impurity effects on the capture yields of long-lived fission products. The neutron energy region for the measurements using the 4π Ge spectrometer was typically from thermal to several 100 eV, and that for the measurements using the NaI(Tl) spectrometer was typically from thermal to several 100 keV.

For example, the capture cross sections of ^{244}Cm obtained from the measurement using ANNRI [30] are shown in **Fig. 10**, where those from the previous measurement [31] and the evaluations of JENDL-4.0 are also shown. The previous measurement used a nuclear device as the neutron source. The present results below 20 eV are the first measurements in the world. It is worthy of note that the amount of the ^{244}Cm sample was very small, *i.e.* 0.6 mg, but its radioactivity was large, *i.e.* 2.0 GBq.

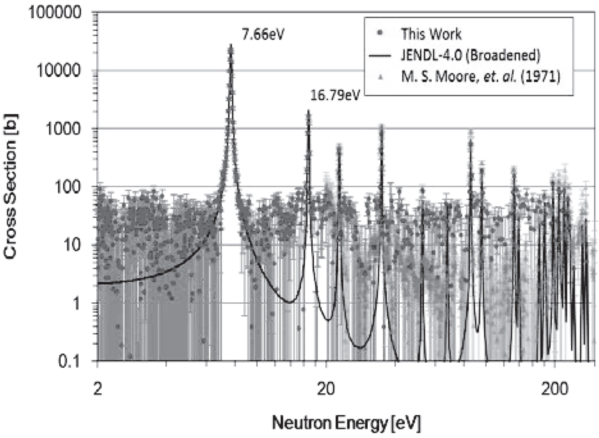

Fig. 10 Neutron capture cross sections of ^{244}Cm

4. Summary

Study on neutron capture reaction using the 3UH-HC Pelletron of the Tokyo Institute of Technology was reviewed briefly. In particular, E1 and/or M1 gamma-ray strength functions derived from measured keV-neutron capture gamma-ray spectra of medium and heavy nuclei and non-resonant p-wave neutron capture by light nuclei were reviewed. Concerning the gamma-ray strength functions, it was pointed out that the M1 scissors mode excitation was important for the deformed nuclei in the medium and heavy mass regions. On the other hand, the E1 pygmy resonance was semi-quantitatively explained as the oscillation of the excess neutron fluid against the proton and blocked neutron fluids in a modified three-fluid model. As for the capture reaction by light nuclei, it was pointed out that the non-resonant p-wave neutron capture was essential for light nuclei except for ^{7}Li.

Measurements of neutron capture cross sections of minor actinides and long-lived fission products using ANNRI/MLF/J-PARC was also reviewed briefly. The measurements were performed in the energy region from thermal to several 100 keV. As an example, the capture cross sections of ^{244}Cm measured using the 4π Ge spectrometer of ANNRI were shown. The results below 20 eV were the first measurements in the world. ANNRI will play an important role in the nuclear data field in the world.

References

[1] M. Igashira *et al*., *Nucl. Instr. Meth*., **A245** (1986) 432.
[2] M. Igashira *et al*., *Nucl. Phys*., **A457** (1986) 301.
[3] M. Igashira, Doctoral thesis, Tokyo Institute of Technology, 1987 [in Japanese].
[4] J. Voignier *et al*., *Nucl. Sci. Eng*., **93** (1986) 43.
[5] I. Bergqvist and N. Starfelt, *Nucl. Phys*., **39** (1962) 353; 529.
[6] G. A. Bartholomew *et al*., *Can. J. Phys*., **46** (1970) 687.
[7] S. Joly *et al*., *Phys. Rev*., **C20** (1979) 2027.
[8] R. Mohan *et al*., *Phys. Rev*. **C3** (1971) 1740.
[9] J. S. Levinger and H. A. Bethe, *Phys. Rev*., **78** (1950) 115.
[10] N. Lo Iudice and F. Palumbo, *Phys. Rev. Lett*., **41** (1978) 1532.
[11] for example, U. Kneissl, *Prog. Part. Nucl. Phys*., **28** (1992) 331.
[12] T. Veerapaspong *et al*., *J. Nucl. Sci. Technol*., **36** (1999) 855.
[13] S. Mizuno *et al*., *J. Nucl. Sci. Technol*., **36** (1999) 493.
[14] A. K. M. Harun-ar-rashid *et al*., *J. Nucl. Sci. Technol*., **37** (1999) 421.
[15] M. Igashira et al., *Proc. the 11-th Int. Symp. on Capture Gamma-Ray Spectroscopy and Related Topics, 2002*, ed. J. Kvasil et al. (World Scientific, 2003) 258.
[16] S. Raman *et al*., *At. Data Nucl. Tables*, **36** (1987) 1.
[17] N. Pietralla *et al*., *Phys. Rev*., **C52** (1995) 2317.
[18] R. L. Macklin and J. H. Gibbons, *Phys. Rev*., **159** (1967) 1007.
[19] R. L. Macklin, *ApJ*., **357** (1990) 649.
[20] Y. Nagai *et al*., *ApJ*,, **372** (1991) 683.
[21] T. Ohsaki *et al*., *ApJ*., **422** (1994) 912.
[22] T. Kikuchi *et al*., *Phys. Rev*., **C57** (1998) 2724.
[23] M. Igashira *et al*., *ApJ*., **441** (1995) L89.
[24] M. A. Lone, *Proc. the 4th Int. Symp. on Capture Gamma-Ray Spectroscopy and Related Topics, 1981,* ed. T. von Egidy et al. (Inst. Phys. Conf. Ser. No. 62) 383.
[25] B. J. Allen and R. L. Macklin, *Phys. Rev*., **C3** (1971) 1737.
[26] S. F. Mughabghab, *Atlas of Neutron Resonances, Resonance Parameters and Thermal Cross Sections Z = 1-100* (Elsevier 2006).
[27] Y. Nagai *et al*., *ApJ*., **381** (1991) 444.
[28] M. Igashira *et al*., *Nucl. Instr. Meth*., **A600** (2009) 332.
[29] Y. Kiyanagi, *J. Korean Physical Society*, **59** (2011) 779.
[30] A. Kimura et al., *J. Nucl. Sci. Technol*., **49** (2012) 708.
[31] M. S. Moore and G. A. Keyworth, *Phys. Rev*., **C3** (1971) 1656.

II. Research Reports

A. Innovative Nuclear Energy System Division

A.1 Progress in the study of Innovative Nuclear Energy Systems and Criticality Safety

Toru Obara

Studies on innovative nuclear reactor concepts and criticality safety have been performed. There was significant progress in the study of innovative prismatic and pebble bed type high temperature gas-cooled reactor concepts, CANDLE burning reactor concept, and critical safety analysis method for nuclear fuel solutions.

1. Study on small passive safe high temperature gas-cooled reactor

The design parameter conditions for high temperature gas-cooled reactors (HTGRs) with passive safety features of decay-heat removal have been obtained by residual-heat transfer calculation using equations for fundamental heat transfer mechanisms. HTGR operating at 1123 K temperature for passive decay-heat removal whose core dimension was determined using the relationships among several parameters including reactor size, power or power density and initial temperature of reactor regions in view of passive decay-heat removal. Performing the criticality and burnup analyses by using the proper composition of B_4Cparticles with a diameter of 0.02 cm with the volume ratio of 140 and Gd_2O_3 particles with a diameter of 0.02 cm with the volume ratio of 490 which are uniformly distributed in the proposed reactor core with coated fuel particles having 20wt% enrichment of uranium, the maximum excess reactivity can be suppressed from 32.7% _*k*/*k* to 3.06%_*k*/*k*. The systematic method to decide the core design which satisfies the condition for passive decay-heat removal was proposed, and a long-life small HTGR whose design parameters were determined using the condition. It was presented that the excess reactivity of the proposed reactor core was small during whole operation by performing proper optimization in the core configuration. The small excess reactivity is a significant advantage from the view point of safety in reactivity accident [1].

2. Study on small pebble bed reactor with ROX fuel

The pebble bed reactor (PBR), a kind of HTGR, is one of the most promising reactors in the generation IV initiative. This type of reactor is claimed to be have excellent passive safety features because of its graphite-moderated, helium-cooled and tristructural-isotropic (TRISO) fuel particles. Rock-like oxide (ROX) fuel has been studied at the Japan Atomic Energy Agency (JAEA) as a new once-through type fuel concept. With both mineral and ceramic properties, it is desired to improve the performance of the fuel elements not only in normal operation, but also for geological disposal without further reprocessing. The purpose of this study was to introduce the design concept for a small PBR with ROX fuel and to optimize the ROX fuel composition so that the reactor can achieve as high a burnup as possible without any failure of the spent fuel in the OTTO cycle. The power peak was set to less than the limit of the reference PBMR design to ensure that the reactor can be cooled by natural circulation and still survive in accident scenarios. In addition, an analysis of temperature coefficients was carried out to show the negative reactivity coefficient of the PBR with the UO_2-YSZ fuel. Results of the showed that we could design a 120-MW_{th} OTTO cycle small pebble bed reactor that could achieve a high discharge burnup of 145 GWd/t-HM and a FIFA value of 75%. In this case, the velocity of fuel pebbles is approximately 1.1 cm/day together with 2-g heavy metal loading per pebble and 20% uranium enrichment. The total power in a pebble and the maximum power density must be less than 4.5 kW and 10 W/cm^3, respectively, to keep the fuel temperature below 1600°C, the limit of the reference PBMR design during normal operation and during a DLOFC transient. Furthermore, the core height can be reduced without any effect on the burnup profile. Reducing the core height will improve economic efficiency, not only in construction but also in normal operation [2].

3. Study on small pebble bed reactor with accumulative fuel loading scheme

Teuchert proposed a new concept of fuel management in PBR design. At the start-up, the reactor cavity is filled with some amount of fuel balls, and under operation new fuel balls are filled in little by little until the cavity is fully filled. Due to the very slow movement of the fuel, this concept has been called the “Peu à Peu” method. For ease of understanding, in this study the method is called an accumulative fuel loading scheme. In the previous study, a small PBR with 110 MWt was designed using this method. However, the optimization of the loaded fuel composition was in sufficient. The purpose of this study was to obtain higher burnup performance by achieving optimum fuel composition based on finite geometry analysis. Burnup calculations were performed for a small PBR with an accumulative fuel loading scheme. Optimum fuel composition was achieved using 4-g HM uranium per pebble with 20% uranium enrichment. With these conditions, the results showed that the reactor could be operated for 5.6 years with a maximum burnup of 182 GWd/t. However, large excess reactivity occurred in the initial condition. To reduce this excess reactivity, enrichment was decreased from 20% to 4.2% only for the initial condition. The results showed that the excess reactivity could be reduced, but that the operation period and burnup value of this reactor would also decrease [3].

4. Study on supercritical kinetic analysis of fuel solution in several-tank system

In nuclear fuel fabrication facilities and reprocessing facilities, various types of nuclear fuels are processed, including powders, solids and solutions. However, most actual criticality accidents have occurred with the use of fuel solutions. Criticality accidents in fuel solutions have unique behaviors in terms of the feedback mechanism. It is important to analyze the kinetic behavior of fuel solutions in such circumstances to evaluate radiation doses and establish safety measures for criticality accidents. The purpose of this study was to perform analyses of the supercritical condition using the developed code for a several-tank system for different compositions of fuel solution and to estimate the increase of total energy released in a two-tank system compared with that of a single-tank system. Transient analyses for different compositions of fuel solution were performed for single- and two-tank systems. From these analyses, it was confirmed that as the enrichment of the fuel solution increases, the neutronic coupling in the two-tank system becomes stronger. The estimated increase of the total released energy was almost the same regardless of which feedback model was used in the analysis. Based on analysis, the total energy released in a system with several fuel-solution tanks may be estimated based on the total energy released in single-tank system at the same composition of fuel solution [4].

5. Study on the concept of CANDLE burning reactor with melt and refining process

The CANDLE (Constant Axial shape of Neutron flux, nuclide density and power shape During Life of Energy production) reactor concept has a unique way of utilizing the neutron flux such that it moves constantly with a speed proportional to the reactor power, along the direction of the core axis without changing the spatial distribution of nuclides densities, neutron flux, and power density. The idea of applying the melt and refining procedure to the CANDLE reactor concept before it reaches the cladding limitation at 200dpa seems like a possible solution to the cladding problem in high burnup. However, if the melt and refining procedure is applied during CANDLE operation, the nuclide distribution in the fuel pins might be lost. The purpose of this study was to determine the effects of melt and refining on a CANDLE reactor with comparison in several homogenization regions. Metal fuel is most likely to achieve > 200dpa during long-term of operation. The results of analyses showed that the application of a melt and refining process to a CANDLE core by introducing nuclide composition homogenization at each fuel movement cycle was found to be a feasible solution to overcome the limitation of metal fuel cladding in a CANDLE burning reactor [5].

References

1. S. Odmaa, T. Obara; *Journal of Nuclear Science and Technology*, Vol. 52, pp.1519-1529 (2015).
2. H. Q. Ho, T. Obara: *Annals of Nuclear Energy*, Vol. 83, pp. 1-7 (2015).
3. I. L. Simanullang, T. Obara: *Transactions of the American Nuclear Society*, Vol. 113, pp. 919-921 (2015).
4. H. Kikuchi, T. Obara; *Progress in Nuclear Energy,* Vol. 82, pp. 96-101 (2015).
5. J. A. Karim, J. Nishiyama, T. Obara: *Transactions of the American Nuclear Society*, Vol. 113, pp. 924-926 (2015).

A.2 SOLID OXIDE ELECTROLYSIS CELL FOR CARBON RECYCLING ENERGY SYSTEM DRIVEN BY NUCLEAR POWERS

Yukitaka Kato

1. INTRODUCTION

The increase of carbon dioxide (CO_2) emissions due to the consumption of fossil fuels causes global environmental problems. In Japan, almost all primary energies are imported from other countries. Reductions of CO_2 emissions and primary energy imports have been difficult problems to be addressed. However, a new low-carbon energy system has been proposed, which is referred to as an active carbon recycling energy system (ACRES)[1]. With ACRES, carbon energy materials such as carbon monoxide (CO) are regenerated from CO_2 and reused cyclically. CO has a higher exergy ratio (ΔG / ΔH) than hydrogen (H_2) and methane, which makes CO an important candidate as a recycling media for ACRES. In ACRES, CO_2 separated from exhaust gas is reduced to CO, as shown in Eq. (1), and the regenerated CO is used cyclically as an energy medium.

$$CO_2 \rightarrow CO + 1/2\ O_2 \qquad (1)$$

CO_2 reduction into CO is a key technology for the establishment of ACRES. It is possible to reduce CO_2 into CO by an electrolysis process, such as with a solid oxide electrolysis cell (SOEC), which employs the opposite operation of a solid oxide fuel cell (SOFC)[2].

ACRES is expected to be applicable with iron-making processes, because CO can be used directly for the reduction of iron ore. After CO_2 generated from a blast furnace is captured, CO is regenerated from CO_2 using the SOEC. The regenerated CO is recirculated in a blast furnace, so that the quantity of coke (reducing agent) required can be reduced. A proposed application of ACRES for an iron-making process referred to as a smart iron-making system based on ACRES (iACRES) is shown in Fig. 1 [3]. As primary energy sources for a high-temperature gas cooled reactor (HTGR) used for ACRES, renewable energies such as solar and wind, and waste heat from high-temperature industrial processes are proposed as candidates. The HTGR, in particular, is a chief candidate for iACRES because it is capable of sufficiently high-temperature heat production up to 950 °C and stable heat output for iACRES.

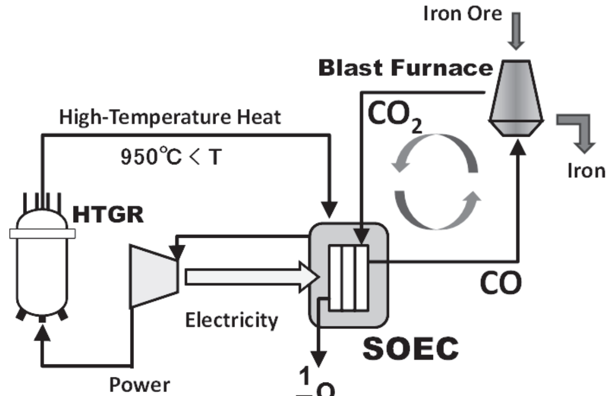

Fig. 1 Schematic of the iACRES concept.

Although previous studies demonstrated CO_2 electrolysis, however, knowledge about availability of SOEC CO_2 electrolysis under operation conditions of gas compositions and temperatures for iACRES was still small. Then, in this study, a disk-type SOEC was prepared and the SOEC electrolysis performance was measured experimentally at the laboratory scale. The availability of a practical iron-making system based on iACRES was evaluated using the experimental results for the SOEC.

2. PRINCIPLE OF SOEC

A SOEC electrolyzes carbon dioxide by the application of an overvoltage in the cell. SOEC has a three-layer structure of cathode|solid electrolyte|anode. CO_2 is supplied to a porous cathode and diffuses through the micropores of the electrode. CO_2 is then decomposed into CO and O^{-2} by electrons supplied to cathode, as shown in Eq. (2):

$$CO_2 + 2e^- \rightarrow CO + O^{2-} \qquad (2)$$

The oxygen ions generated are transported to the anode through ionic defects in the solid oxide electrolyte and oxygen is generated:

$$O^{2-} \rightarrow 1/2O_2 + 2e^- \qquad (3)$$

The overall reaction from Eqs. (2) and (3) gives Eq. (1). The energy change for Eq. (1) is given by

$$\Delta H = \Delta G + T\Delta S \qquad (4)$$

where ΔH [J mol^{-1}], ΔG [J mol^{-1}], and ΔS [J mol^{-1} K^{-1}] are the Gibbs free energy, enthalpy, and entropy changes for the reaction, respectively, and T [K] is the reaction temperature. For establishment of the reaction by the supply of ΔH, the ΔG term is covered by the use of electricity, while the $T\Delta S$ term is provided by thermal energy. The decomposition voltage of CO_2 ($E°$ [V]) is dependent on ΔG, which is expressed as

$$E° = -\Delta G / (\ nF\ ) \qquad (5)$$

where n is the number of the valence electrons and F is Faraday's constant (= 96500 C/mol). The catalytic reactions at the electrodes, gas diffusion in the electrode layer, and ohmic resistance must be considered for performance improvement of SOEC. Yttria-stabilized zirconia (YSZ) is mainly used as solid oxide electrolytes[9], which become oxygen ion conductors at high temperatures around 700–1000 °C.

3. EXPERIMENTAL AND RESULTS

The experimental apparatus was constructed to measure the performance of the SOEC [4]. CO_2 gas is introduced to the reactor as a reaction gas, and Ar is used as a carrier gas at the cathode side. N_2 is used as a carrier gas for oxygen generated via electrolysis at the anode side. The reacted gases were analyzed using gas chromatography.

Fig. 2 shows a cross-sectional schematic of the SOEC reactor. The SOEC (20 mm diameter and 1.0 mm thick) was held by two outer alumina tubes (20 mm outer diameter) and sealed with glass rings. The electrolyte cell thickness was relatively thicker than conventional cell, then, it was thought that IR loss of the cell was relatively larger than conventional one. It was expected that electrolysis performance would be improved by the reduction of the thickness. Reaction gases were supplied through inner tubes (6 mm outer diameter). The electrical current was collected using platinum mesh (7×7 mm^2) attached to each end of the inner tubes. The glass ring seals were melted at 950 °C prior to operation of the SOEC. In this study, a cell with the structure $Ni\text{-}YSZ|YSZ|La_{0.6}Sr_{0.4}Co_{0.2}Fe_{0.8}O_{3-\delta}$ (LSCF) was selected. For the cathode, Ni and YSZ were employed as the catalyst and oxygen ion conductor, respectively.

A current density of 107.1 mA cm^{-2} was measured between the cathode and anode at 2.52 V and 900 °C. The CO and O_2 production rate were measured. The theoretical production rate is dependent on the current density according to Faraday's law.

Based on the experimental results, iACRES as a combination of ACRES with a blast furnace was evaluated when CO_2 in the blast furnace gas (BFG) was reduced to CO by the SOEC. Heat and electricity generated from the HTGR were used together for the high-temperature CO_2 electrolysis in the SOEC. The required HTGR unit numbers and SOEC surface area for a blast furnace were calculated.

A blast furnace used conventionally in large ironworks[10] with an annual pig-iron production of 2.5 Mt y^{-1} was employed as a model for the evaluation. An HTGR plant, in which the secondary coolant has 600 MW-thermal (MWt) at 850 °C[11], was employed for the electrolysis. From measured current density of 0.071 A cm^{-2} at 800°C, CO_2 decomposition rate of 0.37×10^{-6} mol s^{-1} cm^{-2} was calculated, and required surface area of SOEC cell was estimated as 0.098 km^2 for required CO_2 decomposition rate of 358.1 mol s^{-1}. 37.9 MWt and 171 MW of electricity (MWe) were required for the SOEC reduction of the CO_2. Then, total thermal output from HTGR of 493 MWt was needed. The thermal output was corresponding to output of 0.78 HTGR unit. If SOEC current density was improved to 1 A cm^2, required SOEC cell surface area was expected to be reduced to 6.9×10^3 m^2 (0.0069 km^2). It was understood that the improvement of SOEC performance was important way for reduction of volume of CO_2 reduction facility. These evaluated values would be useful information for system scale evaluation in feasibility studies of iACRES.

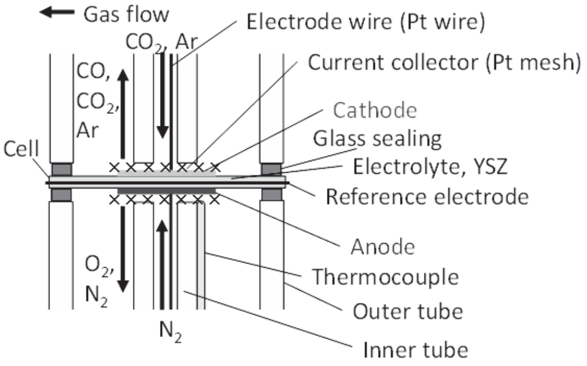

Fig. 2 Cross-section of the SOEC reactor.

4. CONCLUSION

SOEC experimental apparatus was fabricated for CO_2 reduction to CO. The SOEC experiment was conducted. The iACRES evaluation indicated that 0.73 HTGR units and an electrode surface area of 0.098 km^2 were required for the reduction of 30% of the CO_2 in conventional blast furnace gas. These results indicate the possibility of carbon recycling with iACRES driven by nuclear powers.

References

[1] Y. Kato, *ISIJ Int'l*, 50(1), pp. 181-185 (2010).
[2] A. L. Dipu, J. Ryu, Y. Kato, *ISIJ Int'l.*, 52(8), pp. 1427–1432 (2012).
[3] Y. Kato, *Prog. Nuc. Eng.*, 82, pp. 53-57 (2015).
[4] G. Fujii, J. Ryu, K. Yoshida, T. Yano, Y. Kato, *ISIJ Int'l*, 55(2), pp. 387-391 (2015).

A.3 Improvement of Critical Heat Flux Performance by Wire Spacer

Minoru Takahashi, Dan Tri Le

1. Introduction

Boiling water reactors (BWR) could have a higher conversion ratio nearly equal to unity by reducing moderator-fuel ratio with smaller coolant volume ratio compared with a normal core, that is, P/d is less that 1.1. The use of wire spacers is more suitable for the tight lattice core than the use of grid spacers. Heat removability is one of key issues for the feasibility of the tight lattice core with the wire spacer because of the small flow area. The most important feature of coolability of tight lattice core is the critical heat flux (CHF). In the present study, the effect of the wire spacer on the enhancement of CHF for the case of tight lattice arrangement was investigated by means of CHF experiment for single pin test section with a wire spacer. Three difference values of gap size were chosen: 1.1, 1.5, 2.0 mm to cover the range at which the conversion ration could be nearly equal to unity.

2. Experimental Apparatus and Procedure

2.1 Experimental Apparatus

The experimental apparatus of a water circulation loop consists of a water tank, a circulation pump, a pre-heater,an orifice flow meter and a CHF test section. The water flowed from the water tank through the circulation pump and the pre-heater and entered the test section. The system pressure was kept at the atmospheric pressure.

2.2 Test Section

Fig. 1 shows the vertical CHF test section. The main parts of the test section are the heater pin, the upper and bottom copper electrodes, the glass tube, the thermocouples and the wire spacer in case of experiment for a heater pin with a wire spacer. The heater pin was directly Joule-heated. The materials of the glass tube used were Pyrex glass and crystal glass. The heater pin was made of a thin stainless steel tube with an outer diameter, d, of 8 mm and a length of 420 mm. It was connected to the copper electrodes at both ends by silver soldering. The heated length of the heater pin tube with a thin wall, L, was 400 mm. The axial pitch of the wire spacer, H, was set with two different values of 100 mm and 200 mm.

The spacer was electrically insulated from the heater pin. Fig. 1(c) shows the wire spacer made of a Teflon tube in which a stainless steel wire was inserted. Gap size, δ, is the distance from the outer surface of heater pin to the inner surface of the glass tube. For the rod diameter of 8 mm, three different values of gap size were chosen: 1.1, 1.5 and 2.0 mm.

The direct Joule-heating of the heater pin provided an uniform heat flux on the heater pin surface. The maximum power and current of the power in this experiment were 15 kW and 500 A, respectively.

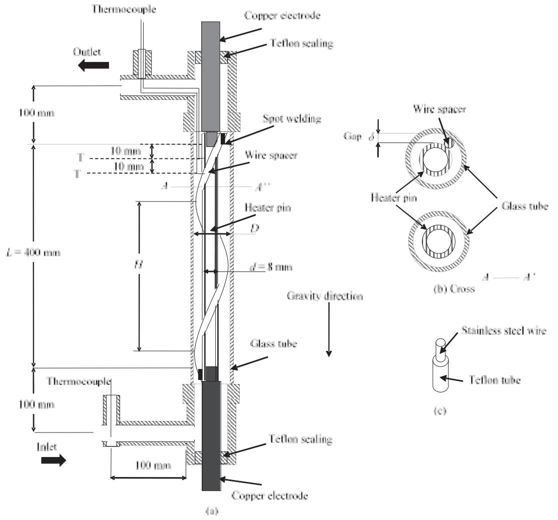

Fig. 1 Test section: (a) test section; (b) cross section of flow channel with wire and without wire spacer; (c) wire structure.

To detect a sudden temperature rise on the heater pin surface at the CHF condition and quickly shutdown the heating power, type K thermocouple elements with diameter of 100 μm were used for the surface heater pin temperature measurement. Fig. 1(a) shows that the ends of the thermocouple elements were spot-welded to the surface to be hot junction at positions of 20 mm and 10 mm upstream from the downstream end of the heated length, being marked as T1 and T2, respectively.

2.3 Experimental Conditions

Parameters in the experiment were the existence of the wire spacer, the gap size and the axial coil pitch of the wire, and the mass flux. In order to investigate the effect of a wire spacer on CHF, the CHF experiments for both case of heater pin with and without a wire spacer were performed under the same mass flux condition. On the other hand, to investigater the effect of gap size on CHF, the experiments at the same mass flow rate were chosen.

2.4 Experimental Procedure and Measurement Items

The water in the water circulation loop was degassed initially by boiling the water in the test section for a while until air dissolved in the water was removed sufficiently.

During the experiment, the water flow rate was kept constant. The flow resistance at the inlet valve of the test section was kept high enough to suppress the instability of flow rate due to the instability of pressure drop of two-phase flow in the test section. When the water temperature at the inlet of the test section reached the desired value by controlling the pre-heater, the electric power to the heater pin in the test section was increased gradually by remote controlling.

Surface temperature of the heater pin was measured and recorded by using the thermocouples. The power of the heater pin was increased step by step until the surface temperature of the heater pin rapidly and suddenly increased because of reaching the CHF condition. Immediately after reaching the CHF condition, the power source was automatically shut down by the signal of sudden rise of surface temperature.

Fig. 2 shows the behaviors of the measured surface and inlet temperatures, voltage and current during the operation. It can be seen that the inlet temperature was kept constant. The surface temperatures T1 and T2 increased slightly due to the increase of the electric power to the heater pin, and then suddenly the surface temperatures of the heater pin T1 and T2 rapidly increased. It was judged that at this time, the burn-out took place or the heat flux reached the CHF.

The measurements were made under the boiling two-phase flow condition. The measurement accuracy of the heat flux value was high enough since it was determined from measured voltage and current.

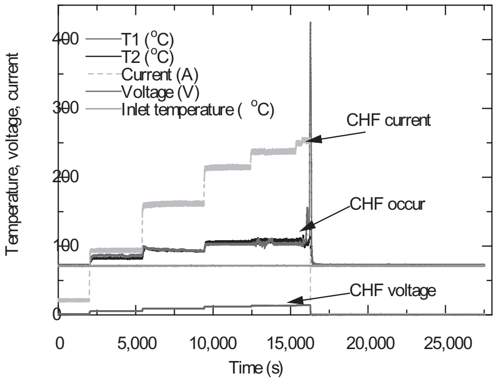

Fig. **2** Temperature behavior during the experiment.

3. Results and Discussion

3.1 Comparison with Look up Table Data

Fig. 3 shows the calculated values obtained by using the CHF correlation with the rod-centered approach and the 2006 CHF look up table data. It is found that the results were close to the experimental results of heater pin without a wire spacer.

3.2 Effect of Wire Spacer

Fig. 4 shows the comparison of the CHF values of single pin channels between with the wire spacer and without the wire spacer. It was found that the CHF values in both types of heater pin decreased with the decrease of the inlet equilibrium steam quality, x_{in}. However, the CHF values were higher in case of heater pin with the wire spacer than that in case of heater pin without the wire spacer. It could be explained by the enhancement of bubble removal from the heated surface due to the effect of wire and spiral flow. Compared with the work of Cheng and Müller, the results of the present study were obtained in smaller range of the quality from -0.1 to 0. However, it can be seen that the CHF values of wire type were still higher than those without wire type even if the inlet equilibrium steam quality was close to zero. Besides, the difference in the CHF values between heater pin with and without wire spacer was larger in lower qualities compared with the difference of CHF in higher qualities.

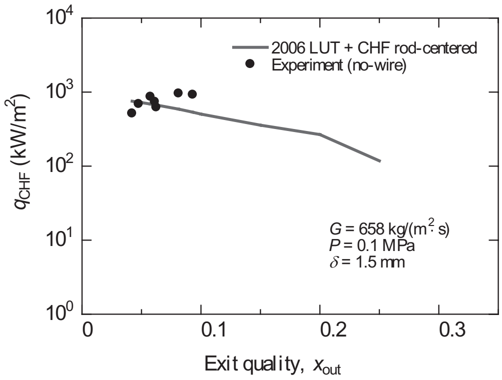

Fig. 3 Comparison of experimental results with the calculated results using CHF correlation for the rod-centered approach for the CHF look-up table.

In furtherance of the investigation of CHF behavior under the effect of the wire spacer, the change in wire spacer size is needed. Therefore, the CHF experiment with different value of δ and H was performed to deal with such kind of study. These experiments were performed under the same flow rate condition of the practical reactor rather than the same mass flux. From reactor design point of view, the consideration of the same water flow rate rather than the same mass flux is needed to be able to keep the best coolability for difference core design. Fig. 5 shows the comparison of the CHF values between three different values of gap size at the same flow rate. It can be seen that at the same local quality, x_z, the CHF values were enhanced with the decrease of gap size under the same flow rate condition. In more detail, the CHF values were higher in case of smaller gap size and it was the highest in case of the smallest gap size. That is because the channel which has the smallest flow area has the highest mass flux at the same water mass flow rate which leads to the enhancement of CHF values. Moreover, there is an effect of the water film along the inner surface of the channel (glass tube) on CHF values. At the low quality region and bigger channel, this effect does not have the big influence on CHF value. However, at the high quality region and smaller gap size, the cold wall effect became higher. In detail, the vapor

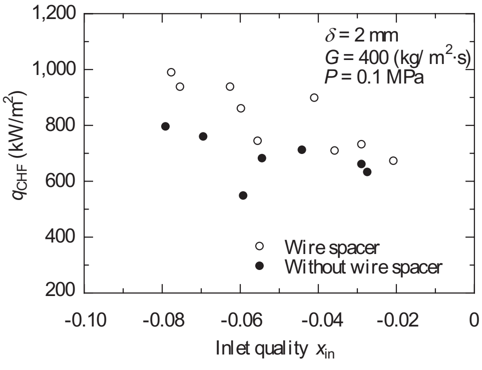

Fig. 4 Critical heat flux base on inlet condition.

velocity was high in case of high quality region due to the high evaporation rate. Therefore, it may disturb the water film which flow along the inner surface of the channel and bring the droplets to the heated surface because of increasing of droplet deposition rate. The phenomena lead to the increase of CHF values at high quality region. On the other hand, with the smaller gap size, the droplet concentration in the vapor phase was also higher compared with it in case of bigger gap size. This is another reason which contributed for the increase of CHF values.

On the other hand, according to Fig. 5, the experiment with smaller gap size could reach higher CHF values and also could go to the higher local quality, x_z. Moreover, in case of bigger gap size ($\delta = 2.0$ mm), the CHF value tended to decrease with the increase of quality. However, in case of flow channel with small gap size, the CHF values were nearly constant value or slightly increase with the increasing of quality.

Fig. 6 illustrates the CHF results in two different values of wire pitch, *H*. It can be seen that the CHF values were nearly the same between two different values of *H*. It can be explained that there were two flow channels with two different values of wire pitch, velocity was the same. Since the velocity was the same, the mass flux was the same. Therefore, it is clear that, the axial pitch did not have a large influence on the CHF. However, it is necessary to consider the pressure drop for the design purpose at the same time.

3.3 Axial Position of CHF

The relation between the CHF values and the heated length to the position of arriving at CHF is shown in Fig. 7. It is found that at the same mass flow rate, *W*, the CHF occurred mostly in the downstream of the flow channel. Fig. 7 also shows the comparison of CHF position among three different values of gap size. In case of gap size of 1.5 mm and 2.0 mm, the CHF positions were mainly at the downstream of flow channel. Therefore, the CHF in this case was principally caused by liquid film dry-out. On the other hand, with the smallest flow area, gap size of 1.1 mm, there was the possibility of CHF occurring at the upstream of flow channel because of the high heat flux and high flow rate. According to the results, the CHF positions changed slightly with different values of the flow area or gap size. The CHF position tended to move from downstream to the upstream of the flow channel due to the decrease of gap size.

4. Conclusions

The CHF phenomena for the tight lattice fuel arrangement with the effect of wire spacer were investigated by mean of the experiment for single fuel pin with and without wire spacer and three difference values of gap size of 1.1, 1.5, 2.0 mm. The conclusions are as follows:

(1) The CHF in case of heater pin with circular shape wire was enhanced up to 25% compared with it in case of without wire space under the same flow condition. Therefore, the coolability or heat removability was enhanced by the existence of the wire spacer and spiral flow;

(2) With the same flow rate condition, the CHF values can be increased up to 100% with the decrease of gap size. Therefore, the flow channel with smaller gap size had a higher coolability compared with the flow channel with larger gap size;

(3) The change in a pitch of wire, *H*, with two difference values of 100 mm and 200 mm did not have a large influence on the CHF if the mass flux was kept constant. The experiment data was nearly the same value even with two different cases of wire pitch.

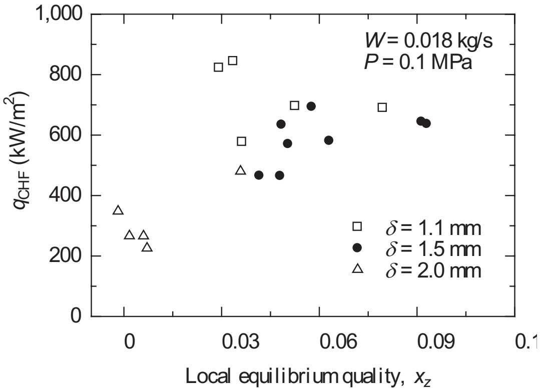

Fig. 5 Critical heat flux for three different gap sizes.

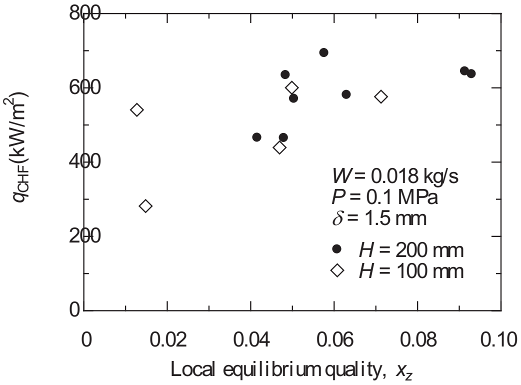

Fig. 6 Critical heat flux of two different wire pitches, *H*.

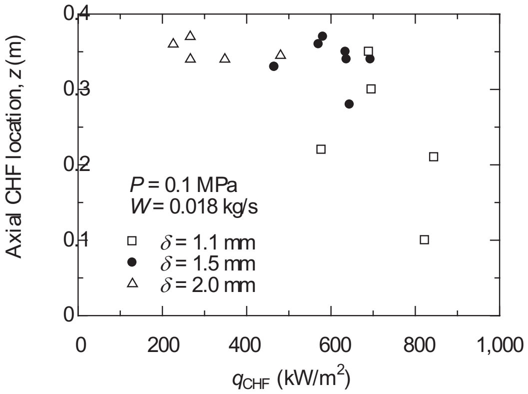

Fig. 7 Critical heat flux base on the heated length.

Reference

(1) Dan Tri Le, Minoru Takahashi: Improvement of Critical Heat Flux Performance by Wire Spacer; Journal of Energy and Power Engineering, Vol.9, No.10, pp.844-851, 2015, doi:10.17265/1934-8975/2015.010.002.

A.4 Progress of Neutron Capture Measurements at Tokyo Institute of Technology

Masayuki Igashira, Tatsuya Katabuchi, Tatsuhiro Saito,
Takeshi Nagasaka, Seigo Umezawa, Karin Takebe, Ryo Fujioka

1. Introduction

In 2015 fiscal year, our research group worked on three topics:

1. Neutron capture cross section and γ-ray spectra of ^{89}Y
2. Gamma-ray production yields from a p-Li neutron source for boron neutron capture therapy
3. Neutron capture cross section of ^{99}Tc

Experiments for the first two topics were performed in the Tokyo Tech. Measurements for the last topic were made in the Japan Proton Accelerator Research Complex (J-PARC) in the Japan Atomic Energy Agency.

2. Tokyo Tech

2.1. Yttrium-89

We measured the neutron capture cross section and the neutron capture γ-ray spectrum of ^{89}Y in the keV neutron energy region. This experiments were motivated by s-process nucleosynthesis. In the s-process reaction network, neutron magic nuclides are important because their neutron capture cross sections are small, thus forming bottlenecks of the s-process path. Yttrium-89 is one of the N=50 neutron magic nuclides. Accurate neutron capture cross section of ^{89}Y is required to calculate *s*-process production yields in stellar nucleosynthesis models. In 2014, we measured the capture cross section of ^{89}Y in the energy range from 15 to 100 keV. We continued this campaign this year, extending measurement at an incident neutron energy of 550 keV.

Experiments were performed using a neutron beam from the ^{7}Li(p,n)^{7}Be reaction induced by a proton beam from the Pelleton accelerator. The incident neutron energy was 550 keV. The neutron energy was determined by the time-of-flight (TOF) method. The incident neutron spectrum was measured with a ^{6}Li glass scintillator located at a distance of about 4.4 m from the neutron source. A natural Y_2O_3 sample was used in the experiments. The sample was placed at a neutron flight distance of 20 cm. Gamma-rays emitted from the neutron capture reaction were detected with an anti-Compton NaI(Tl) spectrometer. The pulse-height weighting technique was applied to derive neutron capture yields. Runs for a gold sample were also made as reference measurements to the standard cross section of the ^{197}Au(n,γ)^{198}Au reaction.

2.2. Gamma-ray production yields from p-Li neutron source for boron neutron capture therapy

This research was motivated by a medical application of neutron science, i.e. boron neutron capture therapy (BNCT). BNCT uses high LET particles from the ^{10}B(n,α)^{7}Li reaction to terminate cancer cells. Neutron sources for BNCT has been nuclear reactors since the beginning of the history but accelerator neutron sources are emerging for the next generation of BNCT. Accelerator-based BNCT can overcome limits the current BNCT has, for example, strict regulation associated with nuclear reactors or public acceptance to implement BNCT in city areas. To achieve the technological requirements, several types of BNCT accelerators have been suggested. In the suggested ideas, the ^{7}Li(p,n)^{7}Be reaction is one candidate neutron production reaction. The ^{7}Li(p,n)^{7}Be reaction requires low proton energy, thus leading to a compact accelerator system. However there is one concern to deploy ^{7}Li(p,n)^{7}Be neutron sources for the medical application. When a lithium target is bombarded with a proton beam, not only neutron production reaction ^{7}Li(p,n)^{7}Be but also γ-ray production reactions, ^{7}Li(p,p')^{7}Li* and ^{7}Li(p,γ)^{8}Be, occur. The γ-ray production rate is high and the γ-ray energy distributes up to around 18 MeV. This γ-rays from a p-Li neutron source introduce undesired radiation dose to a patient. To estimate absorbed dose by the γ-rays, γ-ray nuclear data such as γ-ray production yield and γ-ray spectrum, are necessary. In the present work, we measured the γ-ray spectrum from a p-Li neutron source and derived γ-ray production yields of the ^{7}Li(p,p')^{7}Li* and ^{7}Li(p,γ)^{8}Be reactions.

Experiments were performed in the Tokyo Institute of Technology. A Li target on a Cu backing was irradiated with a proton beam from a Pelletron accelerator. The thickness of the Li target was 0.3 mm, thick enough for the proton to stop in the Li layer. Gamma-rays from the neutron source were detected with a NaI(Tl) detector placed at 0° with respect to the beam axis. After background subtraction, the γ-ray spectrum was derived by unfolding the obtained pulse-height spectrum with detector response functions. The thick target γ-ray production yields were derived from peak areas of the ^{7}Li(p,p')^{7}Li* and ^{7}Li(p,γ)^{8}Be reactions. The results were reported in Ref. [1].

3. J-PARC

3.1. Technetium-99

We measured the neutron capture cross section of ^{99}Tc at J-PARC. Technetium-99 is a long-lived fission product (LLFP) produced in spent nuclear fuel. Long-term nuclear waste management is a debatable issue due to LLFP and long-lived minor actinides. One proposed solution is the nuclear transmutation, in which LLFP nuclides are transmuted into stable or short-lived isotopes via the neutron-induced nuclear reaction. Technetium-99 is high priority for transmutation because the cumulative fission yield and the radio toxicity are very high. To design a nuclear transmutation system, reliable nuclear data of ^{99}Tc are required. Thus, we conducted measurement of the nuclear capture cross section of ^{99}Tc.

A time-of-fligh spectrum of neutron capture events of ^{99}Tc was measured using the Accurate Neutron Nucleus Reaction Measurement Instrument (ANNRI) at J-PARC. The sample of ^{99}Tc was placed at a flight distance of 27.9 m from the spallation neutron source. Capture γ-rays from the sample were detected with an NaI(Tl) detector placed at a scattering angle of 90° with respect to the beam axis. The neutron capture cross section of ^{99}Tc was determined from the thermal to keV energy region. In paticular, effort has been made to measure the cross section in the high energy region.

Reference

1. T. Saito, T. Katabuchi *et al*., Journal of Nuclear Science and Technology. Vol. 54, pp. 253-259 (2017).

A.5 Chemical behaviors of lead-alloy coolants in air ingress accident

Masatoshi KONDO

1. Introduction

The conceptual designs of fast reactors cooled by liquid lead (Pb) or lead bismuth eutectic (LBE, Pb44.5-Bi55.5) have been studied, and some of these designs have been discussed under the collaboration of the Generation IV International Forum (GIF). Liquid LBE is also the target material of accelerator driven system (ADS). The compatibility of the lead based coolant with some candidate structural materials is one of the important issues. However, it was found that the occurrence of the severe dissolution type corrosion and the corrosion-erosion [1] was suppressed by the formation of the protective oxide layers [2] on the steel surfaces by the control of the oxygen potential of the liquid alloy [3]. The protectiveness of their layers was improved by the alloying elements of Al and Si in the steel [4]. The compatibility was also improved by the unti-corrosion coating technology [5]. Pb-17Li alloy is one of the candidate tritium breeders in the design of the fusion reactors. The technical issues, which are similar to the lead based fast reactors, have been studied [6, 7].

The chemical reactivity of Pb based alloys with water is negligibly small even at high temperature. This advantage enables to design the Pb-Bi-cooled direct contact boiling water type fast reactor. The chemical reaction between these liquid metals and air is not violent, though these are oxidized by air. The air cooled type emergency core cooling system (ECCS) is adopted in some designs of the lead alloy cooled FRs and ADSs. The ECCS by the natural convection of atmospheric air is equipped in the reactor system of BREST-OD-300. The air cooled type reactor vessel auxiliary cooling system (RVACS), which is for passive decay heat removal of the reactor, is equipped in the design of the European Lead Fast Reactor (ELSY) and the China lead-based research reactor (CLEAR-1). The ADSs of MYRRHA and XT-ADS also equips the RVACS in their design.

The air ingress accident is caused when these air cooling systems become the route of air ingression into the liquid metal coolant. When a large quantity of oxides is formed by the air ingress situations, the pipe plugging can be caused in the primary coolant system. In the same time, the degradation of the heat transfer efficiency due to the precipitation of oxides on the heat exchanger is also concerned. These situations cause the eventual temperature increase of the reactor core. Therefore, the air ingress situation causes a potential risk for some low probable situations of severe accidents in the reactors. However, the chemical behaviors of the coolant in the air ingress situation for the lead alloy cooled reactor are not made clear so far.

The purpose of the present study is to make clear the chemical behaviors of Pb based coolant in air ingress accident and the oxidation characteristics of Pb alloys. The thermodynamic consideration on the air ingress accident in the LBE cooled reactor was performed. The oxidation characteristics of Pb alloy were investigated by means of the static oxidation tests and metallurgical analysis of the oxidized Pb alloys.

2. Air ingress accident in lead based reactors [8]

Figure 1 shows the progression of physical and chemical events after air ingress accident in the LBE cooled reactor. The tube rupture in the air cooled type ECCS and RVACS is one of the possible causes for the air ingress accident. The chemical composition of air is $75.5N_2$-$23.1O_2$-$1.29Ar$-$0.05CO_2$ [wt%]. When the air ingress accident occurred in the low temperature region of the coolant system, the oxygen concentration in the coolant increases according to the dissolution of oxygen from the air bubbles. When the total inventory of LBE coolant is roughly assumed as $1x10^4$ tones, the soluble oxygen in the coolant is estimated as 15kg based on the oxygen solubility at 673K. Oxygen is promptly dissolved in the coolant due to the large affinity of the coolant with oxygen. When the air inflow rate is assumed as 100L/min in this accident, the oxygen concentration of the coolant reaches to the saturation condition within 10 hours. Nitrogen is not soluble in Pb and LBE. The molecules of CO_2 and H_2O are chemically stable in the coolant. Therefore, the air bubbles are never collapsed in the coolant. The oxygen depleted bubbles (i.e., Nitrogen bubbles) are transferred to the upward direction and escaped from the free surface (Arrow (1) in Fig. 1). Some bubbles may transport to the high temperature region (Arrow (2) in Fig. 1). The oxides are going to be generated in the coolant after the oxygen concentration reached to the saturate condition. The information about the oxidation characteristics of the lead based alloys is described in next chapter. In the flowing conditions, these oxides are transported to the various places in the coolant system. Then, the oxides selectively precipitate on the surface of heat transfer pipes in the heat exchanger, since the surface temperature of the heat transfer pipes is lower than the other place in the low temperature region and the heat exchanger works as so-called cold trap (Arrow (3) in Fig.1). Then, the heat transfer efficient is degraded due to the increase of heat transfer resistance by the layer of precipitated oxides, since the thermal conductivity of these oxides are much smaller than those of the metals. This situation causes unintended increase of the temperature of the coolant system and the reactor core. The erosion of the pump impeller by the solid oxide particles is also concerned (Arrow (4) in Fig.1). In the case of the air ingress accident caused in the high temperature region, the ingressed air simply contributed to the increase of the oxygen concentration in the coolant

(Arrow (5) in Fig.1).

The oxygen in the alloy is assumed to be dissolved and equilibrium state according to the Henry's law. Then, the oxygen potential in the liquid lead alloy is expressed as

$$\Phi = \Delta G^0_{\mathrm{Metal\ oxide}} + RT\ln\frac{C}{\mathrm{Cs}} \quad (1),$$

where $\Delta G^0_{\mathrm{Metal\ oxide}}$ is the Gibbs standard energy for formation of metal oxides, R is the gas constant, T is the temperature, C is the oxygen concentration, Cs is the oxygen solubility in the liquid metal. When the oxygen concentration in the liquid metal reaches to the saturation condition, the oxide is generated in the melt. The oxygen solubility in the coolant is larger at higher temperature, though the oxygen concentration is the same along the coolant loop. Therefore, the oxidation of the coolant is caused in the low temperature region before that in the high temperature region. The oxides must be dissolved in the coolant when the oxides transfer to the high temperature region from the low temperature region.

3. Oxidation characteristics of lead alloys [8]

The oxidation characteristics of lead alloys are investigated by means of the static oxidation tests in high-temperature air. The test samples are Bi, 30Pb-70Bi, LBE, Pb, Pb-17Li and Pb-5Li. Figure 2 shows the experimental procedure of the oxidation tests. The Pb-Bi and Pb-Li alloys were fabricated in the manner reported in previous paper [6]. The samples of Bi, 30Pb-70Bi, Pb and Pb-5Li were tested to investigate the effect of the chemical compositions of the alloy on the oxidation characteristics. The test conditions are summarized in Table 1. The oxidation tests were performed in the air at the temperature of 773K. This temperature is close to that in average along the coolant system of Pb or LBE cooled reactor. The size of the lead alloy samples is Φ26mm x 1.5mm, and the weight of the sample is approximately 16g. The sample was installed on the tray made of SUS304 (Fe-18Cr-8Ni). The SUS304 steel is one of the candidate materials of the structural material in the low temperature region in the reactor. The weight changes of the specimens were measured every fixed time period by an electro reading balance during the oxidation tests. The specimen surface was observed by the visual inspection. The molecular structures of the oxides formed on the sample surface were investigated by X-ray diffraction (XRD). Then, the specimen was cut at the span wise center. The cross sectional analysis of the specimens was performed by scanning electron microscope/energy dispersive X-ray analysis (SEM/EDX) and Laser Raman Spectroscopy (LRS). The corrosion of the SUS304 tray was also investigated. The concentration of Pb and Li in the oxides formed on the Pb-5Li and Pb-17Li samples were measured by Inductively Coupled Plasma Atomic Emission Spectroscopy (ICP-AES).

Figure 3 shows the results of the visual inspection for the oxidized samples. The analysis results for the oxidized samples indicated that PbO (Orange color) was preferentially formed on the Pb-Bi alloys, and then Pb was depleted from the matrix of the alloys by the oxidation. Then, Bi was not involved in this oxidation procedure. Lead bismuth oxide and Bi_2O_3 were formed only after the enrichment of Bi in the alloys due to the Pb depletion. The thickness of the oxide layer formed on the liquid LBE at static condition was approximately 1mm. The oxidation rates of the alloys were much larger than that of the steels. The oxidation rates of the Pb-Bi alloys become larger with higher Pb concentration in the alloy. The compatibility of Pb-Bi alloys with stainless steel can be worse when the Pb concentration in the alloy becomes low due to the oxidation, since the dissolution type corrosion is promoted by the Bi composition in the alloy.

The results of ICP-AES analysis for the oxides formed on the Pb-5Li and Pb-17Li samples (Fig.3) are summarized in Table 2. The results indicated PbO (Red color) and Li_2PbO_3 (Yellow color) were formed on the surface. The surface of the tray was covered by white portions, and the portions was Li_2CO_3. Li was depleted from the Pb-Li alloys due to its preferential chemical reactions in the air at 773K.

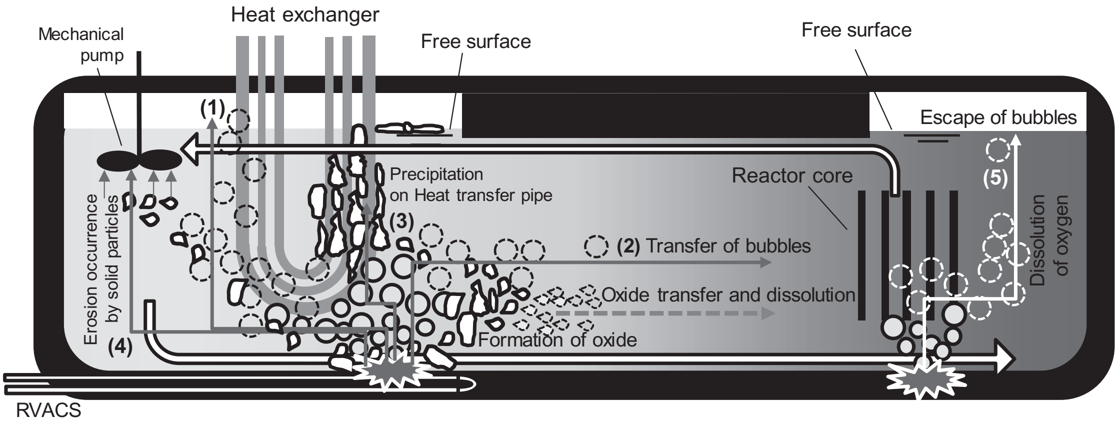

(a) Air ingression accident in low temperature region

(b) Air ingression accident in high temperature region

Fig. 1 Chemical and physical behaviors of lead bismuth coolant after air ingress accident

Acknowledgment

Authors would like to thank Prof. Minoru Takahashi, Prof. Toru Obara and Dr. Jun Nishiyama in Tokyo Institute of Technology for their fruitful discussions on the event of air ingress accident in lead based reactors.

Reference

[1] M. Kondo et al.: J. Nucl. Mater., Vol. 343, pp. 349-59 (2005).

[2] M. Kondo et al.: J. Nucl. Sci. Technol., vol. 43, pp.107-16 (2005).

[3] M. Kondo et al.: J. Nucl. Mater.; vol. 357, pp. 97–104 (2006).

[4] M. Kondo, M. Takahashi: J. Nucl. Mater., vol. 356, pp.203-212 (2006).

[5] A. Heinzel, M. Kondo, M. Takahashi: J. Nucl. Mater., vol.350, pp264-70 (2006).

[6] Y. Nakajima, M. Kondo, T. Nozawa; Fusion Eng. Des.: vol. 98–99, pp.2009–14 (2015).

[7] M. Kondo et al.: Plasma Fusion Res., vol.11, 2405076 (2016).

[8] M. Kondo et al.: The fifth international symposium on innovative nuclear energy systems, October 31- November 2, 2016, O-okayama, Tokyo P-28.

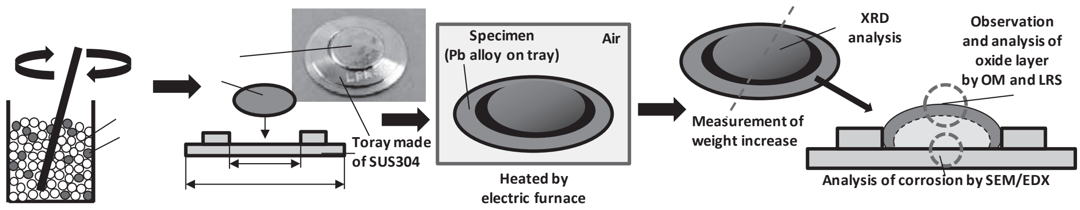

Fig. 2 Experimental procedure: (1) Fabrication of alloy, (2) Sample preparation, (3) Oxidation and (4) Analysis

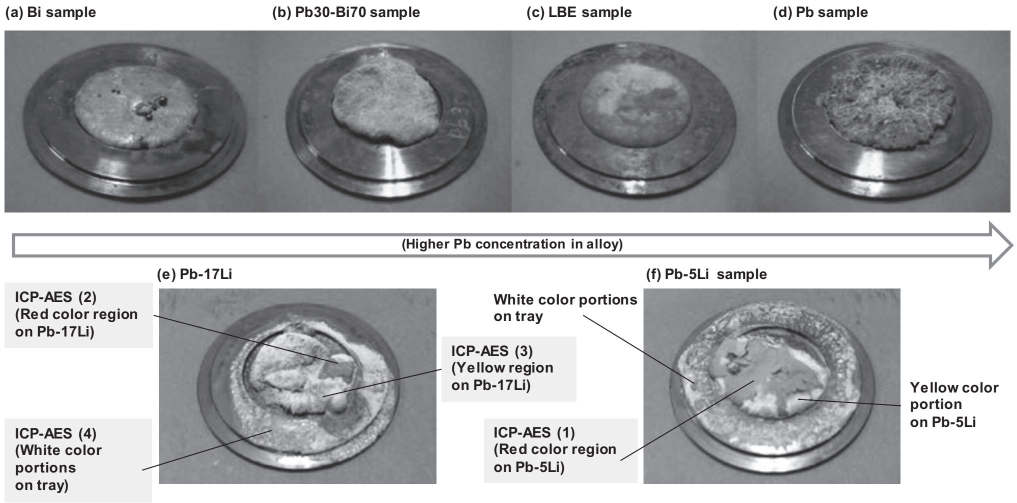

Fig. 3 Results of visual inspection for samples after oxidation test, (a) Bi, (b) Pb30-Bi70, (c) LBE, (d) Pb, (e) Pb-5Li and (f) Pb-17Li

Table 1 Experimental conditions of static oxidation tests

Samples (Purity: wt%)	Time [hour]	Temperature [K]	Analysis
Bi (99.98)	332	773	OM, SEM/EDX
Pb30-Bi70 (Pb: 99, Bi: 99.98)	312	773	OM, SEM/EDX, XRD
LBE: Pb44.5-Bi55.5 (C: 1×10^{-6}～1×10^{-7}wt%)	312	773	OM, SEM/EDX, LRS, XRD
Pb (99%)	332	773	OM, SEM/EDX, XRD
Pb-17Li [6] (Pb: 99.9, Li: 99)	308	773	ICP-AES
Pb-5Li [6] (Pb: 99.9, Li: 99)	308	773	ICP-AES

Table 2 Results of ICP-AES for oxidized samples of Pb-5Li andPb-17Li (wt%)

Sample	Mark	Region	Pb	Li	Residue	Possibility
Pb5Li	ICP-AES (1)	Red area	79.7	2.0	18.3	**PbO,** Li_2PbO_3, $PbCO_3$
Pb-17Li	ICP-AES (2)	Red area	96.2	0.1	3.7	**PbO,** Pb, $PbCO_3$
	ICP-AES (3)	Yellow area	54.7	7.8	37.5	**Li_2PbO_3,** PbO
	ICP-AES (4)	White portions	6.6	17.7	75.7	**Li_2CO_3**

B. Actinide Management Division

B.1 Outer-Sphere Extraction of Uranyl(VI) from HNO_3(aq) to 1-Butyl-3-methylimidazolium Nonafluorobutanesulfonate Ionic Liquid −Towards Decontamination of Uranium Wastes−

Koichiro Takao, Kohei Arakawa, Takahiro Mori, Masayuki Harada, and Yasuhisa Ikeda

1. Introduction

Ionic liquids (ILs) consist of only ionic species, and melt around room temperature or below 100°C, which is rather distinguishable from inorganic salts like NaCl (mp: 800°C). Because of these characters, ILs show several interesting traits, *e.g.*, low melting points, extremely low vapor pressure, high conductivity, and a wide electrochemical window. Especially, the negligibly low volatility of IL is highly favorable in the green chemistry, because its use may reduce environmental and health risks from chemical industrial processes like extraction in which volatile organic compounds (VOCs) used in ordinary processes are more or less released to the atmosphere. On this context, the extraction chemistry of various metal ions (M^{n+}) using ILs has been investigated extensively.[1]

Uranium-contaminated wastes are generated from the enrichment process in the nuclear fuel fabrication. To reduce load to the waste repository, these low-level radioactive wastes should be decontaminated. Use of IL is attracting a special interest as an alternative solvent in a chemical decontamination process for these wastes.[2,-4] To examine the applicability of ILs, it is necessary to understand fundamental extraction behavior of U(VI) in an aqueous/IL biphasic system.

Most previous studies regarding the extraction chemistry in ILs have focused on the extraction efficiency of M^{n+} from an aqueous solution to an IL employed, and dealt with a comparison with those obtained from the ordinary extraction systems using organic solvents. In contrast, little effort seems to be dedicated to recover the metal species distributed to the IL phase, although it is much desirable to recycle ILs for reduction of the secondary waste volume in actual processes. As ILs are hardly evaporated, concentration and drying are not practical. The most popular method to regenerate used ILs is back-extraction of M^{n+} to an aqueous phase with appropriately selected conditions (*e.g.*, acid concentration). However, such a stripping process is somewhat complicated and generates additional liquid wastes. Therefore, it is necessary to develop a simple strategy for the recovery of M^{n+} from ILs. Regarding U(VI), it is well-known that H_2O_2 strongly tends to precipitate U(VI) as uranyl peroxide ($UO_2(O_2).nH_2O$, n = 2, 4) in an aqueous solution. This method could be one of the feasible choices to recover U(VI) from IL and to facilitate the chemical decontamination process.

In this study, we investigated the partitioning behavior of U(VI) from an HNO_3 aqueous solution (aq) to 1-butyl-3-methylimidazolium nonafluorobutanesulfonate ([BMI][NfO], Figure 1) as well as its recovery by using H_2O_2(aq). Our aims are to examine the extraction efficiency of U(VI) in the HNO_3(aq)-[BMI][NfO] biphasic system and to demonstrate the recovery of the extracted U(VI) as uranyl peroxide.

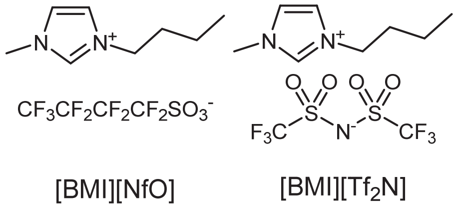

Fig. 1 Schematic structures of 1-butyl-3-methylimidazolium (BMI^+) ionic liquids of nonafluorobutanesulfonate (NfO^-, left) and bis(trifluoromethylsulfonyl)imide (Tf_2N^-, right) used in this study.

2. Experimental

2.1. Materials

The ionic liquid mainly used in this study, [BMI][NfO], was prepared in accordance with our former publication.[5] 1-Butyl-3-methylimidazolium bis(trifluoromethylsulfonyl)imide ([BMI][Tf_2N], Figure 1) was also synthesized through a method reported elsewhere. Distilled water was used to prepare aqueous samples. Uranyl nitrate hexahydrate and uranium trioxide were used as uranium sources. All other chemicals were of reagent grade, and used as received from Kanto Chemical Co., Ind.

2.2. Extraction Experiments

Aqueous solutions (1 mL) containing U(VI) (18.6 mM) and HNO_3 (0.010, 0.10, 0.50, 1.00, 3.00 M) were mixed with [BMI][NfO] (1 mL), which was pre-equilibrated with the blank HNO_3(aq). These biphasic mixtures were vigorously shaken at 298 K for 1 h. After centrifugation, the concentrations of U(VI) in the aqueous phases were determined by Perkin Elmer Optima 3000 ICP-AES. The distribution ratio (D) and extractability (E, %) were calculated using the following equations, respectively.

$$D = ([U(VI)]_{ini} - [U(VI)]_{aq})/[U(VI)]_{aq} \quad (1)$$

$$E = 100 \times ([U(VI)]_{ini} - [U(VI)]_{aq})/[U(VI)]_{ini} \quad (2)$$

where $[U(VI)]_{ini}$ and $[U(VI)]_{aq}$ denote the U(VI) concentrations in the aqueous phases at the initial state and after the extraction, respectively. Although volumes of aqueous and IL phases should also be taken into account in eq 1, they do not appear in this equation because their ratio in the current experiments is equal to 1.

Concentrations of BMI^+ and NfO^- transferred to the aqueous layer through the U(VI) extraction in the 0.010 M HNO_3(aq)-[BMI][NfO] system were determined by peak integrals in ^1H and ^{19}F NMR spectra, respectively (references: 50 mM CH_3COONa and 50 mM CF_3COOH), recorded by JEOL ECX-400 (^1H: 399.78 MHz, ^{19}F: 376.12 MHz). The extraction experiment at each condition was repeated at least 3 times, and the obtained data were merged.

The partitioning behavior of U(VI) in $HClO_4$(aq)-[BMI][NfO], $NaNO_3$(aq)-[BMI][NfO], and HNO_3(aq)-[BMI][Tf_2N] systems were also studied by the same protocol as the HNO_3(aq)-[BMI][NfO] system.

2.3. Recovery of Extracted U(VI) from [BMI][NfO]

From each of the [BMI][NfO] phases obtained after the abovementioned extraction experiments, 0.9 mL was transferred to an empty centrifuge tube. The distilled water (0.9 mL) and 30 wt% H_2O_2(aq) (0.5 or 1.0 mL) were also added to this tube. The mixture was vigorously shaken at 298 K for 10 min. After centrifugation, 0.5 mL was taken from the [BMI][NfO] layer, and loaded to another empty centrifuge tube. This [BMI][NfO] solution was mixed with 3.00 M HNO_3(aq) to strip U(VI) to the aqueous phase. The U(VI) concentration in the aqueous phase was evaluated by ICP-AES. Using this result and distribution ratio in the back-extraction system, the precipitation yield (*Y*, %) was calculated as follows.

$$Y = 100 \times (1 - D[\mathrm{U(VI)}]_{\mathrm{sup,b}}/[\mathrm{U(VI)}]_{\mathrm{IL}}) \qquad (3)$$

where $[\mathrm{U(VI)}]_{\mathrm{sup,b}}$ is the U(VI) concentration of the aqueous layer in the back-extraction using 3.00 M HNO_3(aq). The U(VI) concentration in [BMI][NfO] after the extraction is denoted by $[\mathrm{U(VI)}]_{\mathrm{IL}}$, namely $[\mathrm{U(VI)}]_{\mathrm{IL}} = [\mathrm{U(VI)}]_{\mathrm{ini}} - [\mathrm{U(VI)}]_{\mathrm{aq}}$. *D* is equal to 0.21 at $[HNO_3]$ = 3.00 M which was evaluated in the extraction experiment in Section 2.2. The pale yellow precipitate after addition of H_2O_2 was collected by filtration, and subjected to recording its powder X-ray diffraction (XRD) pattern by using Bruker D2PHASER diffractometer (Cu-Kα: λ = 1.5418 Å).

3. Resutls and Discussion

3.1. Extraction Behavior of U(VI) from HNO_3(aq) to [BMI][NfO]

Dependency of *D* on $[HNO_3]$ is displayed as solid circles in Figure 2. It is noteworthy that U(VI) was extracted from HNO_3(aq) to [BMI][NfO] despite no addition of any other extractants. This means that [BMI][NfO] in itself exhibits ability to extract U(VI). The *D* value decreased with an increase in $[HNO_3]$ from 0.010 to 1.00 M, while it slightly increased at the higher $[HNO_3]$. When 5 M HNO_3(aq) was employed as an aqueous phase, its mixture with [BMI][NfO] no longer formed the biphasic system.

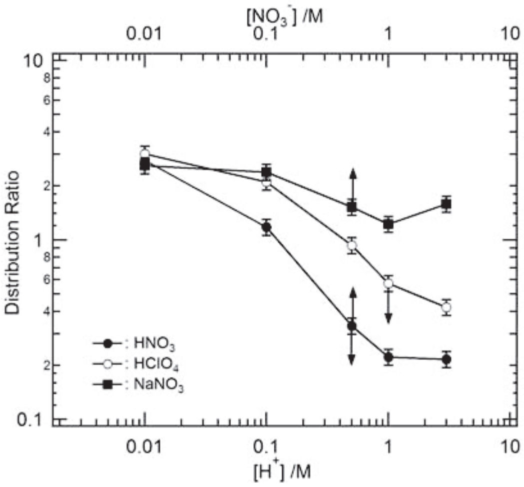

Fig. 2 Distribution ratio (*D*) of U(VI) as a function of $[H^+]$ or $[NO_3^-]$. Solid circles and squares display results from the extraction experiments in use of HNO_3 and $HClO_4$, respectively. Open circles represent the dependency of *D* on $[NO_3^-]$, where $[H^+]$ was fixed to 0.010 M using HNO_3.

The tendency of *D* towards $[HNO_3]$ may provide us a mechanistic insight about the extraction behavior of U(VI) in this system, *i.e.*, $[H^+]$, $[NO_3^-]$, or both of them are involved in the extraction. To clarify this point individually, we first performed the same experiments in use of $HClO_4$(aq) instead of HNO_3(aq). The results are also shown as solid squares in Figure 2. The data point at $[HClO_4]$ = 3 M is missing, because the mixture of 3 M $HClO_4$(aq) and [BMI][NfO] no longer forms a biphasic system. Although the similar trend of *D* on $[H^+]$ was observed in both systems, a distinguishable deviation of *D* in the $HClO_4$(aq)-[BMI][NfO] system from that in HNO_3(aq)-[BMI][NfO] was found at each $[H^+]$ condition. It is widely accepted that ClO_4^- hardly interacts with M^{n+} including UO_2^{2+}, while the coordination of NO_3^- to UO_2^{2+} is usually observed. Therefore, such a deviation could be ascribed to formation of less-extractable species resulted from complexation between NO_3^- and UO_2^{2+}. To examine this hypothesis, we also studied the extraction behavior of U(VI) in $NaNO_3$(aq)-[BMI][NfO] system, where $[H^+]$ was fixed at 0.010 M and $[NO_3^-]$ was varied by dissolving $NaNO_3$ to the aqueous phase. The results are also displayed as open circles in Figure 2. As expected, *D* gradually decreases with an increase in $[NO_3^-]$ up to 0.50 M, while *D* reaches plateau in the higher $[NO_3^-]$ range. In summary, the extraction of U(VI) in the current systems is mainly governed by $[H^+]$, while $[NO_3^-]$ also shows the minor contribution to prevent partitioning of U(VI) to [BMI][NfO].

The conventional slope analysis for Figure 2 would provide us no quantitative information on extraction mechanisms of U(VI), because each set of data points does not follow a straight line, but rather bent. This situation could arise from the significantly different ionic strength conditions in the present systems, which affects activity coefficients of the related species. Therefore, it is not possible to quantitatively and thermodynamically evaluate the observed extraction behavior. However, the observed dependency on [NO_3^-] may imply that the coordination of NO_3^- disturbs the extraction of U(VI) to [BMI][NfO]. Although the species distribution of UO_2^{2+}-NO_3^- complexes is still unclear, $[UO_2(OH_2)_5]^{2+}$ predominantly occurs in 0.01 M HNO_3(aq), where the highest extractability was observed in the HNO_3(aq)-[BMI][NfO] systems tested. This means that the extracted U(VI) species is the pentaaqua complex. Furthermore, the remarkable effect of [H^+] is indicative of participation of H^+ in the extraction. Under the acidity conditions studied here, the hydrolysis of UO_2^{2+} can be ruled out. Taking into account the extraction ability of [BMI][NfO], one of the components of this IL, BMI^+ or NfO^-, should contribute to the extraction.

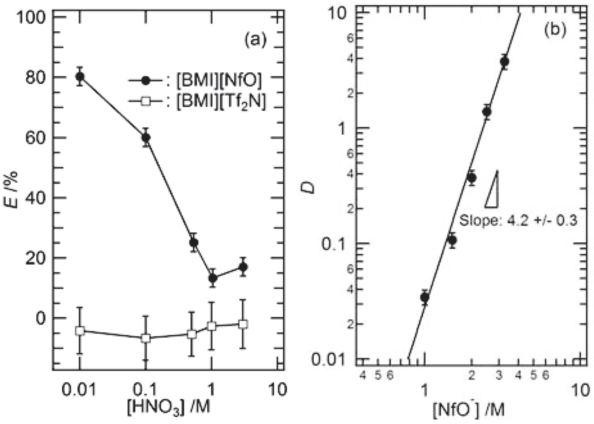

Fig 3 Extraction behavior of U(VI) in HNO_3(aq)-[BMI][Tf_2N] systems. In panel (a), extractability is compared with that in HNO_3(aq)-[BMI][NfO]. Panel (b) shows dependency of *D* as a function of [NfO^-] together with the best fit line resulted from the least-squares regression ([HNO_3] = 0.010 M).

To further clarify the above matter, we studied the extraction of U(VI) from HNO_3(aq) to another IL, [BMI][Tf_2N] (Figure 1), which dissolves [BMI][NfO] as an extractant. Prior to starting this experiment, it was necessary to perform blank tests to confirm that [BMI][Tf_2N] does not have the extraction ability for U(VI). The result is shown in Figure 3a together with those observed in HNO_3(aq)-[BMI][NfO], where the extraction efficiency is displayed in terms of extractability (*E*, %). Consequently, no meaningful extraction was detected in the HNO_3(aq)-[BMI][Tf_2N] systems in the whole range of [HNO_3] tested, indicating that [BMI][Tf_2N] just plays a spectator role unlike [BMI][NfO]. Therefore, the effect of [NfO^-] on the extraction of U(VI) can be investigated solely. We selected 0.01 M HNO_3(aq) as the aqueous phase, because the extraction of U(VI) is most significant. Furthermore, the coordination of NO_3^- is negligible at this condition as described above. Figure 3b shows the full-logarithmic plot of *D* versus [NfO^-] in the 0.010 M HNO_3(aq)-[BMI][Tf_2N] systems. The least-squares regression resulted in the slope of the best fit line as 4.2 ± 0.3. This means that four NfO^- ions are involved in the extraction of U(VI).

While the perfluorinated butyl group of NfO^- reminds us that this anion is a very weak ligand for UO_2^{2+} because of the extremely diluted negative charge on the sulfonate moiety, the coordination bond between UO_2^{2+} and NfO^- has actually been demonstrated in a crystalline $UO_2(NfO)_2$(tetrahydrofran)$_3$ by our group. To clarify whether or not such a coordination interaction is formed in the current extraction system, we recorded UV-vis absorption spectra of U(VI) in both layers of the $HClO_4$(aq)-[BMI][NfO] extraction system ([$HClO_4$] = 0.010 M). The results are displayed in Figure 4 together with that of $[UO_2(OH_2)_5]^{2+}$ in 0.010 M $HClO_4$(aq). Interestingly, all the spectra displayed are almost identical to each other, indicating that $[UO_2(OH_2)_5]^{2+}$ is present as is in both aqueous and [BMI][NfO] phases even after the extraction. Thus, the coordination strength of NfO^- is so weak that no direct bonds can be formed between UO_2^{2+} and NfO^- in the studied extraction systems.

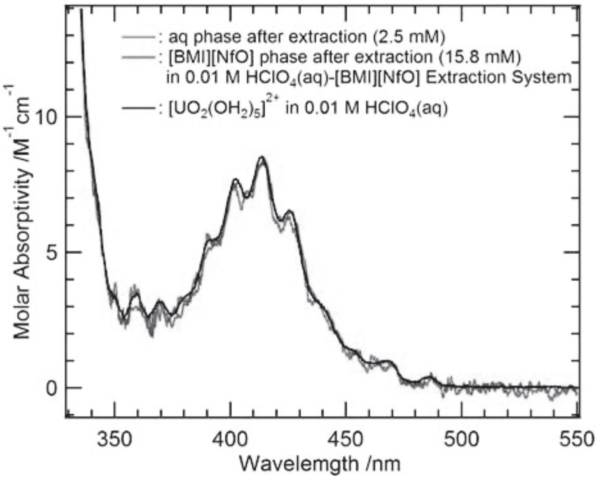

Fig. 4 Molar absorption spectra of U(VI) in both phases of the 0.010 M $HClO_4$(aq)-[BMI][NfO] extraction system (green: aqueous, red: [BMI][NfO]) together with that of $[UO_2(OH_2)_5]^{2+}$ in 0.01 M $HClO_4$(aq) (black).

In contrast, we have found that four NfO^- are involved in the extraction of $[UO_2(OH_2)_5]^{2+}$ as demonstrated in Figure 3. The most plausible explanation for these findings would be formation of an outer-sphere complex like $\{[UO_2(OH_2)_5](NfO)_4\}^{2-}$. Although it is quite difficult to obtain an experimental evidence supporting this hypothesis, the outer-sphere coordination sometimes effectively assists extraction of charged metal complexes like $[MCl_n]^{x-}$ (M = Zn, Fe, Pt). While hydrogen bonding can be formed between the sulfonate moiety of NfO^- and the water molecules present in the first coordination sphere of UO_2^{2+}, the electrostatic attraction between $[UO_2(OH_2)_5]^{2+}$ and NfO^- is also likely to occur. As a matter of fact, Bell and co-workers employed the positive charge of tripodal hydrogen bonding receptors to let them come closer to $[PtCl_6]^{2-}$ by the Coulombic attraction. The perfluoronated butyl group of NfO^- interacting with

$[UO_2(OH_2)_5]^{2+}$ would be directed to the outwards of the $\{[UO_2(OH_2)_5](NfO)_4\}^{2-}$ outer-sphere complex to facilitate hydrophobic solvation in the [BMI][NfO] layer. Finally, the extraction of U(VI) is driven. This conclusion does not indicate extraordinarily strong interaction of NfO^- with $[UO_2(OH_2)_5]^{2+}$ in [BMI][NfO]. Such an outer-sphere coordination seems to rely on very high $[NfO^-]$ in [BMI][NfO] (*ca.* 3.4 M = 1473 $g\cdot dm^{-3}/438.31\ g\cdot mol^{-1}$), while the solubility of NfO^- in the aqueous phase is only 10-20 mM determined by ^{19}F NMR spectroscopy. Thus, the outer-sphere complex practically occurs only in [BMI][NfO]. It is noteworthy that Tf_2N^- is not potential to play such a prominent role in the U(VI) extraction.

In summary, the extraction of U(VI) in the 0.01 M $HNO_3(aq)$-[BMI][NfO] system should proceed through the following reaction.

$$[UO_2(OH_2)_5]^{2+}{}_{aq} + 4\ NfO^-{}_{IL} = \{[UO_2(OH_2)_5](NfO)_4\}^{2-}{}_{IL} \qquad (4)$$

where subscripts *aq* and *IL* indicate location of the species. The equilibrium constant of eq 4, namely distribution coefficient (K_d), is equal to $D[NfO^-]^{-4}$. From the dependency of D on $[NfO^-]$ shown in Figure 3b, log K_d was evaluated as −1.47 ± 0.01 at 298 K.

Through progress of eq 4, the charge distribution in both phases must be compensated successively. To satisfy this requirement, there are two possible pathways, *i.e.*, (i) exchange reaction between $[UO_2(OH_2)_5]^{2+}{}_{aq}$ and two cations present in [BMI][NfO] and (ii) ion pair formation of $[UO_2(OH_2)_5]^{2+}$ with two anions in the aqueous phase. In mechanism (i), the cationic exchanger can be BMI^+ or H^+. The anionic species responsible for mechanism (ii) can be NfO^- or NO_3^-. To find a reliable extraction mechanism, we determined the concentration of BMI^+ and NfO^- distributed to the aqueous phase of the 0.01 M $HNO_3(aq)$-[BMI][NfO] biphasic system by using ^1H and ^{19}F NMR spectroscopy, respectively. As a result, any remarkable differences in $[BMI^+]$ and $[NfO^-]$ in the aqueous phase were not detected through the extraction of 14.9 mM U(VI). Therefore, contribution of BMI^+ and NfO^- in mechanism (i) and (ii), respectively, can be ruled out. Furthermore, we can immediately get to know that NO_3^- does not form the extractable ion pair with $[UO_2(OH_2)_5]^{2+}$ in mechanism (ii), because little $[NO_3^-]$ dependency has been observed in Figure 2. If an ion pair like $[UO_2(OH_2)_5]^{2+}\cdot 2NO_3^-$ is extracted to [BMI][NfO], D in Figure 2 will increase with an increase in $[NO_3^-]$. However, this is not the case in the actual situation. In contrast, D clearly decreases with increasing $[H^+]$ in Figure 2. This result implies attendance of H^+ in the extraction of U(VI), while acidity of NfOH is so strong that protonation of NfO^- to form NfOH is quite unlikely to occur. It is reasonable to assign the role of H^+ in the U(VI) extraction to the cation exchanger with $[UO_2(OH_2)_5]^{2+}$ in mechanism (ii). In conclusion, the extraction of U(VI) in the 0.01 M $HNO_3(aq)$-[BMI][NfO] system proceeds through a combination of the cation exchange with $H^+{}_{IL}$ and outer-sphere complexation with $NfO^-{}_{IL}$ like eq 5.

$$[UO_2(OH_2)_5]^{2+}{}_{aq} + 4\ NfO^-{}_{IL} + 2\ H^+{}_{IL} = \{[UO_2(OH_2)_5](NfO)_4\}^{2-}{}_{IL} + 2\ H^+{}_{aq} \qquad (5)$$

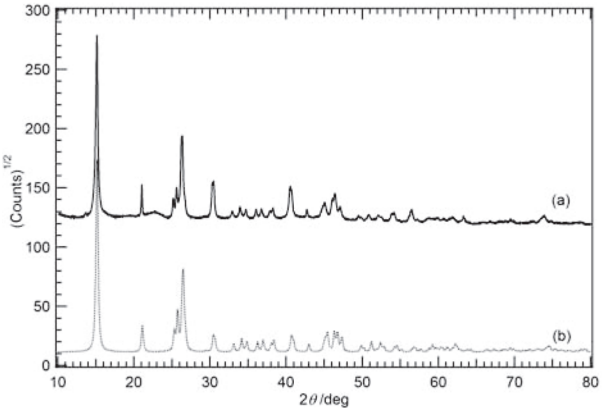

Fig. 5 Powder XRD pattern of (a) pale yellow precipitate collected from [BMI][NfO] after addition of 30 wt% $H_2O_2(aq)$ together with (b) that of studtite ($[(UO_2)(O_2)(H_2O)_2]\cdot 2H_2O$) calculated on the basis of its reported crystallographic data (fwhm = 0.3° fixed).

3.2. Recovery of U(VI) from [BMI][NfO] after Extraction

When 30 wt% $H_2O_2(aq)$ (0.5 mL) was added to the [BMI][NfO] solution containing U(VI) (5.5 mM), pale yellow and finely powdered precipitate was formed after the vigorous stirring and centrifugation. The XRD pattern of this solid compound (Figure 5) is in fair agreement with that of uranyl peroxide tetrahydrate, $[(UO_2)(O_2)(H_2O)_2]\cdot 2H_2O$ (studtite). Figure 6 shows the precipitation yield (Y, %) as functions of (a) $[HNO_3]$ used in the preceding extraction experiments and (b) pH in the aqueous phase at the equilibrium (pH_{eq}). As a result, Y is independent of the volume of added 30 wt% $H_2O_2(aq)$ under the current conditions. In contrast, Y clearly tends to increase with an increase in pH_{eq} (48.1% at pH_{eq} = 0.43, 96.2% at pH_{eq} = 2.08). This tendency is in line with the formation of $[(UO_2)(O_2)(H_2O)_2]\cdot 2H_2O$ involving deprotonation from H_2O_2 as follows.

$$UO_2{}^{2+} + H_2O_2 + 4\ H_2O = [(UO_2)(O_2)(H_2O)_2]\cdot 2H_2O\downarrow + 2\ H^+ \qquad (6)$$

The efficiency of this method to precipitate U(VI) as uranyl peroxide has already been established in aqueous solution. We also confirmed that Y in the aqueous system is ranging from 96.9 to 98.0% at pH_{eq} = 0.43-1.47 as presented by solid triangles in Figure 6. In contrast, the current results in Figure 6 indicate that this precipitation method in [BMI][NfO] is not as efficient as that in the aqueous system, although the activities of H^+ in the [BMI][NfO] solutions are not necessarily the same with pH_{eq}.

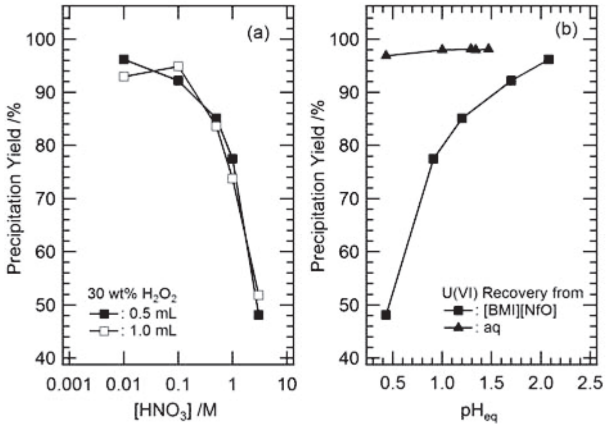

Fig. 6 Precipitation yield (*Y*) of U(VI) as functions of [HNO_3] (a) and pH at equilibrium (pH$_{eq}$, (b)) after addition of 30 wt% H_2O_2(aq). In panel (a), the transverse axis represents the HNO_3 concentration used in the preceding extraction experiments.

4. Conclusion

In this study, we investigated extraction chemistry of U(VI) in the HNO_3(aq)-[BMI][NfO] biphasic systems. As a result, it was clarified that [BMI][NfO] is not simply a spectating organic solvent, but its anionic component, NfO$^-$, is rather prominent in the extraction of U(VI) to form the outer-sphere complex like $\{[UO_2(OH_2)_5](NfO)_4\}^{2-}$ in [BMI][NfO]. Furthermore, the extraction of U(VI) seems to compete with the coordination interaction of NO_3^-. Finally, the following overall extraction mechanism was proposed for the 0.01 M HNO_3(aq)-[BMI][NfO] system; $[UO_2(OH_2)_5]^{2+}$ is transferred to [BMI][NfO] together with back-extraction of H^+ to compensate the charge balance in both phases, followed by the outer-sphere coordination with NfO$^-$ to give $\{[UO_2(OH_2)_5](NfO)_4\}^{2-}$ in the IL phase. The extracted U(VI) in [BMI][NfO] was successfully recovered by addition of H_2O_2(aq), although the efficiency is not as well as that in the aqueous system. As expected, the precipitate was assigned to the uranyl peroxide tetrahydrate, $[(UO_2)(O_2)(H_2O)_2]\cdot 2H_2O$ (studtite), by means of the powder XRD analysis. The experimental results obtained here are helpful to consider applicability of [BMI][NfO] to the chemical decontamination processes for uranium-contaminated low-level wastes. To assess the recyclability of [BMI][NfO] in the proposed decontamination process, it is also necessary to clarify chemical stability of this IL upon contact with HNO_3 as well as H_2O_2, although no degradation was observed in the NMR spectra under the experimental conditions currently investigated.

Acknowledgment

This work was supported by JSPS KAKENHI Grant Number 24360390, Grant-in-Aid for Scientific Research (B).

Reference

1. K. Takao, T. J. Bell, Y. Ikeda, *Inorg. Chem.* **2013**, *52*, 3459.
2. Y. Ohashi, N. Asanuma, M. Harada, Y. Wada, T. Matsubara, Y. Ikeda, *J. Nucl. Sci. Technol.* **2009**, *46*, 771.
3. K. Sasaki, T. Suzuki, T. Mori, T. Arai, K. Takao, Y. Ikeda, *Chem. Lett.* **2014**, *43*, 775.
4. T. Mori, K. Takao, K. Sasaki, T. Suzuki, T. Arai, Y. Ikeda, *Sep. Purif. Technol.* **2015**.
5. K. Takao, T. Takahashi, Y. Ikeda, *Inorg. Chem.* **2009**, *48*, 1744.

B.2 Development of Poly(NIPAAm) Gel-Enclosing Photonic Crystal on a Microchip for Metal Ion Sensing

Kaname Saga, K-C. Park, and Takehiko Tsukahara

The analysis of metal ions in radioactive wastes generated from nuclear facilities has become of a critical issue for the environmental safety, in particular, strontium ion (Sr^{2+}) is one of the most harmful elements. Although complicated instruments are generally utilized for such analysis, they require time-consuming chemical operations and produce large amounts of secondary wastes. Accordingly, simple sensing methods of metal ions should be established. Our previous studies showed that poly-N-isopropylacrylamide (poly(NIPAAm)) grafted on silica matrixes makes it possible to adsorb and desorb metal ions by only temperature changes.[1,2] Therefore, in this study, we aim to develop on-chip metal ion sensor composed by poly(NIPAAm) gel-enclosing PC. The swelling/shrinking behavior of poly(NIPAAm) gel based on adsorption/desorption of target metal ions can lead to changes of diffraction wavelength (λ) of PC, *i.e.*, color changes, according to Bragg-Snell law (see Eq. (1)).

$$\lambda = 2D(n^2 - \sin^2\theta)^{1/2} \qquad (1)$$

where D, n, and θ are the lattice spacing of crystal, the refractive index, and the incidence angle, respectively.

Square-shaped microstructures with μm-deep/mm-width and μm-deep/μm-width were fabricated on quartz substrates by polyimide tapes and SU-8 photolithographic processes, respectively. After a dimethylformamide solutions consisting of 100 nm-sized colloidal silica particles, IPAAm monomer, *N,N*-Methylenebisacrylamide crosslinking agent, and 2-Hydroxy-2-methylpropiophenone initiator was shaken and dialyzed, the solution was dropped onto the microstructures. Photo-polymerization syntheses of poly(NIPAAm) gel were performed by irradiating UV light (365 nm, 500 W) at 240 sec under Ar gas. The irradiated areas on each substrate were colorless immediately after polymerization, but exhibited metallic-blue color at an ambient temperature by adding pure water (Fig. 1). This result means that the poly(NIPAAm) gel-enclosing self-assembled colloidal silica particles could act as PC and change the periodic structures with shrinking/swelling of gel.

The poly(NIPAAm) gel-enclosing PC [poly-gel-PC] was filled with pure water, and temperature-dependence of colors and diffraction spectra for the water-filled poly-gel-PC was examined by microscope and fiber-optic reflectance spectrometer. As shown in Fig. 2, we found that the poly-gel-PC had bluish-green color at 15 °C, while the color changed gradually to blue with increasing temperatures up to 30 °C and approached to the colorless at 34 °C. The diffraction spectra also appeared that the peaks were shifted at the wavelength from about 540 to 300 nm with an increase in temperatures.

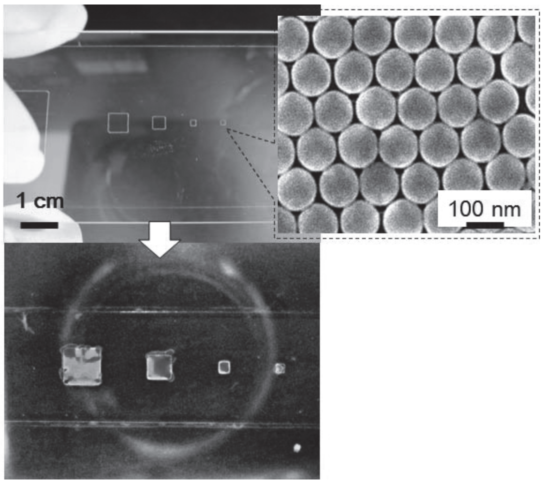

Fig. 1 Pictures and a SEM image of SU-8-typed poly-gel-PC microchip.

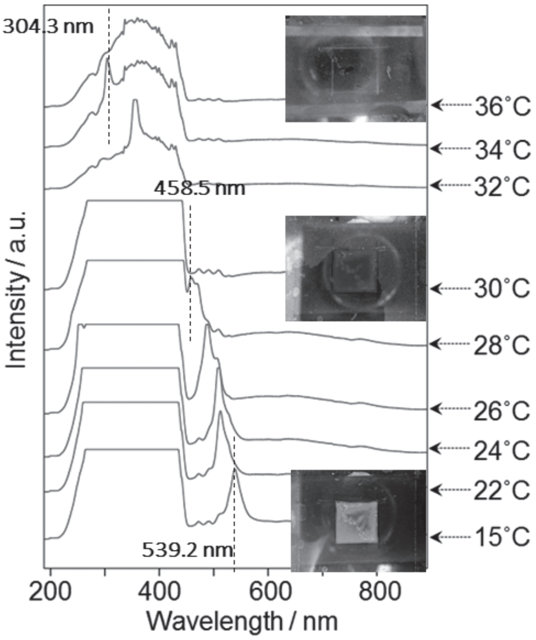

Fig. 2 Temperature dependence of signal intensities and color changes of poly-gel-PC microchip.

When the solution containing Sr^{2+} was dropped onto the poly-gel-PC at 15 °C, the structural color was drastically and instantaneously changed from blue to colorless, because of reduction of interparticle distances accompanying with gel-shrinking. When the removal of residual Sr^{2+} solution and the drop of pure water onto poly-gel-PC were performed, the recovery of color from colorless to initial blue could be observed, because of gel-swelling and expansion of interparticle distances (Fig. 3). This fact proves that the fabricated poly-gel-PC on a chip has metal ion sensing performances.

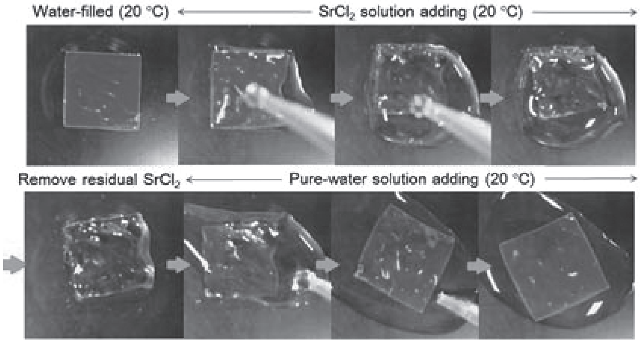

Fig. 3 Pictures of Sr ion sensing using the synthesized poly-gel-PC on a chip at 20 °C. We can observe rapidly color changes from blue to colorless.

In conclusion, we succeeded in the development a simple stimuli-responsive microchip for metal ion sensing, in which target metal ions can be selectively detected according to changes of diffraction spectra of poly(NIPAAm) gel enclosing PC.

This work was supported by the Initiatives for Atomic Energy Basic and Generic Strategic Research (260402) from the Ministry of Education, Culture, Sports, Science and Technology (MEXT).

References

1. T. Tsukahara, and N. Idota, “Temperature-swing Microfluidic Separation of Uranyl Ions Using Thermoresponsive Copolymer Brushes”, *Chem. Lett.*, 1381 - 1382, 2011.
2. E. P. Weather, “Synthesis of NIPAAm-based polymer-grafted silica beads by surface-initiated ATRP using Me4Cyclam ligands and the thermo-responsive behaviors for lanthanide(III) ions” , *Reactive and Functional Polymers*, 79, 36 - 46, 2014.

B.3 Celestite Precipitation-Induced Diffusion Behavior of $^{36}Cl^-$, $^{22}Na^+$, and HTO in Compacted Illite

Y. Fukatsu, L.R. Van Loon, A. Shafizadeh, D. Grolimund, Y. Ikeda, and T. Tsukahara

Understanding of migration of radionuclides in sedimentary rocks consisted of natural compacted clay plays an important role for long term safety assessments of radioactive waste disposal system. The sedimentary rocks have various pore spaces between the grains, and the radionuclides can be spread into the biosphere on the flow of groundwater in the pores. Practically, since dissolution and precipitation of clay minerals are generated by groundwater including anions such as SO_4^{2-} and/or CO_3^{2-}, size distribution, porosity, and tortuosity of the pores in sedimentary rocks are significantly changed depending on the underground environment, and unexpected migration behavior of radionuclides should be induced. Therefore, in the present study, we aim to evaluate the effect of precipitation in highly compacted clay on the diffusion behavior of ion species by means of chemical tracer experiments.

We developed a tracer experimental system as shown in Fig. 1. A compacted illite (cylindrical pellet with inner diameter of 5 mm and height of 10 mm) was fabricated by a high-press instrument, and the precipitation of celestite ($SrSO_4$) in the pores of compacted illite were applied by cross-diffusion of strontium chloride and sodium sulfate solution. The position of celestite precipitation inside the pores were measured with neutron radiography [1]. The results showed that the selective clogging in the pores at the center of the compacted illite were succeeded.

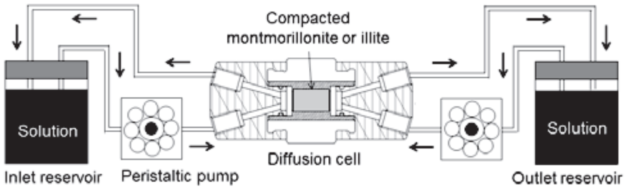

Fig. 1. Schematic illustration of the tracer experiment system.

The tritiated water (HTO) and aqueous solution containing $^{22}Na^+$ and $^{36}Cl^-$ ions were introduced into illite sample with celestite precipitation, and the solution through the illite sample were recovered into an aqueous solution located at the outlet reservoir. The results show in Fig. 2. By measuring time dependence of the radioactivity of the recovered solution, the effective diffusion coefficients (*D*) of HTO, $^{22}Na^+$, and, $^{36}Cl^-$ in the illite sample with celestite precipitation were evaluated. The resulting *D* values of HTO and $^{22}Na^+$ were found to be lower than those in the compacted illite without precipitation. This fact indicates that water and cations can be migrated even in much smaller pores produced by celestite precipitation. On the other hand, the diffusion of $^{36}Cl^-$ passed through in the illite sample didn't occur. Such prevention of diffusion of anion could be characterized by the anion exclusion effect, which was induced by electric double layer overlap of the negatively-charged illite grain surfaces [2].

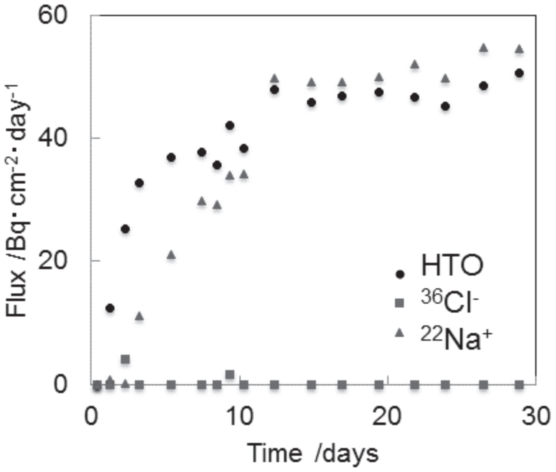

Fig. 2 Time dependence of flux of HTO, $^{22}Na^+$, and, $^{36}Cl^-$.

In conclusion, we clarified the effects of celestite precipitation in compacted illite on the diffusion of HTO, $^{36}Cl^-$ and $^{22}Na^+$ by using tracer through-diffusion experiments. These findings are important information for understanding the migration of radionuclides in sedimentary rocks.

This work was partially supported by Support for Tokyotech Advanced Researchers (STAR) from Tokyo Institute of Technology.

References

1. A. Shafizadeh, T. Gimmi, L. Van Loon, A. Kaestner, E. Lehmann, U.K. Maeder, S.V. Churakov, Physics Procedia, 2015, 69, 516.
2. Luc R. Van Loon, Martin A. Glaus, Werner Müller, Applied Geochemistry, 2007, 22, 2536.

B.4 Development of Separation Process of PGMs and Mo from HLLW for the Stable Operation of Vitrification Process

Kenji Takeshita, Yusuke Inaba, Hideharu Takahashi, Miki Harigai

In the production process of vitrified object by the LFCM (Liquid Fed Ceramic Melter) in Japan, both high level liquid waste (HLLW) and glass frit are supplied directly in the glass melter and heated to 1200ºC by the Joule heating method using electrodes. The molten glass containing metal oxides is flowed out from the melter and solidified in a canister.

However, platinum group metals (PGMs) such as Pd, Ru and Rh in HLLW form flocs. The flocs are deposited on the side wall of melter. The apparent viscosity of molten glass is increased by the addition of flocs and the mobility of molten glass becomes worse. Therefore, the molten glass with frocs cannot be released stably from the melter and the continuous operation of the melter is disturbed. Molybdenum (Mo) is also a trouble element, which is present as molybdate in molten glass and cause the formation of low viscous phase called yellow phase. To avoid these problems, two special operations, such as the HLLW dilution and the melter washing, are carried out. In the HLLW dilution, total concentration of PGMs in HLLW is arranged. In the melter washing, the melter is cleaned by adding only glass frit. As a result, the number of generated glass bodies is increased to more than twice of those with no operations.

In this study, we are developing a simultaneous removal process of PGMs and Mo from HLLW for the decrease in the number of glass bodies and the stable operation of glass melter. As shown in Fig.1, the proposed process consists of four steps, such as the simultaneous adsorption of Mo and PGMs from HLLW by an inorganic adsorbent, the thermal decomposition of adsorbent adsorbing Mo and PGMs, the leaching of Mo and PGMs from the residue by HNO_3 (or H_2O) and the separation of Mo and PGMs from the leachate by solvent extraction.

In this paper, we report the selection of inorganic adsorbent suitable for the simultaneous adsorption of PGMs and Mo from HLLW.

3 mol/L HNO_3 solution with 1mmol/L of $Pd(NO_3)_2$, $Ru(NO_3)_3$ and $Rh(NO_3)_3$ was prepared and the adsorption of PGMs into antimony compounds, phosphorus compounds and ferrocuanide compounds was tested. PGMs were little adsorbed in Sn antimonite, Zr antimonite and Zr phosphonate. Low adsorption performance of PGMs was observed only for Ti antimonite. On the other hand, Cu ferrocyanide adsorbed Pd completely and Ru and Rh with high adsorption efficiency. These results suggest that metal ferrocyanide is the most suitable for the adsorption of PGMs.

Subsequently, we synthesized various metal ferrocyanides such as Fe / Al / Cu ferrocyanides, etc., moreover, the simultaneous adsorption of PGMs and Mo from a simulated HLLW (sHLLW) with 26 elements was tested by the ferrocyanides. Al ferrocyanide adsorbed Pd completely and Ru, Rh and Mo with high adsorption efficiency, moreover, no adsorption of rare earth elements by Al ferrocyanide was confirmed, compared with other metal ferrocyanides. These result suggest that Al ferrocyanide has the selective separation performance of PGMs and Mo.

In this work, we proposed a new separation system of PGM and Mo from HLLW for the quality improvement and volume reduction of vitrified object. The screening tests to select an appropriate inorganic adsorbent were carried out. As a result, we found that the selective separation of PGMs and Mo from HLLW can be accomplished by Al ferrocyanide.

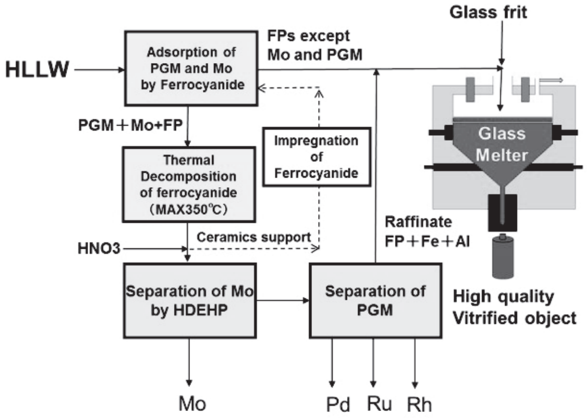

Fig. 1 Separation process of PGMs and Mo from HLLW

Acknowledgments

This work was financially supported by “The Initiatives for Atomic Energy Basic and Generic Strategic Research” and “ Innovative Nuclear Research and Development Program” organized by the Ministry of Education, Culture, Sports, Science and Technology of Japan.

Reference

1. K. Takeshita, Y. Inaba, H. Takahashi, *MARC X*, Honolulu, USA, April 12-17, 2015, 560.
2. K. Takeshita, Y. Inaba, H. Takahashi, J. Onoe, H. Narita, *GLOBAL2015*, Paris, France, September 21-24, 2015, 5387.
3. J. Onoe, S. Watanabe, M. Nakaya, Y. Sawada, M. Yoshida, Y. Inaba, T. Nagasaki, H. Matsuda, H. Takahashi, K. Takeshita, T. Kameyama, T. Torimoto, *EMCMRE-3*, Marrakech, Morocco, November 2-6, 2015.

And other 24 publications (related with this study in FY 2015).

B.5 Development of a Granulation Method for Iron(III) Ferrocyanide by Thin-film Polymer Gel Coating[1)]

Yusuke Inaba, Miki Harigai, Kenji Takeshita

1. Introduction

After the Fukushima Daiichi Nuclear Power Plant Accident, a large amount of radioactive material was released into the atmosphere. The main radioactive contaminant was ^{137}Cs, which has a half-life of about 30 years. Iron (III) ferrocyanide, also known as Prussian blue (PB), and its analogs are well-known Cs adsorbents and exhibit high selectivity and high adsorption capability towards Cs. However, the separation of PB from the contaminated water is difficult after Cs adsorption because the very small PB particles (10-20 nm) disperse well in the water. If the PB particles are granulated to form particles that are larger in size (several microns), they can be easily recovered from water and the granulated PB can be used as a column packing material.

Therefore, we have devised a new granulation method for PB and have incorporate them onto porous carriers by thin-film polymer gel coating.

2. Results and discussion

Firstly, experiments related to the preparation of PB supported on porous silica gel by the thin-film gel coating method were conducted. Figure 1 shows the process for the synthesis of the composite adsorbent, PB supported on silica (PBS).

The PB (Dainichiseika Color & Chemicals Mfg. Co., Ltd.) used in this study was dried for more than 24 h under a pressure of 0.09 MPa. After the addition of PB (50, 100, 200, 400 mg), 1.5 mL of dimethylformamide (DMF) as a solvent, 0.5 mL (5.0 mmol) of *N*,*N*-dimethylacrylamide (DMAA) as a monomer, and 80 mg (0.5 mmol) of *N*,*N'*-methylene- bisacrylamide (BIS) as a crosslinking agent into a 20 mL vial, the PB particles in the monomer solution were well-dispersed by ultrasonic waves for 20 min. N_2 was subsequently bubbled through the monomer solution for 3 min in order to remove oxygen. The PB was dispersed again by ultrasonication for 20 min after the addition of 100 mg (0.6 mmol) of 2,2'-azobis(isobutyronitrile) (AIBN) as the initiator. Subsequently, porous silica gel (Fuji Silysia Chemical, Ltd., diameter 50 μm, pore size 700 nm) was added into the monomer solution containing the PB particles and was impregnated with the PB particles for 24 h under pressure (0.03 MPa) at 25°C. In this process, the monomer solution containing PB particles was drawn into the micro pores of the porous silica gel by capillary action. By heating for 24 h at 85°C, the PB particles were supported onto the surface of the porous silica gel via the formation of a thin-film polymer gel. After polymerization, the blue colored parts of the sample were separated and rinsed several times using distilled water and wet PBS (3.5 g) was obtained.

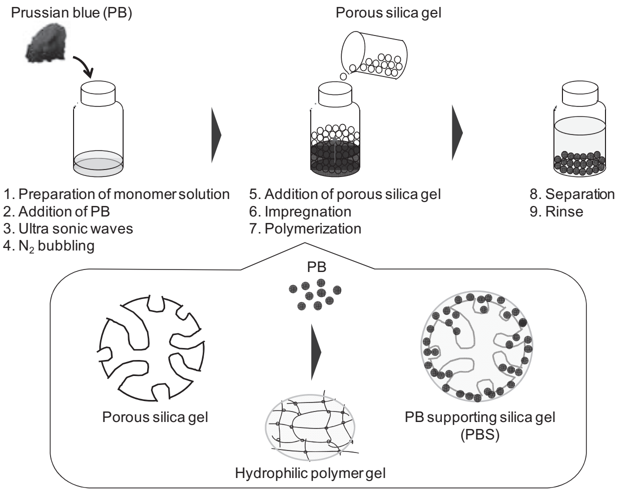

Fig. 1 Preparation procedure for PBS.

To evaluate the supporting strength for PB on PBS, two types of samples were compared. In the first type of sample, polymerization was conducted after the impregnation of the monomer solution into the porous silica gel, whereas in the second type of sample, polymerization was not conducted. Figure 2 shows photographs of each type of sample after shaking in water. In the case of PBS without polymerization (Figure 2(b)), the PB particles were released into water and remained suspended. However, in the case of PBS with polymerization (Figure 2(a)), the PBS settled quickly and the supernatant was transparent and did not contain released PB particles. In addition, in this type of sample, even after 3 h of shaking, the PB particles were strongly supported on the porous silica gel.

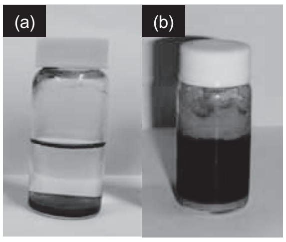

Fig. 2 PBS samples after shaking. (a) PBS with polymerization, (b) PBS without polymerization.

The amount of PB in various PBS samples was determined by X-ray fluorescence (XRF) analysis. The Fe concentrations in the PBS samples were measured using the calibration method. Table 1 shows the PB contents in PBS for different levels of PB addition during synthesis. The PB content in PBS increased with increase in the amount of PB. However, when a large amount (400 mg) of PB was added, the PB solution did not penetrate the porous silica gel, owing to high viscosity of the PB solution due to the high concentration of PB. In the cases of 50, 100 and 200 mg of PB addition, the shapes of each PBS observed by SEM were almost similar.

Table 1. PB contents in PBS samples produced under various conditions.

Amount of PB added (mg)	PB content in PBS samples (wt%)
50	2.65
100	3.33
200	4.61
400	N/A *

* The amount of PBS obtained was insignificant because the monomer solution containing PB did not penetrate the porous silica gels owing to high viscosity of the solution.

Secondly, batch test for the adsorption of Cs on to PBS (100 mg of PB was added) was conducted. The solid-liquid ratios were 2 mL/0.2 g-(wet PBS) and the adsorption time was 24 h. After the adsorption, the leak of PB from PBS was scarcely observed. The Cs concentration after adsorption was measured by atomic adsorption spectrometry (AAS). Batch tests examining the adsorption of Cs on to PBS produced under various conditions were conducted to clarify the adsorption ability of the various samples. For these experiments, the Cs concentration was 100 ppm, solid-liquid ratio was 2 mL/0.2 g-(wet PBS), and adsorption time was 24 h. Figure 3 shows the amount of Cs adsorbed on to the various PBS and PB supported on PBS sample. The amount of PB supported on PBS was calculated using XRF data.

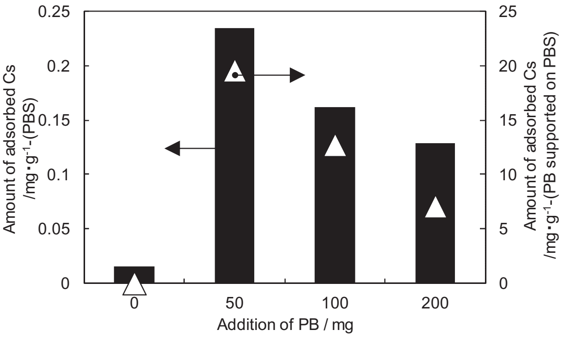

Fig. 3 Cs adsorption isotherms of PB supported on PBS.

Increase in the amount of PB added during synthesis resulted in a decrease in the amount of Cs adsorbed on to PBS and PB supported on PBS. As mentioned previously, the PB concentration of the monomer solution increased with increase in PB addition. Therefore, it is assumed that the PB particles are supported in the low dispersed state. This decrease in dispersibility caused decrease in the surface area of PB. Consequently, the Cs adsorption amount dropped. A large amount of PB particles needs to be incorporated within the porous silica gel for increasing the PB content and Cs adsorption of PBS because the PB particles are primarily supported on the outside of PBS.

Lastly, Cs column tests were conducted with PBS (100 mg of PB was added) as the column material. PBS (0.5 g; bed height 22 mm) and sea sand (bed height 78 mm) were poured into a glass column (inner diameter 5 mm, height 100 mm). The initial Cs concentration (concentration of the Cs solution before flowing in the column, C_0) was 403 ppb, flow rate was 2 mL/min, and space velocity (SV) was 278 h^{-1}. The Cs concentration (concentration of the Cs solution after flowing in the column, C) was measured by ICP-MS. Figure 4 shows the Cs breakthrough curve for PBS. The breakthrough curve sharply rises from a bed volume of about 60. From this result, it may be concluded that PBS exhibits a fast adsorption rate and is suitable for use as a column material in the continuous process. However, the value of C/C_0 did not reach 1 even after breakthrough, suggesting that Cs adsorption by the PB within PBS did not progress adequately owing to the high SV value.

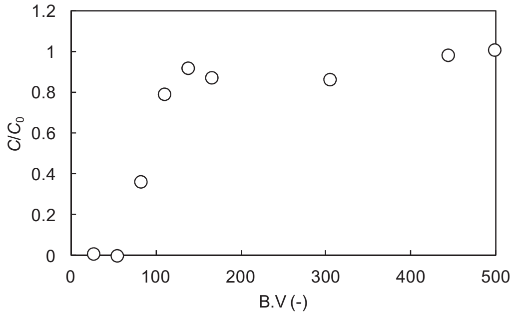

Fig. 4 Cs breakthrough curve for PBS as a column material.

In conclusion, we have succeeded in establishing a new granulation method for PB, which is difficult to handle owing to its small particle size. PB was supported on the surface of porous silica gel by a thin-film gel coating, which improves the supporting strength. Further, the PB content in PBS increased with increase in the amount of PB added during synthesis. Lastly, a breakthrough curve corresponding to shallow mass transfer was observed in the column tests using PBS. We confirmed that PBS is suitable for use as a column material for the adsorption of Cs in low concentrations. Furthermore, we expect that this new granulation method can be applied not only to PB, but also to other granular adsorbents.

Reference

1. Y. Inaba, Y. Sakai, K. Kanazawa, M. Harigai, H. Oaki, K. Takeshita, *Chem. Lett.* **45**, 776-778 (2016).

C. Global Nuclear Security Division

C.1 Effect of Microbial Cells on the Oxidation of Trivalent Cerium

Toshihiko Ohnuki, Mingyu Jiang, Fuminori Sakamoto, Naofumi Kozai, Shinya Yamasaki, Qianqian Yu, Kazuya Tanaka, Satoshi Utsunomiya, Xiaobin Xia, Ke Yang, Jianhua He

The anthropogenic rare earth elements (REEs) are potentially released into subsurface environments surrounding the storage and/or the disposal sites over geological time scale. Most REEs exhibit a trivalent oxidation state in the ambient environment. Manganese oxides are well known to accumulate large amounts of trivalent REEs. Manganese oxides sorb Ce(III) and oxidize it to Ce(IV) during the sorption process. On the other hand, the previous studies showed that a fraction of Ce(III) was not oxidized [1,2]. Further XANES analysis of biogenic Mn oxides [2] demonstrated the presence of Ce(III) oxidation and the sorption of Ce(IV) onto biogenic Mn oxides, results also indicated that the presence of microbial organic materials suppress the sorption of Ce onto Mn oxides. In the present study, Ce(III) uptake experiments on mixtures of synthetic MnO_2 and gram-negative bacterium, *Pseudomonas fluorescens*, were carried out to elucidate the influence of microorganisms on the sorption of Ce(III) by Mn oxides [3].

We used *Pseudomonas fluorescens* (ATCC 55241) isolated from the low-level radioactive waste disposal site in West Valley, NY, USA. For the sorption kinetics study, a mixture of $0.17\ g\cdot L^{-1}$ MnO_2 and $0.33\ g\cdot L^{-1}$ *P. fluorescens* cells was added to a Ce(III) solution of $10^{-4}\ mol\cdot L^{-1}$ at pH 3, 4, 6, or 8. The effect of Ce(III) pre-sorption by microbial cells on oxidation of Ce(III) to Ce(IV) by MnO_2 was tested. A microbial cell suspension was added to Ce solution and left to react, then followed by the addition of MnO_2 to the solutions for 96 h. After the sorption experiments, the Ce-sorbed mixtures and the Ce-sorbed microbial cells were collected using a hydrophilic PTFE filter (0.20 μm; Advantec, Tokyo) for Field Emission Scanning Electron Microscopy (FESEM) analysis. The separated mixtures on the filter were subsequently analyzed by FESEM (JEOL; JSM-7000F) at 5, 10, or 15 kV and by micro-X-ray fluorescence (micro-XRF) at synchrotron facilities. A Ce L_{III}-edge micro XANES spectra analysis was also performed to determine the oxidation states of Ce adsorbed to the Mn oxides and microbial cells in the mixtures. The filtrates were diluted in a $1.0x10^{-1}\ mol\cdot L^{-1}$ HNO_3 solution before analysis. Ce and P concentrations in the filtrates were determined by inductively coupled plasma atomic-emission spectrometry (ICP-AES; Shimadzu ICPS-7000 or ICP-OES; 720 Agilent Technologies, Inc., USA).

The distribution ratios (K_d) of Ce between the individual solids and solution increased with increasing pH of the solution, and was nearly the same in mixtures containing varying amounts of microbial cells. SEM-EDS and micro-XRF analyses showed that Ce was sorbed by both MnO_2 and microbial cells ($1.7x10^{-1}$ or $3.3x10^{-1}\ g\cdot L^{-1}$). In addition, nano-particles containing Ce and P developed on the surface of the microbial cells (Fig, 1). XANES analysis showed that lower fractions of Ce(III) were oxidized to Ce(IV) in the mixtures containing greater amounts of microbial cells. Micro-XANES analysis revealed that Ce was present as Ce(III) on the microbial cells and as Ce(IV) on Mn oxides (Fig. 2). These results strongly suggest that the association of Ce(III) with the microbial cell surface and the formation of Ce phosphate nano-particles are responsible for suppressing the oxidation of Ce(III) to Ce(IV) in the mixtures.

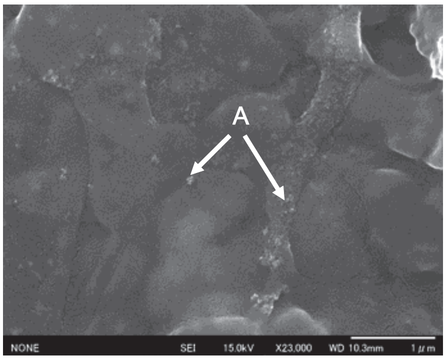

Fig. 1 SEM photograph spectra of the mixture containing MnO_2 and microbial cells after exposure to a $1x10^{-4}$ mol L^{-1} Ce solution for 4 h at pH 5.7. Arrow heads of A show nano particles.

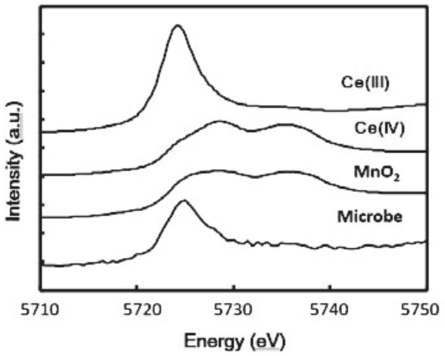

Fig. 2 Micro-XANES spectra of Ce L_{III}-edge from MnO_2 and microbes, along with the standard XANES spectra for Ce(III) and Ce(IV).

Reference

1. T. Ohnuki T., et al., Chem. Geology, 253, pp. 23-29. (2008)
2. K. Tanaka et al., Geochim. Cosmochim. Acta, 74, 5463-5477(2010).
3. 131T. Ohnuki, et al., Geochim. Cosmochim. Acta, 163, pp. 1-13 (2015).

C.2 Recovery behavior of high purity cubic SiC ceramics by post-irradiation annealing after low temperature neutron irradiation

Toyohiko Yano, Mohd Idzat Idris and Katsumi Yoshida

1. Introduction

Numerous reports on silicon carbide (SiC) show outstanding features in thermal and mechanical properties such as thermal stability at temperatures above 1273 K and excellent mechanical strength (>600 MPa). It had been used as an important material in tristructural-isotropic (TRISO) fuel of high temperature gas-cooled reactors. SiC exhibits tremendous stability in harsh radiation environment induced by fission products and neutrons in reactors. Nevertheless, the main flaw of monolithic SiC is its intrinsic brittle nature. To ensure enhanced reliability with increasing damage tolerance, the proposed materials for future structural components were SiC fiber-reinforced SiC composites (SiC_f/SiC). However, fusion reactor environment near the first wall is the considerably severe for materials due to wide energy range of ions, an extreme heat and electromagnetic flux, and a crucial dose of penetrating neutrons. In addition, the most significant threat to structural materials is fusion neutrons, which able to trigger the atomic displacement and the production of gaseous and solid transmutation products. These irradiation effects are liable for degradation of material performance of SiC and SiC_f/SiC. Thus, in order to understand the fundamental mechanical properties of SiC and SiC_f/SiC composites after neutron irradiation, the dimensional change, lattice parameter and microstructure of these materials should be measured and examined in specific.

In the previous work [1] seven of monolithic SiC or SiC_f/SiC composites specimens (PureBeta, Chemical vapour deposition (CVD)-SiC, Liquid phase sintering (LPS)-SiC, Nano-powder Infiltration and Transient Eutectoid (NITE) A and B, SiC_f/SiC of chemical vapor infiltration (CVI), NITE and electrophoretic deposition (EPD) methods) with different fabrication processes were irradiated in the BR2 reactor (Belgium) up to a fluence of 2.0-2.5×10^{24} (E>0.1 MeV) at 333-363K. Subsequently, changes in macroscopic length and lattice parameter were measured. In this report [2], recovery behavior assessment by post-irradiation annealing was conducted to clarify recovery stages of high purity monolithic β-SiC (PureBeta and CVD-SiC) polycrystals which were similar specimens as the previous study. Post-irradiated isochronal annealing up to 1673 K and *in-situ* length change measurement at 6 h isothermal annealing with increment of 50 K from room temperature was performed using a precision dilatometer to confirm recovery stages in high purity β-SiC.

2. Experimental procedures

2.1. Materials

High purity β-SiC polycrystals, PureBeta-SiC (Bridgestone, Japan) and CVD-SiC (Rohm and Haas Advanced Materials, USA), were used to appraise the recovery behavior by post-irradiation thermal annealing. Density of PureBeta was ~98% RD (3.14 g/cm^3) and contains carbon inclusions at grain boundaries. Total metallic impurity amount is less than 0.3 ppm. CVD-SiC is a single-phase cubic and has a high purity up to 99.9995% of SiC with a mostly full density and has no voids or microcracks. Both of these materials were machined into 25 x 4 x 2 mm^3 in bar shape.

2.2. Neutron irradiation and post-irradiation annealing

Specimens were concurrently neutron-irradiated in the BR2 reactorup to a fluence of 2.0~2.5×10^{24} n/m^2 (E>0.1 MeV, 0.20~0.25 dpa) at 333-363 K. Prior to post-irradiation annealing, both unirradiated and irradiated specimens were cut into half (25 x 2 x 2 mm^3). The annealing behavior was investigated by a precision dilatometer. Length change for both specimens were measured *in-situ* continuously from room temperature up to 1673 K with a step heating temperature interval of 50 K in helium atmosphere, as described previously in the literature [3]. After completing the annealing, macroscopic lengths and lattice parameter of both irradiated specimens were determined by a point type micrometer and XRD technique at room temperature (RT) [1].

2.3. Rate of recombination and activation energy

Presence of point defects is correspond to the volume change (ΔV) of the specimen after neutron irradiation, and the recovery of crystal after thermal annealing is based on migration of these defects and annihilation. Thus, by understanding the material behavior and dynamic process of defects recombination, important quantities of activation energy for recombining interstitials and vacancies from Frenkel pairs which are formed in irradiated samples are able to be estimated by first order reaction (1) and an Arrhenius equation (2) as follow.

$$\ln [A] - \ln [A_0] = - kt \qquad (1)$$

$$\ln k = -E_a/k_BT + \ln A \qquad (2)$$

where A_0 and A are volume of unirradiated and after annealing of irradiated specimen, k is a rate coefficient, k_B, E_a and T are Boltzman constant, activation energy and absolute temperature, respectively.

3. Results and discussion

3.1 Recovery behavior by isochronal annealing

Recovery behaviors due to isochronal annealing for 6 h from RT up to 1673 K of PureBeta-SiC and CVD-SiC are shown in Fig. 1. From the figure, we can noticed that recovery behavior for both specimens were mostly identical, and were started at 333-363 K which was similar with irradiation temperature, and the recombination rate was relatively high until ~573 K. After that, the

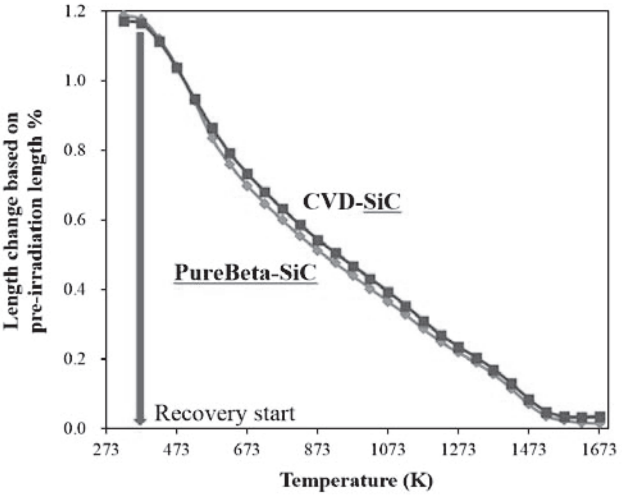

Fig. 1. Recovery behavior by isochronal annealing from room temperature up to 1673 K for PureBeta-SiC and CVD-SiC.

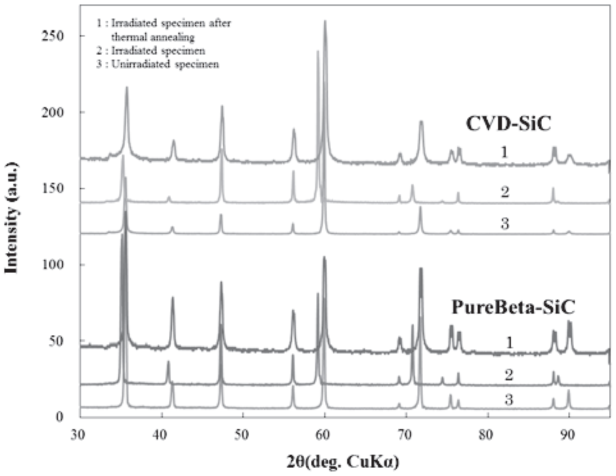

Fig. 2. XRD profile peaks measured at room temperature after post-irradiation annealing up to 1673 K for PureBeta-SiC and CVD-SiC.

recombination rate was seemed to become lower followed by saturation of recovery at elevated temperature (~1573 K). We assumed that mechanism of defects annihilation should be mainly occurred by recombination of vacancies and interstitial atoms. One of the author in this research also reported that, in spite of the β-SiC were neutron-irradiated at higher fluence up to 2.8 × 10^{26} n/m^2 at 753 K and 4.6 × 10^{26} n/m^2 at 1003 K, the macroscopic length changes decreased gradually near irradiation temperature which were at ~773 K and at ~873 K, respectively, and almost constant at elevated temperature where the lengths returned completely to the pre-irradiation lengths [4]. The same recovery tendencies also observed upon medium fluence up to 5.3 × 10^{24} n/m^2 (E>0.1 MeV) at 743 K for α- and β-SiC and less fluence irradiated α-SiC where it exposed to 1.9 × 10^{23} n/m^2 (E>0.1 MeV) at <473 K [3].

By performing the XRD to determine the lattice parameter at RT, the diffraction profiles of peaks with indices (111), (200), (220), (311), (222) and (400) of β-SiC for each specimen were scrutinized as shown at Fig. 2. As explained in a previous research [1], peaks of irradiated specimens were shifted to a smaller angle due to swelling by formation of point defects, however the peaks were returned to the same positions of those of the unirradiated specimens after the post-irradiation annealing. Table 1 summarizes the recovery behavior by measuring the macroscopic length and lattice parameter change of PureBeta-SiC and CVD-SiC. From the table, it was shown apparently that both specimens were recovered well after annealing at 1673 K. Comparing recovery rate after isochronal annealing for 6 h between cubic (β) polytype of SiC in present work (Fig. 1) and that of hexagonal (α) polytype (6H) containing small amount (0.3%) of boron as sintering additive in the previous works (Fig. 4 in ref. 5, Fig. 4 in ref. 3), it is obvious that recovery percentage at lower annealing temperature than ~873 K, particularly less than 573 K of β-polytype is significant (quick recovery).

3.2 Recovery behavior by isothermal annealing

When the recovery process was governed by the recombination of interstitial atoms with vacancies, this annihilation process of defects could be explained as a first order reaction [3]. The macroscopic volume recovery behavior of PureBeta-SiC during each isothermal annealing was plotted against annealing time (not shwn here). We tried to fit the line in logarithmic scale into single straight slope but the coefficient of determination R^2 was not very well, therefore it was divided and fitted into two straight lines along isothermal annealing time which defined as former and latter part. Each R^2 for fitting was mostly better than 0.95 in both former and latter part. It is well known that there are several kinds of point defects in SiC crystalline lattice, and there is a probability that some of these recombination rates are overlapped or consecutively occur at wide temperature range. Hence, by obtaining the rate coefficient of the first order reaction, it is explicitly fit to measure the activation energy [6].

Fig. 3 shows an Arrhenius's plots using the rate coefficient. From this figure, the activation energies, E_a of the volume recovery can be determine. The rate coefficients of PureBeta-SiC were divided into 4 stages to acquire the differences of activation energies and to understand the defects annihilation mechanism. We perceived that the straight line is slightly steeper at the first stage where the recovery behavior begins, similar to irradiation temperature up to 573 K. Nevertheless, as the temperature entered the stage 2 (723-923 K), the straight lines are almost flat followed by a little steeper straight lines in stage 3 (923-1173 K), and the slopes tend to more incline at the elevated temperature from 1323 to 1523 K, where the recovery behavior almost saturated, as shown in Fig. 1. Between 1173 K and 1273 or 1323 K, these k values are almost constant, indicating the change in recovery mechanism. Similar with PureBeta-SiC, the rate coefficient can be divided into 4 stages to obtain the activation

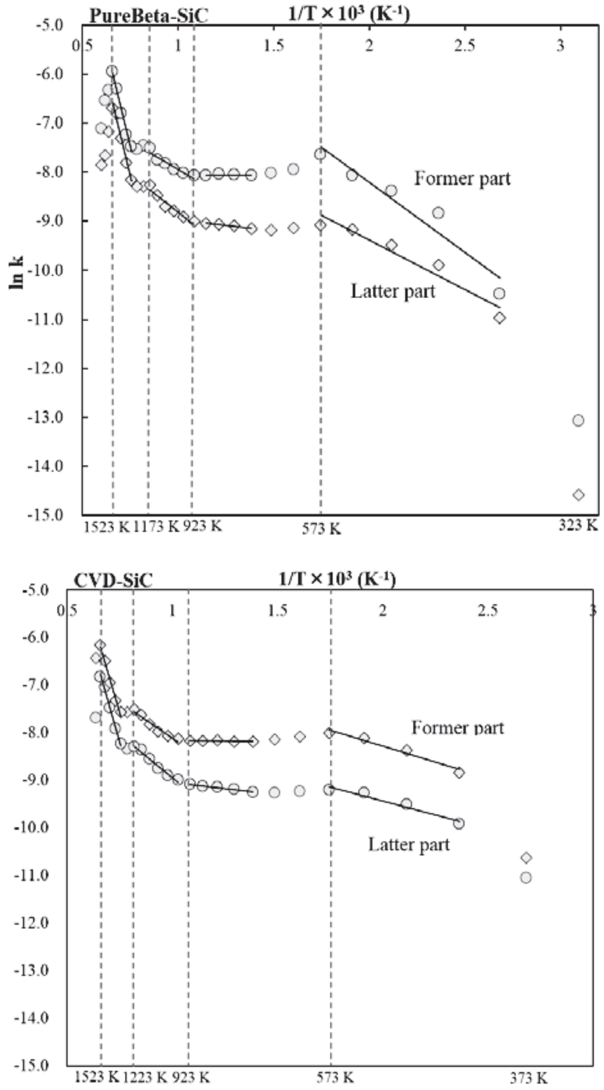

Fig. 3. The Arrhenius plot of volume recovery of PureBeta-SiC and CVD-SiC according to the rate coefficient, *k* value which obtained by first order reaction. Activation energies can be measured using the slope of the straight lines.

energies. At lower temperature (423-573 K), the straight line is steeper as the recovery behavior started at this stage but it shows nearly flat as the temperature entered the stage 2 (723-923 K). However, the straight line becomes steeper at stage 3 (973-1223 K). The fourth stage (1223-1523 K) was almost same as the case of PureBeta, the constant *k* region followed by steepest line for both former and latter. From comparison of two figures in Fig. 3, changes in recovery rate *k* against annealing temperature of PureBeta and CVD-SiC were very similar each other.

The inclination of the straight lines can be express by the activation energies, obtained using Arrhenius equation (2). The activation energies at 373-573 K for PureBeta-SiC and CVD-SiC were in the range of 0.17-0.24 eV and 0.10-0.12 eV, respectively as they were divided by former and latter parts. However the activation energies become lower in the range of 0.002-0.04 eV and 0.006-0.04 eV for PureBeta-SiC and CVD-SiC at 723-923 K, and it increase gradually to 0.20-0.27 eV and 0.26-0.31 eV at 923-1223 K followed by 1.37-1.38 eV and 1.26-1.29 eV at 1323-1523 K, respectively. Yano et al. [6] reported that similar results emerged for PureBeta-SiC which the activation energies were 0.11, 0.07, 0.37, and 1.23 eV at 423-573 K, 723-1023 K, 1023-1173, and 1273-1573 K, respectively. However, the activation energies for SiC containing secondary elements were slightly difference from the high purity SiC. According to Suzuki et al. [7,8], the swelling and the recovery behavior for the simultaneously irradiated polycrystalline SiC were different depending by presence of sintering aids and/or polytypes of SiC. For instance, Yamazaki et al. [9] reported that the activation energies for SiC which contained Al_2O_3 were 0.2 and 0.9 eV at 823-1223 K and 1223-1523 K, respectively, while SiC which contained B_4C were 0.12 and 0.79 eV at 473-1073 K and 1073-1223 K, respectively. Another report also showed that the activation energies for α-SiC sintered bodies consisting of mainly 6H polytype were 0.14, 0.26, and 1.13 at 473-873 K, 923-1223 K, and 1373-1573 K, respectively [5]. Nonetheless, by comparing the activation energies of 3C-SiC and 6H-SiC, Yano et al. [6] concluded that those were mostly similar and no significant difference was found for different polytypes and/or sintering impurities in that neutron irradiation and annealing conditions. In addition, although SiC containing B_4C, mainly 6H polytype and SiC containing Al_2O_3, mainly 4H- and 6H-polytype have different atomic configurations in cubic stacking part and hexagonal part, but the basic recovery behavior was similar due to small difference in stacking sequence [9]. However, there is a slight difference in the first and second stages' recovery (<873 K) for high-purity β-SiC and α-SiC. High purity β-SiC recovered more quickly in this temperature range (lower E_a).

Weber and Gao et al. [10,11] reported that annihilation of Frenkel defects in β-SiC by computational methods based on molecular dynamics, and showed that 60% of the interstitials produced were able to recombine with vacancies at RT. They also asserted that the activation energies for close-pair recombination of C Frenkel pairs were between 0.24 and 1.6 eV while recombination of Si Frenkel pairs was in the range of 0.28 and 0.90 eV. Moreover, migration energies of C and Si interstitial atoms in β-SiC were 0.74 and 1.53 eV, respectively whereas migration energies for C and Si vacancies were 4.10 and 2.35 eV, respectively [12]. In this study, the first and the third stages of activation energies for both specimens were closed to the computational data which was 0.24 eV for recombination of C Frenkel pairs, where the C interstitials were separated by $0.47a_o$ (a_o is the lattice parameter of cubic β-SiC) from the vacancies. In addition, since the Si^+–C <100> dumbbell close to the Si vacancy with a separation distance of only $0.57a_o$, it is expected that the interstitial should simply recombine with the vacancy by 0.20 eV [13] and 0.28 eV [11], for recombination of Si Frenkel pairs. As a result, we can conclude that the

Table 1. Comparison of swelling of macroscopic length change and lattice parameter measurement before and after thermal annealing up to 1673 K at room temperature.

Specimen	Fluence (n/m^2)	Irradiation temperature (^oC)	Before thermal annealing		After thermal Annealing (1673 K)	
			Microscopic length change (%)	Lattice parameter (%)	Microscopic length change (%)	Lattice parameter (%)
PureBeta-SiC	$2.0\text{-}2.5\times10^{24}$	60-90	1.19	1.13	0.03	0.01
CVD-SiC			1.17	1.17	0.02	-0.02

recombination less than ~1223 K possibly occurred for intimately positioned C and Si Frenkel pairs which are less than separated distance of $0.57a_o$ and no long range migration is essential. It is noted that nearly three fourths of volume recovery was proceeded by the recombination of closely positioned Frenkel pairs, see Fig. 1. The highest activation energy at the stage 4 for PureBeta-SiC was 1.38 eV which is close to 1.34 eV ($1.05a_o$) [11] and 1.40 eV [13], for recombination of C Frenkel pairs which is higher than the migration energy of a C^+–C <100> interstitial [14], or migration of Si interstitials (1.40 eV [13], 1.53 eV [12]) where they jump straightly from one tetrahedral orientation to a similar position by a kick-in/out process through a Si-Si split-interstitial configuration. Besides that, the highest activation energy for CVD-SiC at the stage 4 was 1.29 eV which is close to the same recombination energy of PureBeta-SiC for C Frenkel pairs, or migration of Si interstitials. Hence, recombination of slightly separated C Frenkel pairs and more long-range migration of Si interstitials may have occurred for both PureBeta-SiC and CVD-SiC specimens at 1323-1523 K. Activation energies corresponding to the migration of C or Si vacancy were not found in both specimens up to annealing temperature of 1523 K. Therefore, independent vacancies of carbon and silicon should not migrate, just as sinks for corresponding interstitials until 1523 K. It was supported by Price's report [15] which clarified that the lowest temperature for void formation under neutron irradiation was 1523 K. It is still unclear, between 573-923 K and 1173(1223)-1323 K, why are the recovery rates almost constant independent of temperature ($E_a\approx0$), however these phenomena are observed commonly in SiC [5,6].

4. Conclusion

High purity PureBeta-SiC and CVD-SiC were concurrently neutron-irradiated in the BR2 reactor up to a fluence of $2.0\text{~}2.5\times10^{24}$ (E>0.1 MeV) at 333-363 K. Obtained results are summarizes as follows:

1. Recovery of defects induced by neutron irradiation in high purity β-SiC have four stages with different activation energies. At 373-573 K, the activation energy of PureBeta-SiC and CVD-SiC were in the range of 0.17-0.24 eV and 0.12-0.14 eV, 0.002-0.04 eV and 0.006-0.04 eV at 723-923 K, 0.20-0.27 eV and 0.26-0.31 eV at 923-1223 K, and 1.37-1.38 eV and 1.26-1.29 eV at 1323-1523 K, respectively.
2. Below ~1223 K the recombination possibly occurred for closely positioned C and Si Frenkel pairs and no long range migration is essential. Nearly three fourths of recovery induced by neutron irradiation occur by this mechanism. In addition, at 1323-1523 K, recombination of slightly separated C Frenkel pairs and more long-range migration of Si interstitials may have occurred for PureBeta-SiC and CVD-SiC specimen. Migration of both vacancies may be restricted up to ~1523 K.
3. Comparing to hexagonal α-SiC, high purity β-SiC recovered more quickly in the lower annealing temperature range less than 873 K, particularly less than 573 K.

Reference

1. M. I. Idris, H. Konishi, M. Imai, K. Yoshida and T. Yano, Energy Procedia, Vol.71, pp.328-336 (2015).
2. M. I. Idris, S. Yamazaki, K. Yoshida and T. Yano ; J. Nucl. Mater., Vol.465, pp. 814-819 (2015).
3. S. Yamazaki, M. Imai, T. Yano, Prog. Nucl. Energy. Vol.50 pp.601-605 (2008).
4. T. Yano, M. Akiyoshi, K. Ichikawa, Y. Tachi and T. Iseki, J. Nucl. Mater., Vol.289, pp.102-109 (2001).
5. T. Yano, Y. Futamura, S. Yamazaki, T. Sawabe and K. Yoshida, J. Nucl. Mater., Vol.442, pp.S399-S403 (2013).
6. T. Yano, Y. You, K. Kanazawa, T. Kobayashi, M. Imai, K. Yoshida and S. Yamazaki, J. Nucl. Mater., Vol.455, pp.445-449 (2014).
7. T. Suzuki, T. Yano, T. Maruyama, T. Iseki. and T. Mori, J. Nucl. Mater., Vol.165, pp.247-251 (1989) .
8. T. Suzuki, T. Iseki. T. Mori and J.H. Evans, J. Nucl. Mater., Vol.170, pp.113-116 (1990).
9. S. Yamazaki, K. Yoshida and T. Yano, J. Nucl. Mater., Vol.417, pp.425-429 (2011).
10. W.J. Weber, F. Gao, R. Devanathan, W. Jiang and C.M. Wang, Nucl. Instrum. Methods Phys. Res., B, Vol.216, pp.25-35 (2004).
11. F. Gao and W.J. Weber, J. Appl. Phys., Vol.94, pp.4348-4356 (2003).
12. F. Gao, W.J. Weber, M. Posselt and V. Belko, Phys. Rev. B, Vol.69 (2004) 245205.
13. M. Bockstedte, A. Mattausch and O. Pankratov, Phys. Rev. B, Vol.69 (2004) 235202.
14. F. Gao, G. Henkelman, W.J. Weber, L.R. Corrales and H. Jonsson, Nucl. Instrum. Methods Phys. Res. B, Vol.202, pp.1-7 (2003).
15. R. J. Price, J. Nucl. Mater., Vol.48, pp.47-57 (1973).

C.3 Microstructure of Porous SiC Ceramics Based on In–Situ Grain Growth

Katsumi Yoshida, Toyohiko Yano

1. Introduction

Silicon carbide (SiC) is one of the attractive materials for structural applications such as aerospace industries, nuclear applications and high-temperature gas turbine since it shows high thermal and chemical stability, high stiffness, high hardness, high thermal conductivity, excellent oxidation, corrosion and wear resistance, high mechanical strength at high-temperatures, low thermal expansion, and good resistance to high-energy neutron irradiation. Recently, porous ceramics have received great attention in many fields. Porous ceramics have been traditionally used as heat insulating materials and refractories. Furthermore, porous ceramics have been expected to be applied as catalyst carrier, diesel particulate filter (DPF), membranes for gas separation, filters for water purification, adsorbent, electrodes for batteries, and bone-graft substitutes and so on. Currently, porous SiC ceramics has been commercially used for DPF.

Pore size control and surface functionalization of porous ceramics have been strongly required to extend their applications. Present authors have proposed the surface functionalization of porous ceramics based on in-situ grain growth. Figure 1 shows the concept of the porous ceramics with in-situ grain growth. The authors paid attention to the interesting structures seen in nature such as calcareous caves for the surface functionalization of porous ceramics. In our study, in-situ grain growth has been defined as the grain growth and the grain orientation on the sintered surface such as the surface and/or inside of pore walls and frameworks in porous ceramics, and we have tried to fabricate porous ceramics based on in-situ grain growth. In our previous study, porous SiC ceramics with in-situ plate-like grain growth were successfully achieved by pressureless-sintering at 2150^{o}C for 30 min using submicron-sized b-SiC powder and 0.1 wt% aluminum (Al) - 0.15 wt% boron (B) - 1.00 wt% carbon (C) additives [1,2]. In addition, aluminum nitrate enneahydrate ($Al(NO_3)_3•9H_2O$) was effective to enhance plate-like grain growth in porous SiC ceramics because Al from $Al(NO_3)_3•9H_2O$ would be distributed homogeneously on the SiC powder rather than metallic Al powder. The pore size distribution of the porous SiC ceramics with in-situ grain growth was bimodal, and larger pores (around 8 μm) and smaller pores (around 1 μm) would be formed by pore formers and the gaps among plate-like grains, respectively.

In this study, three kinds of β-SiC powders with different particle sizes were used as the starting materials, and the effects of β-SiC particle size and sintering temperature on microstructure of porous SiC ceramics based on in-situ grain growth were investigated.

2. Experimental

Submicron-sized (average particle size; 0.3 μm), micron-sized (2.3 μm) or coarse β-SiC powder (5.3 μm) was used as the starting materials. In this study, Al-B-C system was selected as the sintering additives and grain growth promotors. Al-B-C system has been known as the sintering additives for SiC. The compositions of B and C were 0.15 wt% and 1.00 wt%, respectively. Aluminum nitrate enneahydrate ($Al(NO_3)_3•9H_2O$) was used as the Al source, and the composition of Al was adjusted to 0.1 wt%. Beta-SiC powder and sintering additives were mixed by wet ball-milling for 24 h using SiC balls, and then dried with a rotary evaporator. The dried powder was crushed with SiC mortar and pestle, followed by sieving with mesh with opening of 300 μm. Spherical polymethyl methacrylate (PMMA) particles were used as pore formers to fabricate porous SiC ceramics. PMMA particles were added to the starting powders. The amount of PMMA particles was 17 wt% (40 vol%). The powder was mixed with SiC mortar and pestle. After mixing, the powder was sieved through mesh with opening of 300 μm. The powder was formed into a cylindrical compact by uniaxial pressing at 17 MPa, followed by heat-treatment at 400^{o}C for 1h in air at a heating rate of 1^{o}C/min in order to remove the PMMA particles in the compacts. The compacts were pressureless-sintered at 1850-2150^{o}C for 30 min in argon atmosphere at a heating rate of 30^{o}C/min. The compacts were heated under vacuum from room temperature to 1500^{o}C. After being held at 1500^{o}C under vacuum for 30 min, argon gas was fed into the furnace, and the compacts were heated to the desired temperature in argon flow. Bulk density and open porosity of the porous SiC ceramics were measured by Archimedes' method. Their microstructure was observed with a field emission scanning electron

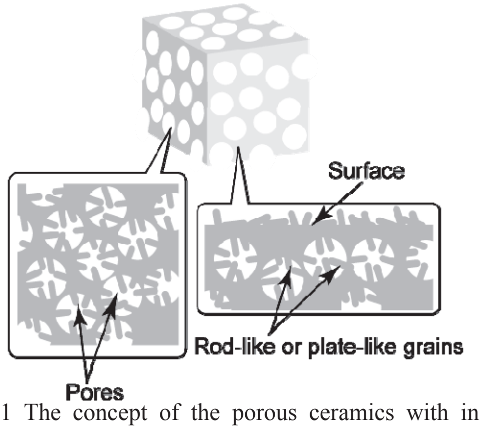

Fig. 1 The concept of the porous ceramics with in-situ grain growth.

microscope (FE-SEM). Crystalline phases of the porous SiC ceramics were identified by a powder X-ray diffraction analysis and the distribution of SiC polytypes in the porous SiC ceramics was determined by Ruska's method.

3. Results

3.1 Porous SiC Ceramics using Submicron-Sized β-SiC Powder (0.3 μm)

Figure 2 shows SEM micrographs of the porous SiC ceramics using submicron-sized β-SiC powder sintered at 1850°C-2150°C. At 1850°C and 1950°C, grain growth did not occur during sintering, and plate-like SiC grains were not observed. At 2050°C, grain growth was promoted and the formation of plate-like grains started. At 2150°C, the porous SiC ceramics consisted of plate-like SiC grains of around 10-20 μm, and the plate-like SiC grains stuck out of the walls of pores and the sintered surface in the porous SiC ceramics. Bulk density and open porosity of the porous SiC ceramics sintered at 2150°C were 1.43 g/cm^3 and 52.0 %, respectively. Their volume shrinkage after sintering at 2150°C was around 5 %.

The porous SiC ceramics sintered at 1850°C and 1950°C mainly consisted of 3C (β-SiC), and the fraction of 3C in the porous SiC ceramics was around 90 %. The fraction of 3C decreased and the formation of 6H (α-SiC) was enhanced with increasing sintering temperature, and the fraction of 6H in the porous SiC ceramics sintered at 2150°C was 76 %. In addition, the fraction of 4H (α-SiC) also increased from 1 % to 8 %. From this result, it is suggested that the plate-like SiC grains formed in the porous SiC ceramics during sintering mainly corresponded to 6H phase.

3.2 Porous SiC Ceramics using Micron-Sized β-SiC Powder (2.3 μm)

Figure 3 exhibits SEM micrographs of the porous SiC ceramics using micron-sized β-SiC powder sintered at 2000°C and 2150°C. Whereas SiC grains were not grown in porous SiC ceramics sintered at 2000°C, large SiC grains were observed in porous SiC ceramics sintered at 2150°C. Large plate-like SiC grains of about 30-40 μm in maximum grew during sintering and the porous SiC ceramics consisted of entangled large plate-like SiC grains. In addition, the number and the size of gaps among plate-like grains also increased with increasing the particle size of the starting β-SiC powder. Bulk density of the porous SiC ceramics sintered at 2150°C was 1.13 g/cm^3 and their open porosity was 65.7 %. The volume shrinkage of the porous SiC ceramics sintered at 2150°C was about 6 %. The porous SiC ceramics using the micron-sized β-SiC powder showed higher open porosity than the porous SiC ceramics using the submicron-sized β-SiC powder due to the increase in the number and the size of gaps among plate-like grains and the pore size formed by pore formers.

At 2000°C, 3C phase predominantly existed in the porous SiC ceramics, and its fraction was around 90 %. In the case of the porous SiC ceramics sintered at 2150°C, 6H was major phase in porous SiC ceramics, and its fraction was around 80 %. This value was slightly higher than the porous SiC ceramics using the submicron-sized β-SiC powder. Furthermore, the fractions of 4H also increased from 2 % to 15% as sintering temperature increased. The results suggested that the porous SiC ceramics mainly consisted of 6H and 4H phases.

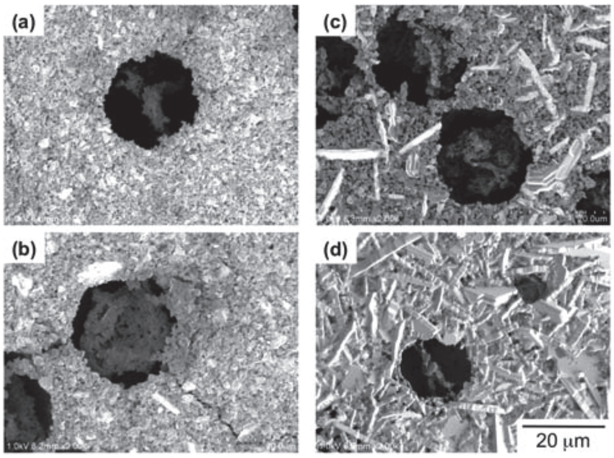

Fig. 2 SEM micrographs of the porous SiC ceramics using submicron-sized β-SiC powder (0.3 μm) sintered at (a) 1850°C, (b) 1950°C, (c) 2050°C and (d) 2150°C.

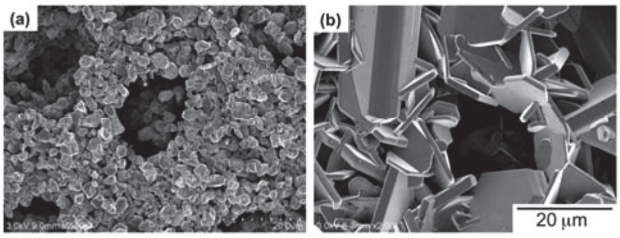

Fig. 3 SEM micrographs of the porous SiC ceramics using micron-sized β-SiC powder (2.3 μm) sintered at (a) 2000°C and (b) 2150°C.

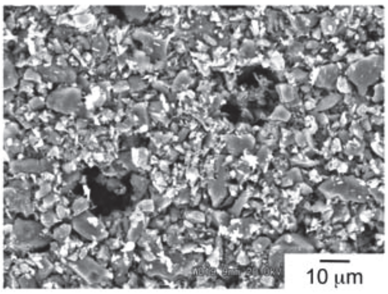

Fig. 4 SEM micrograph of the porous SiC ceramics using coarse β-SiC powder (5.9 μm) sintered at 2150°C.

3.3 Porous SiC Ceramics using Coarse β-SiC Powder (5.9 μm)

SEM micrograph of the SiC porous ceramics using coarse β-SiC powder sintered at 2150°C is exhibited in Fig. 4. The porous SiC ceramics had a bulk density of 1.31 g/cm^3 and an open porosity of 57.8 %. The volume shrinkage of the porous SiC ceramics was around 5 %.

Despite sintering at 2150°C SiC grains did not grow and plate-like SiC grains were not observed in the porous SiC ceramics using the coarse β-SiC powder. It seemed that sintering of the porous SiC ceramics did not proceed well, and there were many gaps among each SiC garins in the porous SiC ceramics.

At 2150°C, 3C phase was still dominant in the SiC porous ceramics, and the fraction of 3C was 75 %.

4. Discussion

In order to discuss the effect of Al-B-C addition to SiC on β-α phase transformation of SiC and microstructure of porous SiC ceramics, porous SiC ceramics without Al-B-C additives were fabricated at 2150°C, and their microstructure and fractions of SiC polytypes in the porous SiC ceramics were evaluated. In the case of submicron-sized β-SiC powder, only a few SiC grains were grown into plate-like shape. As for the porous SiC ceramics using micron-sized and coarse β-SiC powders, plate-like SiC grains were not grown without additives.

The fraction of 3C phase in the porous SiC ceramics without Al-B-C additives was over 70%, and this means that β-α phase transformation and plate-like grain growth were well promoted at 2150°C with Al-B-C addition. On the other hand, β-α phase transformation did not take place in the porous SiC ceramics using the coarse β-SiC powder, and the coarse β-SiC particles did not grow into plate-like shapes at 2150°C in spite of Al-B-C addition. It was reported that the rate of β-α phase transformation of SiC powder was proportional to the dimension of the specific surface area of the powder. The present result suggested that the size of plate-like SiC grains grown in the porous SiC ceramics depended on the starting β-SiC particle size. However, the coarse β-SiC particles did not transform into α-phase easily and did not grow into the plate-like shape under the present sintering condition, and this result was consistent with their report.

Furthermore, impurities in the starting SiC powders may affect the grain growth in the porous SiC ceramics because the amount of the additives was very small. Submicron-sized and coarse β-SiC powders contain traces of iron, aluminum, and calcium as impurities, and micron-sized β-SiC powder does not contain the metallic impurities because the β-SiC powder was synthesized via liquid phase route. As mentioned above, only a few SiC grains were grown into plate-like shape in the porous SiC using submicron-sized β-SiC powder without Al-B-C additives. At present, it has been unclear whether this grain growth occurred by the effect of β-SiC particle size or impurities. In our future works, the effect of impurities in the starting SiC powders, notably the submicron-sized β-SiC powder, on the grain growth in the porous SiC ceramics should be considered to clarify the in-situ growth mechanism in our porous SiC ceramics.

From the results, it is concluded that the porous SiC ceramics with a unique morphology of entangled large plate-like SiC grains were achieved using the micron-sized β-SiC powder with small amount of Al and B additions at 2150°C, and the plate-like SiC grains formed in the porous SiC ceramics during sintering mainly corresponded to 6H.

5. Conclusion

Porous silicon carbide (SiC) ceramics were fabricated based on in-situ grain growth, and the effects of β-SiC particle size and sintering temperature on the microstructure of the porous SiC ceramics were investigated. Submicron-sized (average particle size; 0.3 μm), micron-sized (2.3 μm) or coarse β-SiC powder (5.3 μm) was uses as the starting material, and aluminum (Al), boron (B) and carbon (C) were added to SiC powder as sintering additives and grain growth promotors.

In the case of the submicron-sized β-SiC particles, grain growth was promoted and plate-like grains started to form at 2050°C, and the porous SiC ceramics consisted of plate-like SiC grains of around 10-20 μm at 2150°C. Whereas SiC grains were not grown in porous SiC ceramics using the micron-sized β-SiC particles sintered at 2000°C, large SiC grains were observed sintered at 2150°C. The porous SiC ceramics with a unique morphology of entangled large plate-like SiC grains of about 30-40 μm in maximum were achieved using the micron-sized β-SiC powder. XRD analysis suggested that the formation of 6H phase was promoted in the porous SiC ceramics using the submicron-sized or the micron-sized β-SiC powder with small amount of Al and B additions at 2150°C, i.e. the small amount of Al and B additions would promote the formation of 6H phase in the porous SiC ceramics at 2150°C. In addition, the plate-like SiC grains mainly corresponded to 6H phase. On the other hand, β-α phase transformation did not take place in the porous SiC ceramics using coarse β-SiC powder, and the coarse β-SiC particles did not grow into plate-like shapes at 2150°C in spite of Al-B-C addition.

Acknowledgement

This work was partially supported by Grant-in-Aid for Young Scientists (B) (21750204) from The Ministry of Education, Culture, Sports, Science and Technology (MEXT).

References

1. K. Yoshida, *Chemical Industry (Kagaku Kogyo)*, **62**, 672-676 (2011) [in Japanese].
2. K. Yoshida, *Ceramic Data Book 2011/12*, 84-88 (2011) [in Japanese].

C.4 Effect of heterogeneous moderator in the fast breeder reactor blanket as a target of plutonium denaturing and TRU transmutation

Hiroshi SAGARA

1. Introduction

A comparative study was performed with different designs of the fast breeder reactor (FBR) blanket to evaluate the performance of plutonium breeding accompanied with denaturing, and transuranium (TRU) transmutation for enhancement of the proliferation resistance and actinide management in the future fuel cycle. Four designs of the FBR blanket fuel were intercompared, conventional depleted uranium (DU) oxide fuels, DU with TRU oxide fuels, DU with TRU oxide fuels with homogeneous/heterogeneous moderators.

2. Methodology

Four designs of FBR blanket fuel will be studied and compared each other; 1) conventional depleted uranium (DU) oxide fuel, 2) DU with TRU oxide fuel, 3) DU with TRU and homogeneous moderator mixture, and 4) DU with TRU and heterogeneous moderator rod/pellet arrangement. Secondly, the number and the loading pattern of moderator rods/pellets were compared inside the radial blanket assembly and also inside the axial blanket, and were optimized by maximizing TRU transmutation ratio to the even-mass-number plutonium isotopes, where the fuel breeding performance of the reference core were preserved. Finally, the non-proliferation aspect were evaluated of the blanket spent fuel by the material attractiveness. **Fig. 1** shows the three-dimensional calculation model applied in the present study, and parametric survey of the geometry was performed in the axial and the radial blanket fuels independently for the better statistics of three-dimensional calculation.

3. Results

As results, with heterogeneous moderator in the axial and the radial blanket fuels, the greatest TRU transmutation and plutonium denaturing performance were attained without deteriorating fuel breeding. Design optimization was performed as for ZrH1.65 moderator rod/pellet arrangement in the axial and the radial blanket fuel assemblies. The optimum number of moderator rods per assembly was 25 (11% of the number of total rods) with proper interval (2-3cm) and symmetrical arrangement in the radial blanket, and insertion of 1cm thick ZrH1.65 moderator pellets to 4 and 10 cm from the top and the bottom planes of the active core was the optimum design in the axial blanket, in order to achieve the highest TRU transmutation ratio and plutonium denaturing performance without deteriorating fuel breeding. From the non-proliferation aspect, material attractiveness of plutonium were evaluated comparing with the criterion based on decay heat, and required TRU doping ratio in DU with TRU oxide fuel were proved to be as 1.6-2.5wt.% with heterogeneous moderator, 2.1-3.0wt.% with homogeneous moderator, and 4.1-5.0wt.% without moderator. The heterogeneous loading of moderation showed the great advantages of fuel treatment in order to clear the heat generation limit criterion, as well as mass requirement to the initial and multi-cycle phases.

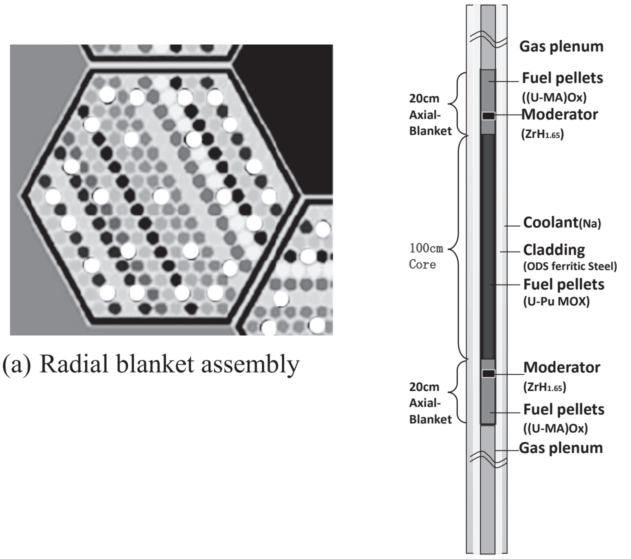

(a) Radial blanket assembly

(b)Vertical single fuel rod cell

Fig. 1 Calculation model of Fast Reactor Blankets

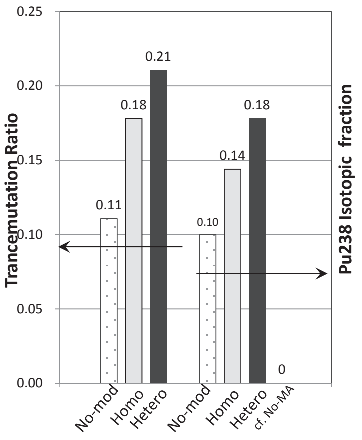

Fig. 2 Transmutation ratio, isotopic ratio of ^{238}Pu at EOC in radial blanket

References

1. H. Sagara, K. Matsumoto, I. Yamauchi, K. Nakao, C. Y. Han, T. Onishi, S. Koyama and M. Saito, Prog. Nucl. Energy, Vol. 82, P. 92–97, July (2015).

C.5 Sociological Aspect of the Origin and Structure of the "Genshiryoku-mura (Nuclear Village or Pro-Nuclear Concession Sector)"

Tetsuo Sawada

1. Introduction

The Fukushima Daiichi nuclear disaster caused serious disorders in the Post 3.11 society especially in Japan. The origin of the disorders is so-called "information contamination" or information pollution.

Information contamination: it is also denoted as information pollution that was first discussed by L. Orman.[1] Information contamination means the contamination of information supply with irrelevant, redundant, unsolicited and low-value information.

In the post-3.11 Fukushima Daiichi nuclear accident era, information contamination was successively created by unintentional cooperation between the experts' explanations concerning the accident progression/radiation effect and the newspaper, TV, and magazine reports on them. Sometimes they can be biased. Such mass-media reports can be intentionally edited for the Internet information. In the Web, such contaminated information has been rapidly reproduced so that much of the public can build up their own understanding based on the biased and irrelevant information. Typical contaminated information is the discourses such as 1) we must be never irradiated more then 1 mSv/y, otherwise we ought to die of disease sooner or later; 2) we can no longer place confidence on professionals and experts, because they made mistakes in foreseeing earthquake, tsunami, accident progression; or they tried to conceal the reality of low radiation effect, etc. There is an aspect that the mixture of the following three factors created this kind of information pollution:

- Unprepared or imprudent explanations by professionals/experts of the sever accident and radiation effect,
- Reports by mass media like newspaper, TV program, weekly magazines etc., and
- Internet spreading of labeling without proof.

Typical labeling is that he is: 1) a member of "Genshiryoku-mura," and 2) a scientist under the government's thumb ("Goyo-gakusha" in Japanese).

"Genshiryoku-mura" can be Nuclear Village in direct translation. Here the word "mura (village)" means a narrow-minded concession sector that must have made undue profits of nuclear business. Thus, it has much more sense of jeering by anti-nuclear people against pro-nuclear society.

On the whole, we see an excess emotionality or antagonism in such a labeling with inadequate understanding of fact. Nonetheless, there is an unconcealable reality of the labeling.

In this study, by using an axiological approach[2], we will discuss the origin and structure of so-called Genshiryoku-mura in reference to the case of the Nuclear Engineering Course of Kyoto University, which is the first established in Japan in 1957. Here the axiological approach means the structure is analyzed beyond the boundary between the peaceful use of nuclear energy and the weapon use of nuclear.

2. Genshiryoku-mura –its origin and structure in reference to the ancestor of Japan's nuclear engineering in university-

2.1 A Precursor

In the very early stage of Japan's nuclear research, a physicist Ryokichi Sagane played very important role, who was a professor of physics in the University of Tokyo. He worked with Yoshio Nishina and built a large cyclotron at Institute of Physics and Chemical Research (IPCR). The cyclotron was used for the research of Japan's research for nuclear bomb that is called "Ni-Go Project."[3] In the meantime, another similar project called "F-Go Project was going on under Professor Bunsaku Arakatsu of Kyoto University.[4] After the Second World War, in 1949, Sagane went to US and worked for a study of nuclear engineering at the Laurence Baerkeley Institute of the University of California. Then he explained the possibility of the peaceful use of nuclear to those who visited him as the representatives of delegations from Japan. Among them was a former P.M. Yasuhiro Nakasone who submitted the first atomic energy budget in 1954 [5, 6].

Photo 1 Dr. Ryokichi Sagane, a precursor of nuclear engineering in Japan.

Based on such facts, we can consider Dr. R. Sagane was a precursor of the atomic energy research groups in

Japan down to the present. Sagane was a son of Hantaro Nagaoka who learned physics under Ludwig Boltzman and developed an early planetary model of the atom in 1904. He was well-distinguished pioneering nuclear physicist and he was one of the teachers of Hideki Yukawa, who won the first Nobel prize as Japanese. When Nagaoka was the president of Osaka University, Yukawa became an associate professor there, and the full professor of Kyoto University in 1939 just after obtaining doctor of science degree at Osaka University. Nagaoka predictively talked “we will go into an atomic age so that also in the field of industries will go on the same way …” as early as 1948.[7]

After his resignation as a professor of the University of Tokyo in 1955, Sagane held various posts such as the vice-president of Japan Atomic Energy Research Institute (JAERI, now Japan Atomic Energy Agency), a councilor of Atomic Energy Commission, the vice-president of The Japan Atomic Power Company.

2.2 The Origin of Nuclear Engineering at Kyoto University

The department of nuclear engineering of the Kyoto University graduate school of engineering was established in April 1957. In succession, its undergraduate course started in April 1958. It consists of 8 chairs (Table 1).

Table 1 Establishment of the 6 chairs at nuclear engineering department of Kyoto University

	Chair name	Created date	First professor
1st	Nuclear Reaction Engineering	31 March 1957	Gentaro Araki
2nd	Isotope Engineering	31 March 1958	Shinzo Okada
3rd	Reactor Engineering	31 March 1959	Hiroshi Nishihara
4th	Reactor Material Engineering	31 March 1959	Jun Oishi
5th	Nuclear Device Engineering	1 April 1960	*Hiroshi Nishihara*
6th	Nuclear Fuel Engineering	1 April 1961	*Jun Oishi*

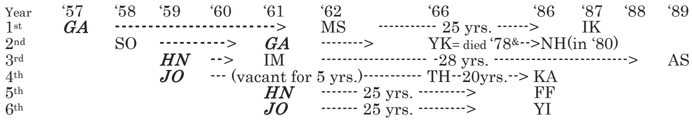

Fig. 1 Basis of the family tree of nuclear engineering department in Kyoto University.

(GA$^{*\#}$: G. Araki, SO*: S. Okada, HN$^{*\#}$: H. Nishihara, JO$^{*\#}$: Jun Oishi, IM: Itaru Michiyoshi, MS*: Masakatsu Sakisaka, YK: Yasuhisa Katayama, TH*: Tomonori Hyodo, KA*: Kunio Azuma, FF*: Fumio Fukuzawa, YI*: Yasuhiko Itoh, IK*: Itsuro Kimura, NH*: Norio Hosizaki. Those who are marked with * left at retirement age, and # moved from post to post. Note that Yasuhisa Katayama (YK) died of illness at the age of 52.[8])

Gentaro Araki, the professor of the 1st chair, graduated from Tokyo Liberal Arts and Science University in 1932 and moved to Kyoto University in 1943, then in the next year he was promoted to a full professor of the department of chemical engineering. He was a physics chemist and studied proactively adopting the theory of quantum physics in chemical engineering. During that time, he interacted with Yukawa. The then dean of School of Chemical Engineering Risaburo Torikai planned to introduce quantum mechanical thinking power into chemical engineering. Yukawa mediated between Torikai and Araki.[9] In this context, Yukawa created the basis of the startup of nuclear engineering of Kyoto University.

After four years' professor of the 1st chair, Araki moved to the 2nd chair. Then five years later, he took mandatory retirement. After Araki, Yasuhisa Katayama attained the position by a strong invitation by Yukawa. Katayama was a pure elementary particle physicist and well known as Yukawa's most favorite disciple.

2.3 Early Stage Research Activity

In 1959, three students completed master's degree, and five in 1960. Table 2 listed the research titles and mentors.

Table 2 Early stage research activity

	Title	Mentors
1959		
Y. Ikebe	Measurement of Gamma-Ray Output by Ionization Chamber	NA (*not written on his thesis*)
M. Higashi	Several Experimental Studies concerning Reactor Neutron Measurements	**Sakae Shimizu** (Institute for Chemical Research. Kyoto UNiv.) Tomonori Hyodo
T. Matsubara	On the Stability of the Induction Pinched Plasma	NA (*not written on his thesis*)
1960		
B. Makino	Detection of Uranium Fission by Scintillation Detector	**Sakae Shimizu** Tomonori Hyodo
H. Masaki	Subcritical Experimental Device	**Sakae Shimizu**
S. Matsuura	On the Fast Neutron Effect in Subcritical Device	**Sakae Shimizu**
H. Nishihara	Study on Stability Limit Thermal Power in Boiling Light Water Reactor	Hiroshi Nishihara
S. Yabushita	Isotope Shift of Helium	NA

The data tells us that half of the 8 students were supervised by Professor Sakae Shimizu of Institute for Chemical Research. Sakae Shimizu graduated from the Department of Science, Kyoto University in 1940 and became the professor of Institute for Chemical Research in 1952. During the Second World War, he worked under Bunsaku Arakatsu for F-Go Project.

The basis of the family tree, Fig. 1, tells that at the dawn of the nuclear engineering G. Araki was in the center of initiating and developing of the department. The 6 chairs were established in four years and the leading professors. i.e., Araki and Okada, left in 10 years. Then younger full professors in their 30s succeeded them and stayed at the same positions for about 30 years until retirement age. The initial professors transferred to another chair to set up a new chair.

The management capability seemed to be more important than the expert knowledge. G. Araki was a pure theoretical physicist whose prominent works on nucleus are, for instance, the quantum mechanical derivation of the mass deficiency of a nucleus and the quantum mechanical basis of atomic nucleus shell structure. He must try to apply such knowledge on nucleus physics to nucleus engineering at the 1st chair as well as the 2nd. In the meantime, at the supervising of early students, Shimizu played an important role. He is not a professor of the department. He is an experimental nuclear physicist whose prominent work was isotope separation by using cyclotron.

At the early stage, Japanese scientists had no experience of making fission, needless to say, fission chain reaction and reactor criticality. Therefore, theory and experiment in F-Go Project, a Japanese nuclear bomb project, might be efficient at the education in the department of nuclear engineering.

Photo 4 Dr. Sakae Shimizu, an experimental nuclear physicist who played a leading role.

3. Summary

- The first step of becoming a “Genshiryoku-mura” in the sense of the narrow concession sector could be the fact that physicist community separated from atomic energy research around the year of 1954 to1957. The root of mental background of the “Goyo-gakusha” labeling is in the separation.
- In the early stage of the education and research in nuclear engineering, nuclear physicists played significant role who worked for Japan’s nuclear bomb research during the Second World War.

Acknowledgments

The author expresses his gratitude to Drs. Masako Bando (Jein), Yuichiro Manabe (Osaka University), Akihiro Tosaki (Osaka University), and Shinji Mitani for their cooperations, discussions, and suggestions.

Nomenclature

Goyo-gakusha: a scholar or scientist under the government’s thumb

Genshiryoku-mura: a pro-nuclear concession sector

References

1. L. ORMAN, “Fighting Information Pollution with Decision Support Systems,” *Journal of Management Information Systems*, **1**, *2*, pp. 64-71 (1984).
2. T. SAWADA, “An Introduction to the Axiology of Nuclear Energy,” *Journal of Nuclear Science and Technology*, **42**, *5*, pp. 419-422 (2005).
3. M. YAMAZAKI, *Japan’s Nuclear Development: 1939 – 1955 – From Nuclear Bomb to Atomic Energy*, (in Japanese), pp. 37-43, Sekibundo, Tokyo (2011).
4. Id. at pp. 44-53.
5. JAPAN ATOMIC INDUSTRIAL FORUM, Inc., edited by K. MORI, *Atomic Energy, Now – Japan’s Peaceful Use for 30 Years (Volume One),* (in Japanese), pp. 6-8, Marunouchi Publising, Tokyo (1986).
6. Y. NAKASONE, The Mythical Age of Atomic Energy, (in Japanese), *Journal of Atomic Energy Society of Japan*, **49**, *2*, pp. 112-116 (2007).
7. H. NAGAOKA, *The Dawn of Age of Atomic Energy*, (in Japanese), p. 206, Nihon Tosho Center, Tokyo (republished in 1999)
8. EDITING COMMITTEE OF “BOOKLET OF THE INTRODUCTION OF KYOTO UNIVERSITY,” *Kyoto University – Present Situation and Prospects of Education and Research*, (in Japanese), pp. 140-149, Kyoto University, Kyoto (1997)

9. Y. SAKAMOTO, In Commemoration of Prof. Gentaro Araki, (in Japanese), Journal of The Physical Society of Japan, **36**, *1*, pp. 79-80 (1981)

D. Advanced Medical Application Division

D.1

PIXE Measurement on the Effect of Excessive Strontium Absorption in Plants

Yoshiyuki Oguri, Wenkai Teng, Hitoshi Fukuda

1. Introduction

In relation to migration of strontium 90 (^{90}Sr) released by nuclear accidents to agricultural products, PIXE (Proton Induced X-ray Emission) analysis is being performed for Sr in plants grown by hydroponic cultivation with culture solutions spiked with stable Sr isotopes[1,2]. So far, culture solutions with relatively high Sr concentrations (1−5 meq/L) are used for preliminary experiments. However, since the final goal of this study is to clarify the absorption behavior of plants for ultratrace-level Sr, the Sr concentration in the solution should be so low that no effect occurs in the absorption behavior as well as the growth of the plants. On the other hand, if such an effect occurs, the effect should be studied in detail beforehand.

Phosphorus (P) and potassium (K) are included in the three major nutrients for plants. Since plants contain a large amount of these elements, measurement of these elements in plant samples by PIXE analysis is relatively easy. The physiological roles of these elements in plants differ from each other (A.V. Barker and D.J. Pilbeam, Handbook of Plant Nutrition, CRC Press, ISBN: 9781420014877 (2016)). Accordingly, when a plant receives some stresses, the ratio between concentrations of these elements can deviate from the normal value.

In this study, the ratio between P and K concentrations in the plants was investigated as a function of the Sr concentration in the culture solution using PIXE analysis. From the results, we can investigate whether or not the absorption behavior for elements as well as the growth of the plant samples is affected by administration of Sr compounds.

2. Experimental methods

Basil (*Ocimum basilicum*) and sage (*Salvia officinalis*) were grown using a commercially available hydroponic culture kit (Green Farm Cube UH-CB01G1, U-ing Co.). Details of the sample cultivation has been reported elsewhere[1,2]. $SrCl_2$ and $Sr(NO_3)_2$ were employed as the Sr compounds added to the culture solution. The cultivation conditions, such as the concentration and the chemical form of Sr, are listed in table 1. All of the sample plants were cultured for 11 days. The whole plant including the root, stem and the leaves was ashed by ignition in the atmosphere. The ash was dispersed in distilled water. The suspension was dropped on an 11-μm polycarbonate film and dried to prepare a target for proton irradiation. The PIXE analysis was performed using a 2.5-MeV proton beam from the 1.6-MV tandem Pelletron accelerator at Laboratory for Advanced Nuclear Energy, Tokyo Tech in a similar manner to previous work[1,2].

Table 1 Culture conditions for the plant samples

No.	Plant species	Sr in culture solution		Fresh weight
		Compound	Concentration	
1	Basil	$SrCl_2$	5 meq/L	42 mg
2	Basil	$Sr(NO_3)_2$	1 meq/L	57 mg
3	Sage	$Sr(NO_3)_2$	1 meq/L	64 mg

3. Results and discussion

A PIXE spectrum measured for the sample No. 3 in table 1 is shown in Fig. 1 as an example. We clearly see peaks of K_α and K_β X-rays of Sr which originate from Sr absorbed by the plant from the culture solution. Also, among the elements in the culture solution, some elements such as P, K, Ca, Mn, Fe, Cu and Zn can be identified. We determined the total count of the Sr-K_α X-rays by simply summing up the count of each channel of the peak. The total counts of the K_α X-rays of P and K were evaluated by Gaussian fitting after subtraction of continuous backgrounds.

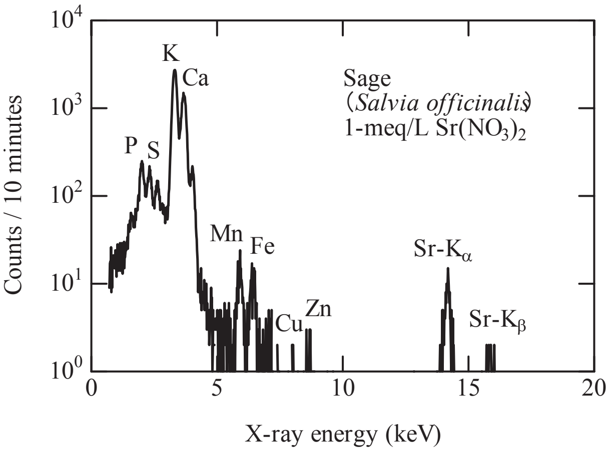

Fig. 1 An example of a PIXE spectrum of an ashed plant sample

Figure 2 (a) shows the measured P-K_α / K-K_α X-ray count ratio as a function of the Sr concentration in the culture solution. This graph indicates the relative concentration of P normalized to the K concentration in each plant sample. Although the difference due to the plant species is significant, we see a tendency that the absorption of P is small when the Sr concentration in the culture solution is high. On the other hand, Fig. 2 (b) shows a similar plot, but the abscissa is the ratio between the counts of Sr-K$_{\alpha}$ and K-K$_{\alpha}$ X-rays measured for each plant sample. This figure depicts the influence by the actual amount of Sr absorbed by each sample. We see that the more Sr is absorbed, the less P is absorbed, like in the case of (a). It is known that even K concentration in plants can change, for example, by salinity stress (M.A. Botella, V. Martinez, J. Pardines and A. Cerda, J. Plant Physiol., Vol. 150, pp. 200–205 (1997)). Therefore it should be confirmed whether the normalization by the K-K$_{\alpha}$ X-ray count is appropriate or not.

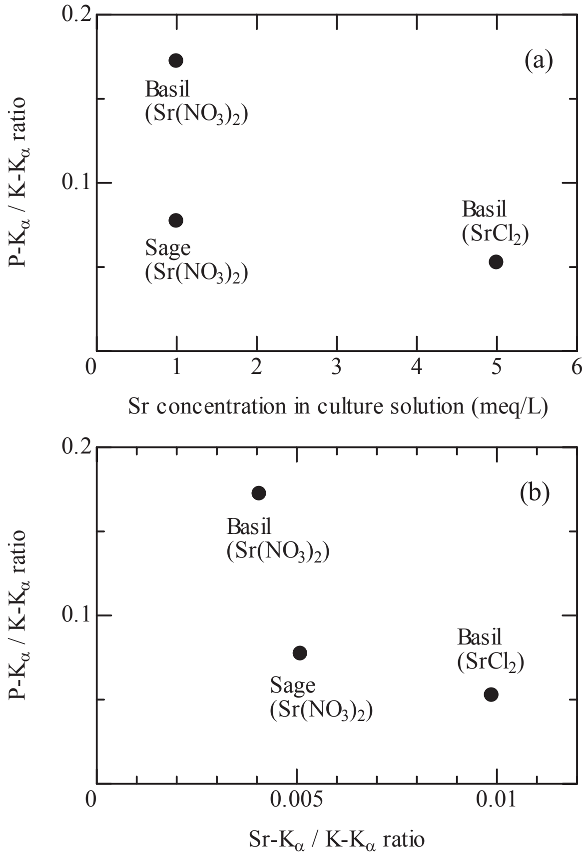

Fig. 2 Change of the P-K$_{\alpha}$ / K-K$_{\alpha}$ count ratio due to the change of (a) Sr concentration in the culture solution and (b) Sr-K$_{\alpha}$ / K-K$_{\alpha}$ count ratio, which reflects the amount of Sr absorbed in each plant sample.

4. Conclusions

From the results above, one sees that the plant samples used for the experiments were affected by the administration of Sr. In addition, actually, when the Sr concentration in the culture solution was raised up to 5 meq/L (sample No. 1 in Table 1), the growth rate of the plant was obviously low compared with the case where no Sr compound was added. It follows that this plant sample could be subjected to some stress due to the administration of Sr. Such a situation is not desirable as an experimental condition for the study of absorption behavior for ultratrace-level Sr.

However, according to the intensity of the Sr-K$_{\alpha}$ X-rays measured in the present work, it is expected that we can quantify Sr in the plant samples with sufficient precision, even if the Sr concentration in the culture solution is reduced by a factor of 10. Because the concentration of K in plants is not always stable, in the next experiment we plan to verify our expectation by quantitative analysis using, for example, an internal standard technique.

Acknowledgment

The authors thank Syukria Kurniawati, Center for Applied Nuclear Science and Technology, National Nuclear Energy Agency (BATAN), Indonesia, for fruitful discussion.

References

1. Y. Oguri, S. Kurniawati, W. Teng, K. Kondo and H. Fukuda, 31th Symp on PIXE in Japan, #3-4, October 28–30, 2015, Takasaki Advanced Radiation Research Institute, Japan Atomic Energy Agency, Takasaki, Japan (2015).
2. Y. Oguri and K. Kondo, Bull. Res. Lab. Nucl. Reactor, Vol. 39, pp. 29–30 (2015).

D.2 Identification of XRCC4 Extremely C-terminal (XECT) Region Highly Conserved in Vertebrate And Essential for DNA Repair

Rujira Wanotayan, Mikoto Fukuchi, Shoji Imamichi, Sicheng Liu,
Mukesh Kumar Sharma, Yoshihisa Matsumoto

1. Introduction

DNA double-strand break (DSB), which is considered the most lethal type of DNA damage, is repaired through homologous recombination (HR) and non-homologous end joining (NHEJ) in eukaryotic cells. NHEJ is utilized also in V(D)J recombination in immune systems. In NHEJ, a heterodimer of Ku70 and Ku86 first binds to the end of DNA and in turn recruits DNA-PKcs. When the DNA ends are not ready for ligation, they undergo processing by enzymes like Artemis, polynucleotide kinase/phosphatase (PNKP) and DNA polymerases μ/λ. Finally, DNA ends are ligated by DNA ligase IV (LIG4), which is regulated by XRCC4 and XLF.

XRCC4 consists of N-terminal globular head domain (1-115), middle stalk domain (119-203) and C-terminal domain. Two XRCC4 molecules form a dimer through coiled-coil interaction mediated through middle stalk domain. The interface with LIG4 also lies in middle stalk domain, especially 173-195. XRCC4 and XLF interact with each other through N-terminal globular head domain. There have been several studies showing that N-terminal ~200 amino acids of XRCC4 are sufficient for its function in DNA repair and V(D)J recombination. On the other hand, the function of C-terminal domain has been less identified. C-terminal region is structurally disordered and less conserved, *e.g.*, between human and budding yeast, than N-terminal and middle domains.

2. Highly conserved sequence in the extremely C-terminal region of vertebrate XRCC4

The amino acid sequences of XRCC4 proteins of various species were retrieved from NCBI database. It was noticed that the sequence of ~20 amino acids at the extremely C-terminus is highly conserved among wide range of vertebrate species including mammal (*Homo sapiens* and *Mus musculus*), bird (*Gallus gallus*), reptile (*Anolis carolinensis*), amphibian (*Xenopus laevis*) and fish (*Danio rerio*) (Fig.1). Especially, the amino acids corresponding to asparagine (N) 326, proline (P) 329, leucine (L) 332 and phenylalanine (F) 333 of human XRCC4 are conserved among all the species listed here. It is also noteworthy that this region is enriched in acidic amino acids, *i.e.*, aspartic acid (D) and glutamic acid (E). Interestingly, this motif is not found in organisms other than vertebrate. We named this region XECT (X̲RCC4 e̲xtremely C̲-t̲erminal) region.

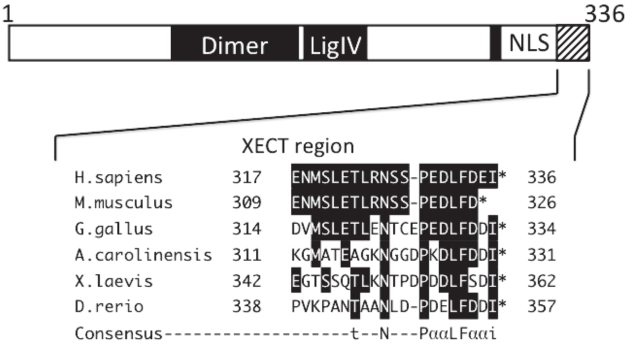

Fig.1 Alignment of the amino acid sequences in the extreme C-termini of XRCC4 proteins from various vertebrate species. In “Consensus”, characters in uppercase show the amino acids, which are common among all of the species, and characters in lowercase shows the amino acids, which are common among five out of six species. “α” indicates conserved acidic residues.

3. Asparagine 326 in XECT essntial for the cell survival after irradiation

To explore its possible importance, series of mutants in this region were constructed and assessed for the functionality in terms of ability to rescue radiosensitivity of M10 cells lacking XRCC4 (Fig.2). Among 13 mutants, M10 transfectant with N326L (Asparagine 326 changed into leucine) mutant showed elevated radiosensitivity, indicating the importance of the extremely C-terminal region of XRCC4 and, especially, Asn326 therein.

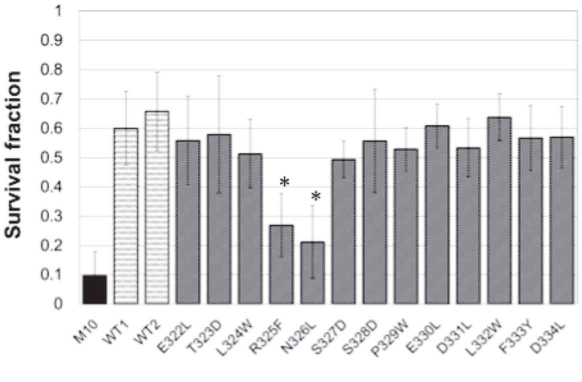

Fig.2 Survival of the cells expressing XRCC4 mutated in XECT region after 2 Gy □-irradiation

Reference

1. R. Wanotayan, et al.; Biohemical and Biophysical Research Communications, Vol.457, pp. 526-531 (2015).

D.3 Regulation of the nuclear localization of XRCC4/DNA ligase IV complex

Mikoto Fukuchi, Rujira Wanotayan, Shoji Imamichi, Mukesh Kumar Sharma, Yoshihisa Matsumoto

1. Introduction

XRCC4 and DNA Ligase IV (LIG4) cooperate to join two DNA ends at the final step of DNA double-strand break (DSB) repair through non-homologous end-joining (NHEJ). However, it is not fully understood how these proteins are localized to the nucleus.

The sequence RKRRQR, spanning amino acids 270-275 of human XRCC4 is considered the nuclear localization signal (NLS). Earlier studies showed that deleting amino acids 250-300 or 266-334 of human XRCC4, containing this putative NLS, resulted in defective nuclear localization. We sought to examine more precisely the functionality of this putative NLS by creating a point mutant. We chose lysine at the second position, *i.e.*, lysine 271 in human XRCC4, and changed it into arginine to preserve positive charge, creating XRCC4^{K271R} mutant.

2. Lysine 271 but not lysine 210 of XRCC4 required for the nuclear localization of XRCC4 and DNA ligase IV

We created and analyzed XRCC4^{K271R} mutant, in which highly conserved lysine 271 had been changed into arginine. We also created XRCC4^{K210R} mutant, as an earlier study showed that K210 undergoes SUMOylation and that SUMOylation is necessary and sufficient for the nuclear localization of XRCC4. XRCC4^{WT}, XRCC4^{K271R} and XRCC4^{K210R} with EGFP tag were introduced into HeLa cell, in which endogenous XRCC4 had been knocked down using siRNA directed to 3'-UTR, and tested for the nuclear localization function. XRCC4^{K271R} was defective in the nuclear localization of itself and LIG4, whereas XRCC4^{K210R} was competent.

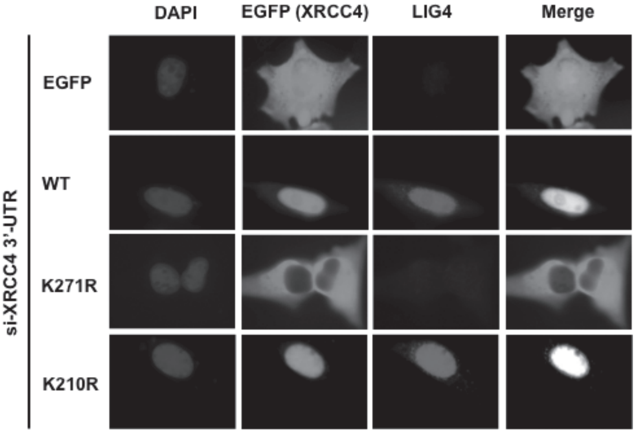

Fig.1 Subcellular localization of wild-type and mutated XRCC4 and their abilities in driving nuclear localization of LIG4.

3. Models for the nuclear localization of XRCC4 and LIG4

Nuclear localization would have two requirements: import into the nucleus and stability in the nucleus. Two models can be considered for the nuclear import of XRCC4 and LIG4 (Fig.2). In the first model, XRCC4 and LIG4 are imported to the nucleus together by means of either XRCC4 NLS or LIG4 NLS (Fig.2A). In the second model, XRCC4 and LIG4 are imported separately into the nucleus and associate with each other in the nucleus (Fig.2B). According to the first model, XRCC4 and LIG4 would have been imported into the nucleus by means of LIG4 NLS, even if XRCC4 NLS was dysfunctional (Fig.2C). According to the second model, LIG4 should have imported into the nucleus in XRCC4^{K271R} cells but would be unstable because of the absence of XRCC4 in nucleus (Fig.2D). Thus, the present results would be more compatible with the second model.

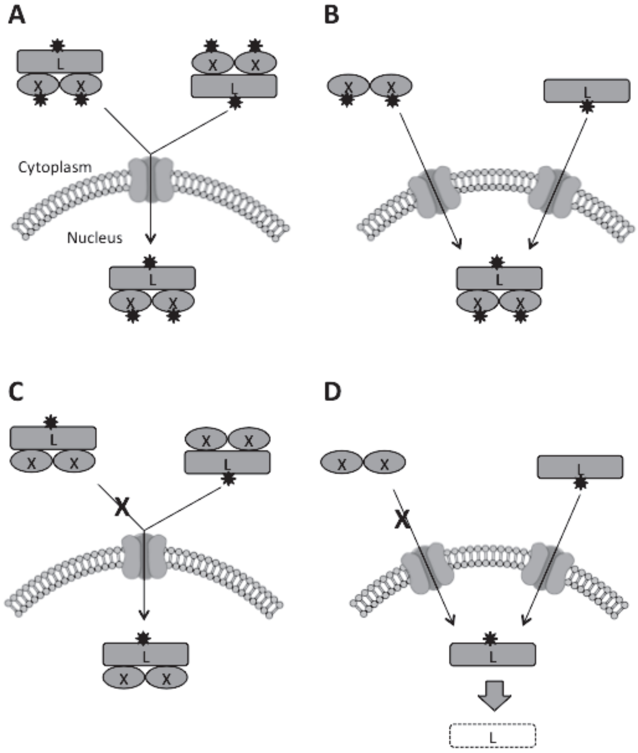

Fig.2 Possible models for the nuclear localization of XRCC4 and LIG4. Ellipses (X) and rectangles (L) stand for XRCC4 and LIG4, respectively. Asteroids indicate for NLS.

Reference

1. M. Fukuchi, et al.; Biohemical and Biophysical Research Communications, Vol.461, pp. 687-694 (2015).

D.4 XRCC4 serine 320 phosphorylation as the indicator for DNA-PK activity

Mukesh Kumar Sharma, Shoji Imamichi, Mikoto Fukuchi,
Ravindra Mahadeo Samarth, Yoshihisa Matsumoto

1. Introduction

DNA-dependent protein kinase (DNA-PK), consisting of Ku70, Ku86 and DNA-PKcs, is an enzyme that catalyzes protein phosphorylation and acts as the double-strand break (DSB) sensor in DSB repair through non-homologous end joining. There are lines of evidence indicating that the catalytic activity of DNA-PK is essential for its repair function. However, till now the targets and roles of phosphorylation remain unclear. It was shown that XRCC4 protein, which is associated with DNA ligase IV, undergoes phosphorylation by DNA-PK in response to DNA damage. Several groups have identified serine 260 and serine 320 (hereafter Ser320) as the major phosphorylation sites in XRCC4 by purified DNA-PK *in vitro* through mass spectrometry. However, the XRCC4 mutants lacking these phosphorylation sites did not exhibit any discernable defects in supporting cellular survival after irradiation and V(D)J recombination, leading to the conclusion that XRCC4 phosphorylation by DNA-PK was unnecessary for these functions. Nevertheless, it is presently unclear whether these sites are phosphorylated in living cells in response to DNA damage. In the present study, we generated a rabbit polyclonal phosphorylation-specific antibody against XRCC4 Ser320 (α-XRCC4-pS320) and examined its phosphorylation status in living cells after irradiation.

2. Detection of radiation-induced phosphorylation of XRCC4 Ser320 by DNA-PK in living cells

Human cervical cancer-derived HeLa cells were harvested 30 min after irradiation with 20 Gy of γ-ray. To examine the role of DNA-PK in the phosphorylation of XRCC4 Ser320, we employed an inhibitor of DNA-PK, NU7441. Since ATM (ataxia-telangiectasia mutated) exhibits similarity to DNA-PKcs in structure and biochemical properties, we also tested the effects of an inhibitor of ATM, KU55933. In the absence of inhibitors, there was the appearance of a band of ~55 kDa, which was greatly enhanced by irradiation (compare lane 1 and lane 2). NU7441 greatly diminished XRCC4 Ser320 phosphorylation (compare lane 2 and lane 4). On the other hand, KU55933 did not affect XRCC4 Ser320 phosphorylation (compare lane 2 and lane 6). The total XRCC4 remained unchanged after irradiation (α-XRCC4) or in the presence of inhibitors. The phosphorylation of XRCC4 Ser320 was detected even after 1 Gy irradiation and increased in a manner dependent on radiation dose.

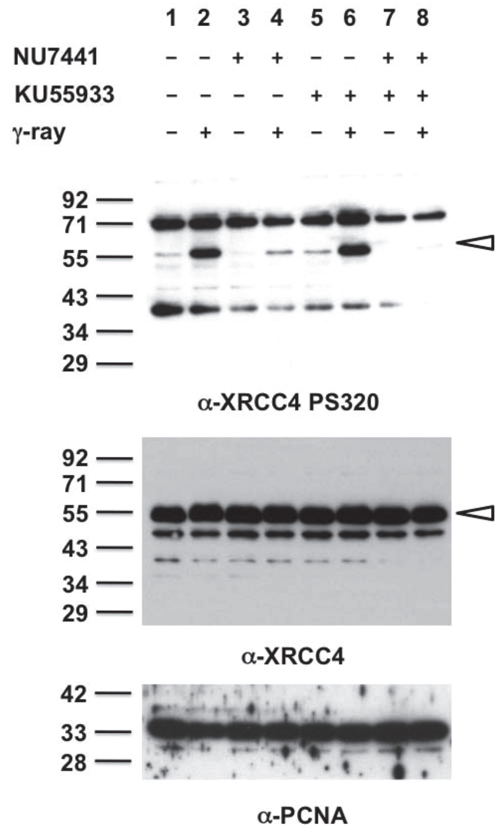

Fig.1 Western blotting analysis using phosphorylation-specific antibody (α-XRCC4-pS320) and general XRCC4 antibody (α-XRCC4). Open arrowheads indicate the position of XRCC4 (55 kDa). Western blotting using α-PCNA is also shown as the loading control.

3. Application potential of XRCC4 Ser320 phosphorylation

XRCC4 Ser320 phosphorylation status enables us to monitor DNA-PK activity and functionality in living cells, which can be used to aid the prediction of radiosensitivity and cancer susceptibility. It would be also useful in the evaluation of the in situ activity of DNA-PK inhibitors, which is being developed as the radiosensitizers.

Reference

1. M.K. Sharma, et al.; Journal of Radiation Research, Vol.57, pp. 115-120 (2016).

D.5 Generation of DNA repair factor XRCC4 knock out cells using genome editing

Mikio Shimada, Masanori Matsumiya, Yoshihisa Matsumoto

1. Introduction

Maintenance of genome stability is important for biological homeostasis. Ionizing radiation (IR) induce several DNA damage, such as DNA single strand breaks (SSBs) and double strand breaks (DSBs). In mammalian cells, there are two pathways of DSBs repair mechanism. One is non-homologous end joining (NHEJ) repair, which is join DNA ends directly, another one is homologous recombination (HR) repair, which is repaired with homologous chromosome. XRCC4 is an important factor in NHEJ pathway. Meanwhile, genome editing system is useful tool to generate knockout cells. Especially, CRISPR/Cas9 system is convenience and well developed. In this study, to investigate function of XRCC4, we established XRCC4 knockout cells using CRISPR/Cas9 system in HCT116 cell line.

2. Materials and Methods

2.1. Cell line

Hela and HCT116 cells were cultured with D-MEM supplemented with 10% bovine calf serum, penicillin-streptomycin and incubated with 5% CO^2 at 37° C.

2.2. CRISPR/Cas9 plasmid vector

To generate knockout cells, pX330 vector was obtained from Addgene (Fig. 1).

2.3. Transfection

CRISPR/Cas9 plasmid DNA vector was transfected into cells using lipofectamin 2000 (Invitrogen)

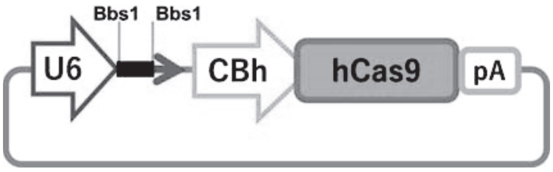

Fig. 1 Map of pX330 DNA plasmid vector

2. Results and Discussions

Generation of XRCC4 knockout cells

XRCC4 CRISPR gRNA sequence was designed with CRISPR design website from Dr. F. Zhang Lab (http://crispr.mit.edu). gRNA sequence was inserted into pX330 plasmid vector and amplified in E. Coli. DNA vector was transfected into HCT116 cells by lipofection method. After 10-14 days incubation, cells were isolated into 24well plates. About 60 clones were picked up and XRCC4 expression level of each clones were evaluated by western blotting. Expression of XRCC4 in 7 clones (10, 11,12,16, 17,18, 20) was disappeared (Fig. 2). To confirm this result, we performed immunostainig using XRCC4 antibody and phosphorylated H2AX (γH2AX), as DSBs marker. XRCC4 expression was disappeared in 3 clones and interestingly, γH2AX positive cells were increased in XRCC4 deficient cells (Fig. 3).

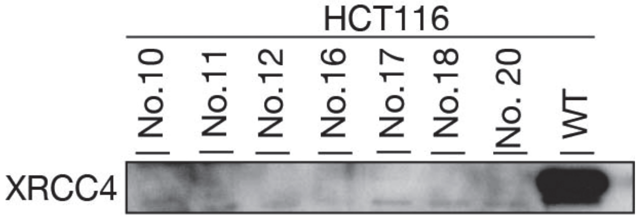

Fig. 2 Expression level of XRCC4 in HCT116 cells. Protein extracts from HCT116 cells were performed with western blotting analysis. No. 10, 11, 12, 16, 17, 18, 20 represent XRCC4-CRISPR/Cas9 transfected clones.

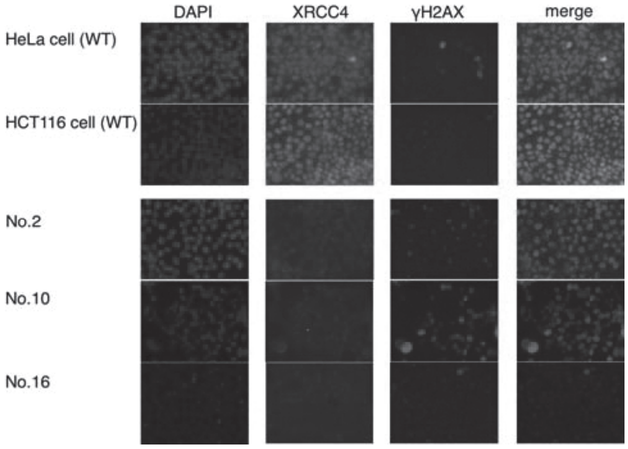

Fig. 3 Expression level of XRCC4 in HCT116 cells. Protein extracts from HCT116 cells were performed with Immunostaining analysis. No. 2, 10, 16 cells represent XRCC4-CRISPR/Cas9 transfected clones.

Acknowledgment

The authors thank to Dr. Matsumoto laboratory members and Dr. Yasuhara (University of Tokyo) for helpful discussion.

Reference

1. M. Matsumiya, et al.; 59th Annual meeting of Japanese Radiation Research Society, October 26-28, Hiroshima (2016)

E. Fundamental Research Division

E.1 Various theoretical approaches in order to understand fission mechanisms in actinide region

Satoshi Chiba

1. Introduction

Prediction of the fission properties of exotic heavy systems such as minor actinides are crucial not only for the safety of the high burn-up nuclears and light water reactors but also reduction of the decommission costs of nuclear reactors. However, the experimental data on the fragment charges are still limited compared to the mass and TKE data, although measurements of isotopic yield using the inverse kinematics have made great progress. Our aim is to understand the fission mechanism at low energy including the charge distribution of fission products and emitted neutrons form them, and to provide high quality data for minor actinides theoretically.

For the above aim, we have developed the Langevin model, which tracks the dynamical history of a system with only a few essential variables. The Langevin model follows the equation of motion with statistical friction and fluctuations. In our model, we solve the time-evolution of a compound nucleus using potential energy based on the two-center shell model, quantum correction to that potential and transport coefficients such as friction tensor and inertia. Our model successfully provides mass yields and TKE of fission products of various actinides at relatively excited system in good agreement with experimental data.

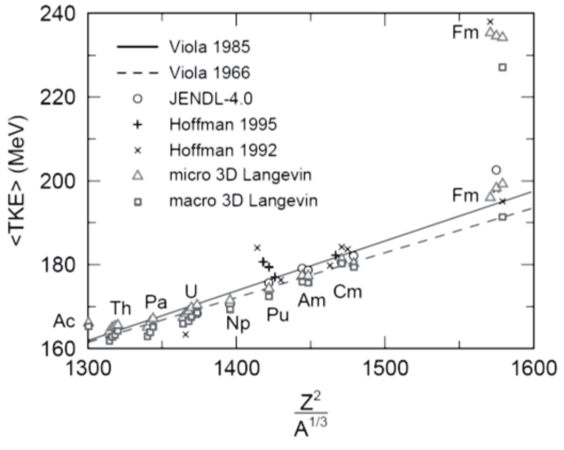

Fig. 1 Average total kinetic energy (TKE) of fission fragment for various fissioning system. Our calculation with microscopic and macroscopic transport coefficients are given by triangles and squares, respectively.

In Figure 1, we compare the calculated average total kinetic energy (TKE) of fission fragments of various fissioning systems (as expressed by $Z^2/A^{1/3}$) with experimental data. The calculations were done with microscopic transport coefficients (triangles) and macroscopic ones (squares). Both calculations can reproduce the trend predicted by Viola's systematics. The anomalous high TKE component for Fm is also reproduced quite well by our microscopic calculations.

However, in order to provide information on thermal fission and that on delayed neutrons, we need to extend our three-dimensional Langevin model [1] by considering a potential-sensitive friction tensor such as the linear response theory, and by adding the degree of freedom on charge fluctuation. Also, full 4D-shape Langevin calculation is in progress. In this paper, we propose two extensions of the Langevin model [1] for the isotope distribution and for low energy fission, separately.

2. Isotope distribution of fission product based on the dynamical model

2.1.Modification of the basic Langevin model

We describe the shape of a compound nucleus, using the two-center shell model by three variables. They correspond to distance between the two centers of mass *z,* deformation δ, and mass asymmetry η_A. In order to treat the isotope distributions, we introduce a new variable η_Z for the charge mode. Here, η_Z corresponds to the charge asymmetry. The Langevin approach treats nuclear fission as a Brownian motion of particle representing by the chosen collective variables. In the equation of motion, the dissipation term and the fluctuation term for the Brownian motion, are added as follows.

$$\dot{q}_i = m_{ij}^{-1} p_j$$

$$\dot{p}_i = -\frac{\partial V}{\partial q_i} - \frac{1}{2}\frac{\partial}{\partial q_i} m_{jk}^{-1} p_j p_k - \gamma_{ij} m_{jk}^{-1} p_k + g_{ij} R_j(t) ,$$

where m_{ij}, γ_{ij}, R_j is the mass tensor, the friction tensor, and the random force, respectively. The strength of the random force is given by $\gamma_{ij}T=g_{ik}g_{kj}$. T is the heat-bath temperature defined as $T^2=E_{int}/a(q)$ using the intrinsic energy E_{int} and the level density parameter a(q), while we use the effective temperature T_Z for the charge mode.

$$E_{\text{int}} = E^* - \frac{1}{2} m_{ij}^{-1} p_i p_j - V.$$

Difference between the current work and other recent works relating to the fission properties based on the Langevin model [2, 3], is the way of the charge mode. We consider the charge mode simultaneously with other degrees of freedom within unified computational scheme solving a system of coupled equations. Note that we consider the diagonal components of these transport coefficients, m_{ij} and γ_{ij}, for the charge mode for simplicity [4,5]. It means that the mass mode in the basic Langevin model can couple with the charge mode only via the following potential.

$$V = V_{LD} + (V_{Shell}(q,T=0) + V_{Pair}(q,T=0))$$

$$= V(q_i, <\eta_Z>) + \frac{C_{\eta_Z}}{2}(\eta_Z - <\eta_Z>)^2$$

$$= V(q_i, <\eta_Z>)_{UCD} + \frac{C_{\eta_Z}}{2}(\eta_Z - <\eta_Z>)^2 - \frac{C_{\eta_Z}}{2}(<\eta_Z>_{UCD} - <\eta_Z>)^2$$

where the coefficient $C\eta_Z$ is derived from the Harmonic approximation around the most probable charge asymmetry $<\eta_Z>$ [6]. In the potential V, the symmetry energy V_{Sym} and the Coulomb energy V_{Coul} directly relate with the charge Z, then we can approximately describe the coefficient as follows.

$$C_{\eta_Z} = \left.\frac{\partial^2 V}{\partial \eta_z^2}\right|_{\eta_Z = <\eta_Z>} \cong \left.\frac{\partial^2 V_{Sym}}{\partial \eta_z^2}\right|_{\eta_Z = <\eta_Z>} + \left.\frac{\partial^2 V_{Coul}}{\partial \eta_z^2}\right|_{\eta_Z = <\eta_Z>}$$

The expectation value of the charge asymmetry at the Unified Charge Distribution (UCD) assumption, $<\eta_Z>_{UCD}$, is derived from the assumption which the ratio between the charge and the mass of a nucleus would be conserved before/after fission. The UCD assumption has been used to describe the fission system and can explain the qualitative properties of the fission fragment mass and TKE. However, for the evaluation of the fission neutron properties such as the prompt neutron multiplicity and the beta-decay heat, the charge deviation from the UCD should not be neglected.

2.1.Isotope distribution of n+^{235}U fission at E=20MeV*

We solved the Langevin equation for the compound system of ^{236}U at E^* = 20 MeV, which corresponds to n+^{235}U at E_n = 14MeV, by changing the mass asymmetry and the charge asymmetry simultaneously and independently in order to calculate the isotope distribution. Fig.2 shows fission product yields as a function of the mass number of a fragment with the charge number Z = 39. As seen in Fig. 1, the peak position and the curvature of our result can reproduce the standard evaluated libraries [7,9,10] and phenomenological model [8], qualitatively and quantitatively. Such characteristics of the calculated isotope distribution can be commonly seen in all data between Z = 39 to Z = 52. Even for the fixed mass number, such consistency with the major libraries can be also found. In the current model, we assumed the expectation value for the charge asymmetry including the charge deviation from the UCD as defined in [6]. As a result, our calculations showed good agreement without any adjustment and/or data fitting.

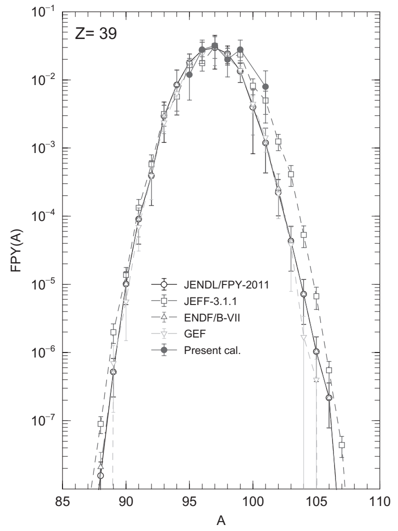

Fig. 2 Isotope distribution for Z=39

Fission product yields as a function of the mass number of a fragment with the charge number Z=39. Red line with filled circle is our calculation on a log scale. Black line with open circle is the JENDL/FPY-2011 [7] for ^{236}U thermal-fission. Blue dashed-line with open-square is the JEFF-3.1.1 [9] for ^{236}U thermal-fission. Purple dashed-line with open triangle is the ENDF/B-VII [10] for ^{236}U thermal fission. Green dashed-line with open inverted-triangle is the GEF [8] for ^{236}U thermal-fission, respectively.

Acknowledgment

The present study includes the results of “Comprehensive study of delayed-neutron yields for accurate evaluation of kinetics of high-burn up reactors” entrusted to Tokyo Institute of Technology by the Ministry of Education, Culture, Sports, Science and Technology of Japan (MEXT).

Reference

1. Y. Aritomo and S. Chiba; *Physical Review C*, Vol. 88, pp. 044614 (2013) and references therein.
2. K. Mazurek, C. Schmitt and P. N. Nadtochy; *Physical Review C* , Vol. 91, pp. 041603(R) (2015).
3. M. R. Pahlavani and S. M, Mirfathi; *Physical Review C*, Vol. 92, pp. 024622 (2015).
4. A. V. Karpov and G. D. Adeev; *The European Physical Journal A*, Vol. 14, pp. 169 (2002) and references therein.
5. A. V. Karpov and G. D. Adeev; *Physics of Atomic Nucei, Vol.* 65, pp.1596 (2002).
6. G. D. Adeev; *Fiz. Elem. Chastis At. Yadra Vol.* 23, pp.1572 (1992).
7. K. Shibata, O. Iwamoto, T. Nakagawa, N. Iwamoto, A. Ichihara, S. Kunieda, S. Chiba, K. Furutaka, N. Otuka, T. Ohsawa, T. Murata, H. Matsunobu, A. Zukeran, S. Kamada, and J. Katakura; *Journal of Nuclear Science and Technology*, Vol. 48, pp.1 (2011).
8. K.-H. Schmidt, B. Jurado, Ch. Amouroux; *JEFF-Report, Vol.* 24, pp. 1 (2014).
9. A. Santamarina et al.; *JEFF-Report, Vol.* 22, pp.1 (2009).□
10. M.B. Chadwick et al.; *Nucl. Data Sheets,* Vol. 112, pp. 2887 (2011).

E.2 Spectroscopic Observation of γ, β and δ bands of NO excited states and relevant excitation kinetics in Low-pressure N_2-O_2 Microwave Discharge

Hiroshi Akatsuka, Atsushi Nezu

1. Introduction

The discharge of N_2-O_2 mixtures has been studied because of their important roles in atmospheric and ionospheric physics. NO widely exists in oxidation processes, which causes not only environmental problems but is also toxic to organisms. However, previous researches of N_2-O_2 mixture discharge plasmas always focus on the particle with numerous number densities such as N_2, O_2 molecules, and N and O atoms. In some cases, the NO molecule is mentioned but only the NO ground state is considered. However, the basic investigation on NO molecules is not enough, especially on its excited states. Therefore, it is necessary to consider the excitation kinetics of NO metastable states in N_2-O_2 mixture discharges, because each metastable state has different population and depopulation processes, which is precisely one of the objectives of this study.

2. Experiments

A N_2-O_2 gas mixture microwave discharge is generated using a vertically placed rectangular waveguide. A quartz tube with a 26mm inner diameter is aligned in the vertical direction of the waveguide. One end of the quartz tube is connected to the gas entrance, where N_2 and O_2 are mixed beforehand. The other end of the quartz tube serves as the outlet to a vacuum chamber, which is evacuated by a rotary pump. A microwave generator (2.45 GHz) is used to drive the gaseous discharge, with flow controllers for both nitrogen and oxygen (purity 99.5%). The discharge apparatus is similar to that described elsewhere.[1, 2]

3. Results and Discussion

In our experimental observations, the β- and δ-bands (from NO B $^2\Pi$ to X $^2\Pi$, and C $^2\Pi$ to X $^2\Pi$, respectively) are observed only when the O_2 partial pressure is smaller than 3%, while the γ-band (from A $^2\Sigma^+$ to X $^2\Pi$) is always observed. Figure 1 shows two observed spectra within the range from 220 to 280 nm when the O_2 partial pressure in the discharge gas is set at 1% and 40%. From the spectra, we can see that when the O_2 partial pressure increases only slightly, the intensity of the δ-band rapidly decreases. However, under this small change in conditions, the intensity from high-vibrational levels (1 to x, for $x = 5, 6, 7, 8$) of the γ-band (from A $^2\Sigma^+$ to X $^2\Pi$) noticeably increases. We know that, when the O_2 partial pressure changes from 1% to 5%, only the number densities of O_2 molecules, its atoms, and ions increase largely.

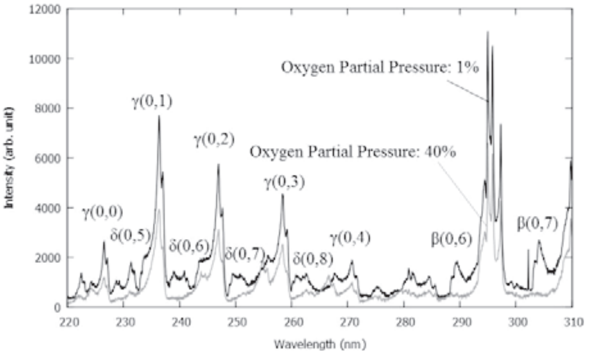

Fig. 1 Experimentally observed spectra over the 220–280 nm wavelength range with the O_2 partial pressure of 1% (black line) and 40% (grey line). The γ-, β- and δ-bands are indicated. Parentheses denote the vibrational quantum numbers (upper, lower) involved.

Therefore, we propose a molecular collisional de-excitation process according to the following reaction for the NO C $^2\Pi$ state:

$$\begin{aligned} &\mathrm{O_2}\left(\mathrm{X}\,^3\Sigma_\mathrm{g}^-, v''=0\right)+\mathrm{NO}\left(\mathrm{C}\,^2\Pi, v'=0\right) \\ &\rightarrow \mathrm{O_2}\left(\mathrm{a}\,^1\Delta_\mathrm{g}, v'=0\right)+\mathrm{NO}\left(\mathrm{A}\,^2\Sigma^+, v''=0\right). \end{aligned} \tag{1}$$

Our results show that the δ-band appears and increases its intensity as the N_2 partial pressure approaches 100%. This implies that Eq. (1) has a much larger rate coefficient than that by quenching by N_2 molecules. Meanwhile, because the resultant product of the reaction is the NO A $^2\Sigma^+$ state, the molecular vibrational properties of the A $^2\Sigma^+$ state should be partially affected by the C $^2\Pi$ state. That is, because the NO C $^2\Pi$ and A $^2\Sigma^+$ states have completely different generation processes, which leads to different vibrational properties.[1, 2] We found that, when the oxygen partial pressure ratio is modified from 1 to 3%, the vibrational temperature of the A state also varies from 2668 ± 107 to 4756 ± 190 K. We also confirmed that, as the ratio of the number density of NO C $^2\Pi$ and A $^2\Sigma^+$ increases, the vibrational temperature of the NO A $^2\Sigma^+$ state increases synchronously. This indicates the NO C $^2\Pi$ state experiences a de-excitation collision and turns into A $^2\Sigma^+$ state, which finally leads to the vibrational temperature increase of NO A $^2\Sigma^+$ state. Because in this kind of N_2-O_2 plasma, NO C $^2\Pi$ state is generating through the atomic collision between N and O, which can lead to the molecules at a high vibrational level distribution.

References

1. Hao Tan, Atsushi Nezu, and Hiroshi Akatsuka; Kinetic Model and Spectroscopic Measurement of NO (A, B, C) States in Low Pressure N_2-O_2 Microwave Discharge, Jpn. J. Appl. Phys., Vol. **54**, No. 9, 096103 (6 pages) (2015).

2. Hao Tan, Atsushi Nezu, and Hiroshi Akatsuka; Spectroscopic Investigation of the NO C $^2\Pi$ De-excitation Process by Collision with O_2 X $^3\Sigma_g^-$ in a Low-pressure N_2-O_2 Mixture Microwave Discharge, Jpn. J. Appl. Phys., Vol. **55**, No. 1S, 01AH04 (4 pages) (2016).

E.3 Experimental Study on Effect of Electric Field on Plasma Flow with Electrons Magnetized and Ions Nonmagnetized

Hiroshi Akatsuka, Atsushi Nezu

1. Introduction

Recently, crossed field (electric and magnetic) discharge devices have been used for many purposes. For example, ***E***×***B*** drift is used for space propulsion as a Hall thruster. In its channel, axial electric field and radial magnetic field is applied. It follows that electron drift is established in the ***E***×***B*** direction. Therefore ionization is increased and high thrust efficiency is provided. These orthogonal fields are also used for electron confinement device such as a Penning trap.

A lot of studies about plasma flow with crossed field are reported up to now, but the interactions between the plasma flow and the crossed fields are not examined yet very much. On the basis of this background, this study intends to understand the effect of the ***E***×***B*** drift on the plasma flow experimentally. The experimental results indicate that electrons are rotated azimuthally by effect of ***E***×***B*** drift.

2. Experimental Setup

Our plasma generator was the same one that had been described in Refs. 1 – 2. Figure 1 shows our experimental equipment consists of a rarefied gas wind tunnel, a pumping system, a plasma generator, six electromagnets, a traversing mechanism and a Mach probe. The rarefied gas wind tunnel is evacuated by the pumping system. During the stationary arc jet expansion, the background pressure is kept at least in the order of 10^{-3} Torr constantly. The further description of the apparatus was described elsewhere. In addition to this, we put another cylindrical electrode, located at the end of the electromagnets and applied orthogonal electric field to the axial magnetic field in order to understand the effect of the radial electric field on the plasma rotation. The maximum voltage applied to the electrode is ± 125 V.

We use a four-tip Mach probe to measure plasma parameters. The angle of plasma flow with respect to the probe axis and the ion Mach number M_i are determined from the ratio of each electrode ion saturation currents of each electrode. In addition, this probe can measure plasma space potential, electron temperature, and electron density as a Langmuir probe. We also interpreted the ratio of the electron saturation currents of up-down probe as electron flux. Further details were described in Ref. 3.

3. Results and Discussion

We measured space potential contour for the case of applying voltage to the electrode as + 125 V. The result shows that, space potential falls toward the center of the plasma column by about 3 V at the edge of the electromagnets. In that region, electron hall parameter is about 10^4, and ion hall parameter is about 10^1. These results indicate that only magnetized electrons rotate azimuthally as hall current, while the ions are not magnetized and moved to the direction of ***E***. In fact, electron saturation current is increased in the direction of ***E***×***B***. It indicates that hall current is generated by radial plasma space potential produced by external electrode. We found that the order of the radial electric field is about several hundred V/m, which should be caused by the difference in the degree of magnetization between electrons and ions. Electron saturation current indicates the existence of the ***E***×***B*** rotation of electrons, whose order is about 2000 – 4000 m/s and consistent with the absolute values of the measured electric field and of the applied magnetic field. Even when we do not apply the radial electric field to the plasma flow, we observed weak azimuthal rotation of the plasma. This can be considered as diamagnetic current by electrons, whose observed order is theoretically consistent, as well as with the value of the ***E***×***B*** drift motion of electrons.

References

1. J. Takeda, A. Nezu, and H. Akatsuka; Proc. Joint Symposium of the 9th Asia-Pacific International Symposium on the Basics and Applications of Plasma Technology (APSPT-9) and the 28th Symposium on Plasma Science for Materials (SPSM-28), P1-21 (2015).

2. J. Takeda, A. Nezu, and H. Akatsuka; 2016 National Convention Record I.E.E. Japan, 1-159, vol. 1, p. 187 (2016) [in Japanese].

3. J. Takeda, A. Nezu, and H. Akatsuka; Book of Abstracts, 18th International Congress on Plasma Physics (ICPP2016), PAM1-2 (2016).

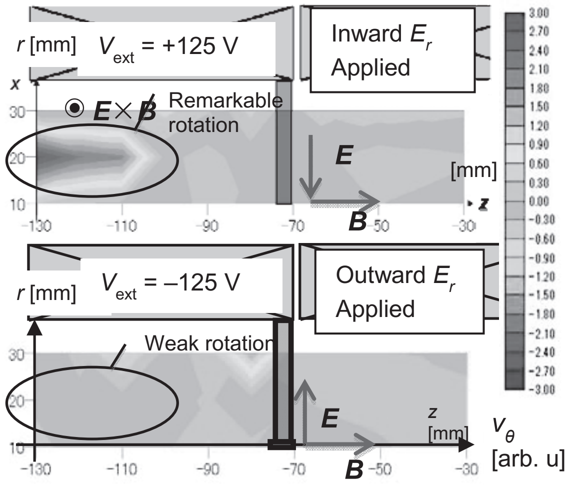

Fig. 1 Contour of the azimuthal component of the electron velocity. The external applied voltage to the ring electrode: upper + 125 V, lower – 125V.

E.4 Possibility of Electron Temperature and Density Monitoring of Argon Plasma by Intensity Ratio Measurement of Ar I lines

Hiroshi Akatsuka

1. Introduction

Low-pressure argon discharge plasmas are widely applied to semiconductor processes in electronic engineering. For precise monitoring of the plasma processes, plasma diagnostics are necessary for keeping the quality of the output materials. For these applications, optical emission spectroscopic (OES) measurement is one of the ideal plasma measurement methods, because it does not disturb the plasma itself. In general, however, the argon plasmas for semiconductor processes are in the state of non-equilibrium. Consequently, excited-state density, which is easily determined by the OES measurement, does not necessarily obey the Boltzmann law of density distribution. If we would like to calculate the number densities of the excited states of argon atom in the plasma, we should apply the collisional radiative (CR) model, where the excited-state populations are described as functions of the electron temperature T_e, the electron density N_e, and the ground-state argon density.

2. Methodology

In the present study, we surveyed the dependence of excited-state density of argon atom on the electron temperature and density over their typical range expected in the semiconductor processes, i.e., $2 \leq T_e$ [eV] ≤ 8 and $10^{10} \leq N_e$ [cm^{-3}] $\leq 10^{13}$, and the discharge pressure 7 mTorr, by applying the Ar CR model.[1] Practically, we would like to understand the state of the plasma in terms of simple parameters, like the intensity ratio of two lines from the excited states, even if it does not exactly correspond to T_e or N_e. If we need complex kinetic model to deduce them from the spectroscopic observation, it is not very practical for the industrial application. Rather, we should find characteristic values simply calculated from the experimental results, which approximately indicate T_e or N_e. We paid an attention to the number density ratios between the excited states of argon atom, which can be directly observed by the OES measurement.

3. Results and Discussion

Through the parameter survey described above, it is confirmed that anyone of the density ratios does not exactly indicate T_e or N_e. However, it is also found that the ratios between some level pairs can be interpreted as an approximate measure of electron temperature, and some others as that of electron density, over the range surveyed in the present study.

For example, the density ratio of (4p'$[1/2]_0$)/(4p$[1/2]_0$), which corresponds to the line intensity ratio of (750.4 nm)/(751.5 nm), is determined mostly by T_e and almost independent of N_e, while that of (4d$[3/2]^o$)/(4p$[1/2]_0$) or the intensity ratio (675.3 nm)/(751.5 nm) mostly by N_e and independent of T_e.

Let us consider difference between the states 4p'$[1/2]_0$ and 4p$[1/2]_0$. Radiative transition from both states to the ground state is optically forbidden (parity forbidden), and direct kinetic processes from/to the metastables are negligible. Meanwhile, we find strong coupling of these levels with resonance states due to optically allowed characteristics, i.e., 4p$[1/2]_0$ ↔ 4s$[3/2]_1$, and 4p'$[1/2]_0$ ↔ 4s'$[1/2]_1$, which is based not only on radiative process but also on electron collisions. Therefore, one of the most probable reasons is difference in the population kinetics between the resonance states 4s$[3/2]_1$ and 4s'$[1/2]_1$ with energy difference about 0.2 eV, which could result in the T_e dependence of the density ratio.[2-3]

On the other hand, we found that the density ratio (4d$[3/2]^o$)/(4p$[1/2]_0$) could be a good approximate measure of N_e over the range of $2 \leq T_e$ [eV] ≤ 8 and N_e [cm^{-3}] $\leq 2 \times 10^{12}$. Concerning the N_e dependence of this density ratio, we can point out the difference in the depopulation processes. That is, 4p$[1/2]_0$ state mainly depopulates by radiative transition, whose depopulation frequency is about hundred times larger than that of the electron collision processes. On the other hand, 4d$[3/2]^o$ state depopulates both by radiation and by electron collisions, which gives rise to the remarkable density-ratio dependence on N_e.

References

1. H. Akatsuka; Abstract of the 10th Asian-European International Conf. on Plasma Surface Eng. (AEPSE2015), p. 94 (2015).
2. H. Akatsuka; Proc. 2015 Annual Conf. Fundamentals and Materials Society IEE Japan, p. 219 (2015).
3. H. Akatsuka, E. Tanaka, K. Ando, A. Nezu, D. Kuwahara, S.Shinohara; Proc. Int. Symp. Dry Process, pp. 95-96 (2015).

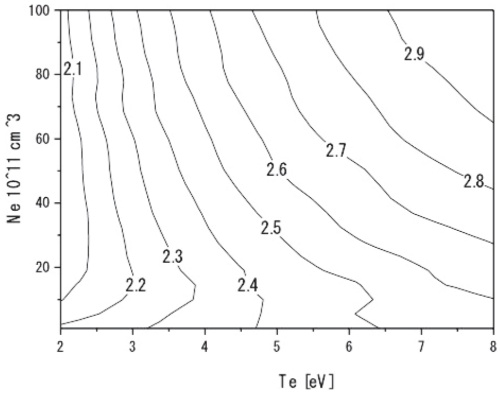

Fig. 1. Contour diagram of the number density ratio of the excited states (4p'$[1/2]_0$)/(4p$[1/2]_0$) calculated for parameters plasma radius R = 10 cm, the gas temperature T_g = 500 K, and the discharge pressure P = 7 mTorr, scanned over the range $2 \leq T_e$ [eV] ≤ 8 and N_e [cm^{-3}] $\leq 10^{13}$.

III. Co-operative Researches

III. Co-operative Researches

III.1 Co-operative Researches within Tokyo Institute of Technology

- Development of an Electromagnetic Shock Tube for Production of Dissociated Atomic Hydrogen Targets for Heavy-Ion Interaction Experiments, Department of Energy Sciences, Interdisciplinary Graduate School of Science and Engineering.

- Fundamental research on remote cutting and size-reduction of nuclear fuel debris immersed in water by arc discharge plasma, School of Materials and Chemical Technology

III.2 Co-operative Researches with Outside of Tokyo Institute of Technology

- n_TOF Collaboration
  CERN

- Advanced Research and Education Program for Nuclear Decommissioning, Ministry of Education ,Culture Sports, Science and Technology-Japan, Tokyo Medical and Dental University, Tokai University, Tokyo City University, Shibaura Institute of Technology

- Criticality Accident Analysis of Meltdown Core, JSPS KAKENHI (Grant-in-Aid for Challenging Exploratory Research)

- High-Temperature Solar Thermal Energy Recovery, Cross-ministerial Strategic Innovation Promotion Program (SIP), Cabinet Office, Government of Japan, 2014-2019.

- Thermochemical Energy Storage for Waste Heat Utilization at Medium Temperatures, JSPS Grant-in-Aid for Scientific Research (B), 2012-2015.

- Solid Oxide Electrolysis Cell Development, JSPS Grant-in-Aid for Challenging Exploratory Research, 2015-2016.

- “Structure Evaluation of Carbon Composite for Battery”, Cooperative Research of RLNR, 2015-01, 2015.

- Experimental study on fabrication of Pb-Li alloys and impurity control, National Institute for Quantum and Radiological Science and Technology, Kyoto university

- Waste management scenario in the hot cell and waste storage for DEMO, National Institute for Quantum and Radiological Science and Technology, Toyama university, Fukui university

- Experimental study on chemical behavior and compatibility of Pb-Bi at composition changing
  Japan atomic energy agency

- Control of heat and hydrogen transfer by improvement of interface structure in heat exchanger of fusion blanket
  National Institute for Fusion Science
  Tokai university

- IAEA Coordinated Research Project: “Pathways to energy from Inertial Fusion: Materials beyond ignition”
  International Atomic Energy Agency
  Osaka university

- Fundamental Study on Simple Reprocessing Method for Spent Thorium Fuels by Using Uranium-Selective Precipitant, Entrusted Research Project, The Center of World Intelligence Project for Nuclear S&T and Human Resource Development, JST, MEXT, Japan.

- Feasibility Study on Dissolution of Vitrified Wastes by Molten Salts (1), Entrusted Research Project, Reduction and Resource Recycling of High-level Radioactive Wastes through Nuclear Transmutation, ImPACT Program of Council for Science, Technology and Innovation, Cabinet Office, Government of Japan.

- Development of Microwave-Driven Rapid Extraction of Platinum Group Metals, Grant for Young Researcher, JGC-S Scholarship Foundation.

- Thermal and Radiolytic Decomposition of Ion Exchange Resin, Entrusted Research Project CERES, Inc., CRIEPI.

- Study on Low-Cost Process of SiC/SiC Composites: Japan Aerospace Exploration Agency (JAXA)

- Study on Properties of B4C Neutron-Absorbing Materials for Control Rods: Japan Atomic Energy Agency (JAEA)

- Study on Neutron-Irradiation Resistance of Orientation-Controlled Ceramics: National Institute for Materials Science (NIMS)

- Sinterability of SiC Ceramics with Al4SiC4 Addition and Their Properties: National Institute for Materials Science (NIMS)

- Study on the Evaluation of Thermal Shock Fracture Behavior of Ceramics: Tokyo Metropolitan University

- Research on Formation and Characterization of Oxide Nanopowder: Vinca Institute, University of Belgrade, Serbia

- Development of Porous Ceramics using Natural Minerals for Adsorption and Immobilization of

Radioactive Nuclides: Silica Material LLC.

- Fundamental Study on Plasma Resistance of Rare-Earth Fluoride Ceramics: Nippon Yttrium Co., Ltd.

- Development of Interphase Formation Process of High-Performance Ceramics-Based Composites Based on Electrochemical Approach, Grant-in Aid for Scientific Research (C), Japan Society for the Promotion of Science

- Astrobiology Experiments Based on MeV Ion Beams, Division of Materials Science and Chemical Engineering, Faculty of Engineering, Yokohama National University.

- Development of Negative Ion Sources for Tandem Accelerators, Atomic Energy Research Laboratory, Tokyo City University.

- Selective Irradiation of Cancer Cells by Electrons Emitted from Cancer-Localizing Drugs, Grant-in-Aid for Scientific Research (B), Japan Society for the Promotion of Science.

- Pyrochemical Treatment of Nuclear Fuel Debris Using Selective Fluorination and Molten Salt Electrolysis, Tokyo City University, Tohoku University

- Plasma Spectroscopy of Argon and Helium Helicon Plasmas for Thruster of Artificial Satellites, Tokyo University of Agriculture and Technology, Shinshu University, National Institute for Fusion Science

- Observation of Optical Emission Spectroscopy in Atmospheric-pressure Plasma Jet, University of Miyazaki.

- Local Structure of Zirconium Cation in Various Fluorides Melts, Tokyo City University, Centre National de la Recherche Scientifique (CNRS, France).

- Production Efficiency of RONS in Plasma Activated Water by Using Micro-sized Atmospheric-Pressure Plasma Jet, Kochi University of Technology

- Time-resolved Optical Emission Spectroscopic Measurement of Pulsed Discharge Plasmas and their Atomic and Molecular Processes, Grant-in-Aid for Scientific Research (B), Japan Society for the Promotion of Science

- Nitrogen Divertor Plasma where Non-equilibrium Characteristics are Actively Applied from the Viewpoint of Atomic and Molecular Processes, Grant-in-Aid for Challenging Exploratory Research, Japan Society for the Promotion of Science

- Spectroscopic Analysis of Low-Pressure Discharge Argon Plasma, Cannon Inc.

- 3S Features of High Temperature Gas Cooled Reactors: RLNR Coop. Research, Japan Atomic Energy Agency.

- Development of Nuclear Waste Categorization System by gamma spectrometry; Japan Atomic Energy Agency

- Regulation of DNA Repair and Cell Death through Phosphorylation of DNA Repair Proteins, Kanazawa Medical University

- Prediction of Radiation Sensitivity And Cancer Susceptibility Using A Newly Generated Phosphorylation-specific Antibody, Sapporo Medical University

- Mechanisms of DNA double-strand break repair through non-homologous end joining, Kyoto University

- Molecular mechanisms of neutron-induced DNA damage and its repair, Kinki University

- Common molecular mechanisms of repair of radiation-induced DNA damage and immunoglobulin class switch recombination, Karolinska Institute, Sweden

- Role of LIG4 in Wnt signaling-induced radioresistance, University of Texas, MD Anderson Cancer Center, TX, USA

- Development of Removal Process of Platinum Group Metals for Quality Improvement and Decrease of Generation Amount of Vitrified Object, Japan Science and Technology Agency (JST).

- Advanced Research and Education Program for Nuclear Decommissioning, Japan Science and Technology Agency (JST).

- Vitrification Test Related with Composition Change of Waste Component (Evaluation of High Loading Glass Based on New Combinatorial Method), Japan Nuclear Fuel Limited.

- Basic Studies for Developing Rational Treatment and Disposal System of Radioactive Wastes Generated by Fukushima Nuclear Reactor Accident, Grant-in-Aid for Scientific Research (S), Japan Society for the Promotion of Science (JSPS).

- Development of Taylor Vortex Centrifugal Extractor for Liquid-liquid / Solid-liquid Nuclide Separation Process, Grant-in-Aid for Scientific Research (B), Japan Society for the Promotion of Science (JSPS).

- Development of New Separation Technique of Radioactive Cesium from Contamimnated Soil Using Agricultural and Waste Based Biomass, Grant-in-Aid for Young Scientists (B), Japan Society for the Promotion of Science (JSPS).

- Development of Absorbents for Decontamination of Radioactive Nuclides such as Cesium, Nitto Denko Corporation.

- Development of Vitrification Method Containing Oxidated PBN for Final Disposal and Evaluation of Vitrification Ability and Safety of Cesium, Mitsubishi Chemical Engineering Corporation.

- Evaluation of Exposure Dose on Overpack and High Content Vitrified Waste of HLLW, Radioactive Waste Management Funding and Research Center.

IV. List of Publications

IV. List of Publications

C. Weiss, Tatsuya Katabuchi (64th author), n_TOF Collaboration (132 authors). The new vertical neutron beamline at the CERN n_TOF facility design and outlook on the performance, Nuclear Instruments and Methods in Physics Research Section A: Accelerators, Spectrometers, Detectors and Associated Equipment, Vol. 799, pp. 90-98, (2015).

Kimura Atsushi, Harada Hideo, Shoji, Iwamoto Osamu, Toh Yosuke, Koizumi Mitsuo, Kitatani Fumito, Furutaka Kazuyoshi, Igashira Masayuki, Katabuchi Tatsuya, Mizumoto Motoharu, Hori Jun-ichi, Kino Koichi, Kiyanagi Yoshiaki. Current activities and future plans for nuclear data measurements at J-PARC, European Physical Journal A, Vol. 51, (2015).

Tatsuya Katabuchi, Shotaro Yanagida, Kazushi Terada, Nobuyuki Iwamoto, Masayuki Igashira: Neutron capture cross section and capture gamma-ray spectra of 138Ba in the keV-neutron energy region; Fifteenth International Symposium on Capture Gamma-Ray Spectroscopy and Related Topics (CGS15), Dresden, Germany, Aug. 25-29, 2014, EPJ Web of Conferences Vol. 93 (2015).

Jun-ichi Hori, Hiroshi Yashima, Shoji Nakamura, Kazuyoshi Furutaka, Kaoru Hara, Hideo Harada, Kentaro Hirose, Masayuki Igashira, Tatsuya Katabuchi, Atsushi Kimura, Koichi Kino, Fumito Kitatani, Yoshiaki Kiyanagi, Mitsuo Koizumi, Motoharu Mizumoto, Tadafumi Sano, Yoshiyuki Takahashi, Yosuke Toh: Neutron Capture Cross Section Measurement on 91Zr at J-PARC/MLF/ANNRI; Fifteenth International Symposium on Capture Gamma-Ray Spectroscopy and Related Topics (CGS15), Dresden, Germany, Aug. 25-29, 2014, EPJ Web of Conferences Vol. 93 (2015).

Hideo Harada, Osamu Iwamoto, Nobuyuki Iwamoto, Atsushi Kimura, Kazushi Terada, Taro Nakao, Shoji Nakamura, Kazuhito Mizuyama, Masayuki Igashira, Tatsuya Katabuchi, Tadafumi Sano, Yoshiyuki Takahashi, Koichi Takamiya, Cheol Ho Pyeon, Satoshi Fukutani, Toshiyuki Fujii, Jun-ichi Hori, Takahiro Yagi, Hiroshi Yashima: Accuracy improvement of neutron nuclear data on minor actinides; Fifteenth International Symposium on Capture Gamma-Ray Spectroscopy and Related Topics (CGS15), Dresden, Germany, Aug. 25-29, 2014, EPJ Web of Conferences Vol. 93 (2015).

Tatsuya Katabuchi, Tomohiro Okamiya, Shotaro Yanagida, Motoharu Mizumoto, Kazushi Terada, Atsushi Kimura, Nobuyuki Iwamoto, Masayuki Igashira. Neutron capture cross section and capture gamma-ray spectra of 89Y, Fifth international workshop on Compound-Nuclear Reactions and Related Topics (CNR*15), Tokyo, Japan, Oct. 2015.

Saito Tatsuhiro, Tatsuya Katabuchi, Tomohiro Okamiya, Shotaro Yanagida, Brian Hales, Masayuki Igashira. Measurement of Gamma-Ray Spectra from a Proton-Lithium Neutron Source for Boron Neutron Capture Therapy, 15th International Congress of Radiation Research (ICRR 2015), Kyoto, Japan, May. 2015.

Tatsuya Katabuchi, Masayuki Igashira, Motoharu Mizumoto, Kazushi Terada, Atsushi Kimura, Shoji Nakamura, Taro Nakao, Hideo Harada, Jun-Ichi Hori, Koichi Kino, Yoshiaki Kiyanagi, Measurement of Neutron Capture Cross Section of Tc-99 using ANNRI-NaI(Tl) Spectrometer at J-PARC, 2015 Fall Meeting of the Atomic Energy Society of Japan, Sep. 9-11, 2015, O02.

Seigo Umezawa, Masayuki Igashira, Tatsuya Katabuchi, Yanagida Shotaro, Tomohiro Okamiya, Measurement of the keV-Neutron Capture Cross Sections and Gamma-ray Spectra of Cs-133 and I-127, 2015 Fall Meeting of the Atomic Energy Society of Japan, Sep. 9-11, 2015, O01.

Atsushi Kimura, Shoji Nakamura, Kazushi Terada, Taro Nakao, Yosuke Toh, Hideo Harada, Tatsuya Katabuchi, Motoharu Mizumoto, Masayuki Igashira, 芝原雄司, Koichi Takamiya, Satoshi Fukutani, Toshiyuki Fujii, Jun-Ichi Hori, Measurement of neutron capture cross section of Gd-155 and 157 with the NaI(Tl) spectrometer in J-PARC/MLF/ANNRI, 2015 Fall Meeting of the Atomic Energy Society of Japan, Sep. 9-11, 2015, O03.

Tatsuhiro Saito, Masayuki Igashira, Tatsuya Katabuchi, Yanagida Shotaro, Seigo Umezawa, Measurement of gamma-ray spectra from proton-Lithium nuclear reactions for development of a BNCT neutron source, 2015 Fall Meeting of the Atomic Energy Society of Japan, Sep. 9-11, 2015, P33.

Takeshi Nagasaka, Masayuki Igashira, Tatsuya Katabuchi, Tatsuhiro Saito, Seigo Umezawa, Ryo Fujioka, Measurement of the 550 keV-Neutron Capture Cross Section and Gamma-ray Spectra of Y-89, 2016 Annual Meeting of the Atomic Energy Society of Japan, Mar. 26-28, 2016, 2J01.

Noriak Nakao, Kazuaki Kosako, Noriyosu Hayashizaki, Tatsuya Katabuchi, Tooru Kobayashi, Monte Carlo analyses of shielding, activation and external exposure for BNCT using near-threshold 7Li(p,n) neutrons, 2016 Annual Meeting of the Atomic Energy Society of Japan, Mar. 26-28, 2016, 1K03.

Taro Nakao, Atsushi Kimura, Kazushi Terada, Syoji Nakamura, Osamu Iwamoto, Hideo Harada, Tatsuya Katabuchi, Masayuki Igashira, Jun-Ichi Hori, Developments of new data acquisition system in J-PARC/MLF/ANNRI, 2016 Annual Meeting of the Atomic Energy Society of Japan, Mar. 26-28, 2016, 2J03.

Odmaa Sambuu, Toru Obara: Neutronic and thermo-hydraulic analyses of a small, long-life HTGR for passive decay-heat removal; Journal of Nuclear Science and Technology, Vol. 52, No. 12, pp. 1519-1529 (2015).

Odmaa Sambuu, Toru Obara: Impact of power density profile on passive decay-heat removal in prismatic HTGR; Annals of Nuclear Energy, Vol. 87, pp. 23-29 (2015).

Topan Setiadipura, Toru Obara: Optimization of Start-up Fuel Management for OTTO Cycle Pebble Bed Reactor; Energy Procedia, Vol. 71, pp. 42-51 (2015).

Piyatida Trinuruk, Toru Obara: Particle-type Burnable Poisons for Thorium-based Fuel in HTGR; Energy Procedia, Vol. 71, pp. 22-32 (2015).

Haruka Kikuchi, Toru Obara: Kinetic Behavior in Criticality Accident of Two Fuel Solution Tanks; Progress in Nuclear Energy, Vol. 82, pp. 96-101 (2015).

Odmaa Sambuu, Toru Obara: Comparative study on HTGR Designs for Passive Decay Heat Removal; Progress in Nuclear Energy, Vol. 82, pp. 37-45 (2015).

Takuya Umano, Keinich Yoshioka, Toru Obara: Application of the “best representativity” method to a PWR fuel calculation using the critical experiments at the Toshiba NCA facility; Annals of Nuclear Energy, Vol. 85, pp. 78-92 (2015).

Odmaa Sambuu, Toru Obara: Above-ground HTGR design for passive decay heat removal; Journal of Nuclear Science and Technology, Vol. 52, No. 6, 857-871 (2015)

Hai Quan Ho, Toru Obara: Burnup performance of OTTO cycle pebble bed reactors with ROX fuel; Annals of Nuclear Energy, Vol. 83, pp. 1-7 (2015).

Julia Abdul Karim, Jun Nishiyama, Toru Obara: Application of the Melt and Refining Procedure to the CANDLE Reactor Concept; Transactions of the American Nuclear Society, Vol. 113, pp. 924-926 (2015). Washington D.C., November 8-12, 2015.

Hai Quan Ho, Toru Obara: Composition of ROX Fuel for High-Burnup Pebble Bed Reactor; Transactions of the American Nuclear Society, Vol. 113, pp. 922-923 (2015). Washington D.C., November 8-12, 2015.

Irwan Liapto Simanullang, Toru Obara: Burnup Analysis of Accumulative Fuel Loading Scheme Pebble Bed Reactor with Optimum Fuel Composition; Transactions of the American Nuclear Society, Vol. 113, pp. 919-921 (2015). Washington D.C., November 8-12, 2015.

Delgersaikhan Tuya, Toru Obara, Hiroki Takezawa: Kinetic Analysis of Weakly Coupled Fuel Debris by Integral Kinetic Model; Transactions of the American Nuclear Society, Vol. 113, pp. 1158-1160 (2015). Washington D.C., November 8-12, 2015.

Toru Obara, Delgersaikhan Tuya, Hiroki Takezawa: Fission Probability Density Functions for Kinetic Analysis in Weakly Coupled Fuel Debris; Transactions of the American Nuclear Society, Vol. 113, pp. 1150-1152 (2015). Washington D.C., November 8-12, 2015.

Toru Obara, Hiroki Takezawa, Delgersaikhan Tuya: PROMPT SUPERCRITICAL KINETIC ANALYSIS WITH NEUTRON COUPLING BETWEEN FUEL DEBRIS; Proceedings of International Conference on Nuclear Criticality Safety (ICNC2015), Charlotte, North Carolina, USA, September 13-17, 2015, pp. 1431-1438 (2015).

Toru Obara, Delgersaikhan Tuya, Haruka Kikuchi: Fission Probability Density Functions for Super Prompt Criticality Accident Analysis in Weakly Coupled Systems by Integral Kinetic Model; Proceedings of ICONE-23, 23th International Conference on Nuclear Engineering, ICONE23-1618, May 17-21, 2015, Chiba, Japan, on CD-ROM (2015).

Delgersaikhan Tuya, Haruka Kikuchi, Toru Obara: Application of Integral Kinetic Model to Transient Analysis of Different Types of Weakly Coupled Systems; Proceedings of ICONE-23, 23th International Conference on Nuclear Engineering, ICONE23-1626, May 17-21, 2015, Chiba, Japan, on CD-ROM (2015).

Odmaa Sambuu, Toru Obara: CORE TEMPERATURE COEFFICIENT OF SMALL LONG-LIFE HTGR FOR PASSIVE DECAY-HEAT REMOVAL; Proceedings of ICONE-23, 23th International Conference on Nuclear Engineering, ICONE23-1625, May 17-21, 2015, Chiba, Japan, on CD-ROM (2015).

Irwan Liapt Simanullang, Toru Obara: IMPROVEMENT OF BURNUP ANALYSIS FOR PEBBLE BED REACTORS WITHANACCUMULATIVE FUEL LOADING SCHEME; Proceedings of ICONE-23, 23th International Conference on Nuclear Engineering, ICONE23-1627, May 17-21, 2015, Chiba, Japan, on CD-ROM (2015).

Hai Quan Ho, Toru Obara: IMPACT ON BURNUP PERFORMANCE OF COATED PARTICLE FUEL DESIGN IN PEBBLE BED REACTOR WITH ROX FUEL; Proceedings of ICONE-23, 23th International Conference on Nuclear Engineering, ICONE23-1651, May 17-21, 2015, Chiba, Japan, on CD-ROM (2015).

Delgersaikhan Tuya, Hiroki Takezawa, Toru Obara: Statistical Uncertainty in Kinetic Analysis using Integral Kinetic Model for Re-criticality Accident in Weakly-Coupled Fuel Debris; Proc. of 2016 annual meeting of Atomic Energy Society of Japan, 1O13 (2016).

Hiroki Takezawa, Toru Obara: A Method for Passive Reduction in Criticality of Fuel Debris Dust; Proc. of 2016 annual meeting of Atomic Energy Society of Japan, 3E07

(2016).

Irwan Liapto Simanullang, Toru Obara: Optimization of initial fuel composition for Small Pebble Bed Reactor with accumulative fuel loading scheme; (2) Use of burnable poison; Proc. of 2016 annual meeting of Atomic Energy Society of Japan, 3O10 (2016).

Hai Ho Quan, Toru Obara: OTTO cycle Small Pebble Bed Reactor with Rock-like fuel elements; (4)Burnup performance in molten salt coolant; Proc. of 2016 annual meeting of Atomic Energy Society of Japan, 3O11 (2016).

Julia Abdul Karim, Jun Nishiyama, Toru Obara: Application of Melt Refining of Metal Fuel to CANDLE Reactor; (3)Effects of Cooling Time during Melt and Refining Procedures; Proc. of 2016 annual meeting of Atomic Energy Society of Japan, 3O12 (2016).

Hiroki Osato, Jun Nishiyama, Toru Obara: Study on CANDLE Burning Reactor with Initial Core Using Plutonium from LWR Spent Fuel; Proc. of 2016 annual meeting of Atomic Energy Society of Japan, 3O13 (2016).

Toru Obara, Dwi Irwanto, Tomonori Nakashima, Taiki Onoe, Piyatida Trinuruk, Topan Setiadipura, Sambuu Odmaa, Hai Quan Ho, Irwan Liapto Simanullang:Design Concept Study for Innovative High Temperature Gas-Cooled Reactors; Proceedings of the Reactor Physics Asia 2015 (RPHA15) Conference, Jeju, Korea, Sept. 16-18, 2015, 12DAIR2-1 (2015).

Van Khanh Hoang, Toru Obara: Effects of Neutron Spectrum Shift on Burnup Performance of a Breed and Burn Reactor; Proc. of 2015 autumn meeting of Atomic Energy Society of Japan, D28 (2015).

Odmaa Sambuu, Toru Obara: Comparison on design parameter criteria of prismatic HTGR and PBR for passive decay heat removal; Proc. of 2016 annual meeting of Atomic Energy Society of Japan, D25 (2015).

Hai Quan Ho, Toru Obara: OTTO cycle Small Pebble Bed Reactor with Rock-like fuel elements (3) Optimization of the core parameters and analysis of temperature coefficient; Proc. of 2015 autumn meeting of Atomic Energy Society of Japan, D24 (2015).

Irwan Liapto SIMANULLANG, Toru OBARA: Optimization of Initial Fuel Composition for Small Pebble Bed Reactor with Accumulative Fuel Loading Scheme (1)Reduction of Fuel Enrichment; Proc. of 2015 autumn meeting of Atomic Energy Society of Japan, D23 (2015).

Julia ABDULKARIM, Jun NISHIYAMA, Toru OBARA, “Application of Melt Refining of Metal Fuel to CANDLE Reactor (2) Effects of noble and reactive fission gasses removal to the burnup performance; Proc. of 2015 autumn meeting of Atomic Energy Society of Japan, D21 (2015).

Delgersaikhan Tuya, Toru Obara: Kinetic Analysis of Re-criticality Accident in Simplified System of Fuel Debris and Consolidated Fuel; Proc. of 2015 autumn meeting of Atomic Energy Society of Japan, A22 (2015).

Arnoldus Lambertus Dipu, Yutaka Ujisawa, Junichi Ryu, Yukitaka Kato: Electrolysis of carbon dioxide for carbon monoxide production in a tubular solid oxide electrolysis cell; Annals of Nuclear Energy, 81, pp. 257-262 (2015).

E. Mastronardo, L. Bonaccorsi, Y. Kato, E. Piperopoulosa, M. Lanza, C. Milone: Thermochemical performance of carbon nanotubes based hybrid materials for MgO/H2O/Mg(OH)2 chemical heat pumps; Applied Energy, 181, pp. 232-243 (2016).

S. T. Kim, M. Zamengo, J. Ryu, Y. Kato: Kinetic Characterization of Expanded Graphite, Calcium Chloride, and Magnesium Hydroxide Composite for the Chemical Heat Pump; Heat Transfer Research, 46(2), pp. 91-107 (2015).

Yukitaka Kato, Yutaka Ujisawa, Hiroshi Sakai, Takanobu Inada: Application of Carbon Recycling Iron-making System in a Shaft Furnace; ISIJ Int’l, 55(2), pp. 359–364 (2015).

Gentaro Fujii, Junichi Ryu, Katsumi Yoshida, Toyohiko Yano, Yukitaka KATO: Possibility of Application of Solid Oxide Electrolysis Cell on a Smart Iron-making Process Based on an Active Carbon Recycling Energy System (iACRES); ISIJ Int’l, 55(2), pp. 387-391 (2015).

Jun Kariya, Junicihi Ryu, Yukitaka Kato: Reaction Performance of Calcium Hydroxide and Expanded Graphite Composites for Chemical Heat Storage Applications; ISIJ Int’l, 55(2), pp. 457-463 (2015).

Odtsetseg MYAGMARJAV, Junichi RYU, Yukitaka KATO: Waste Heat Recovery from Iron Production by using Magnesium Oxide/Water Chemical Heat Pump as Thermal Energy Storage; ISIJ Int’l, 55(2), pp. 464-472 (2015).

M. Zamengo, J. Ryu, Y. Kato: Numerical Analysis of Chemical Heat Storage Units for Waste Heat Recovery in Steel Making Processes; ISIJ Int’l, 55(2), pp. 473-482 (2015).

Y. Kato: Contribution of Nuclear Energy on New Energy Systems Post Fukushima; Prog. Nuc. Eng., 82, pp. 53-57 (2015).

O. MYAGMARJAV, J. RYU, Y. KATO: Dehydration Kinetic Study of a Chemical Heat Storage Material with Lithium Bromide for a Magnesium Oxide/Water Chemical Heat Pump; Prog. Nuc. Eng., 82, pp. 153-158 (2015).

M. Zamengo, J. Ryu, Y. Kato: Chemical heat storage of thermal energy from a nuclear reactor by using a magnesium hydroxide/expanded graphite composite material; Energy Proceedure, 71, pp.293-305 (2015).

S. Saito, Y. Matsumura, Y. Kato, Japan Patent, No. 5852501, 11 December, 2015.

Odtsetseg Myagmarjav and Yukitaka Kato: Development of Chemical Heat Storage Material for a Combined System with Load-following Nuclear Power Plant; THE 3rd JAPAN-CHINA ACADEMIC SYMPOSIUM ON NUCLEAR FUEL CYCLE (ASNFC 2015), 4 Dec, 2015, Tokyo.

Y. Kato, (Invited Lecture): Thermochemical energy storage for waste heat recoveries and utilizations; World Engineering Conference and Convention (WECC2015), OS 2-4-5, 1 December, 2015, Kyoto.

Massimiliano ZAMENGO, Junichi RYU, Keiko FUJIOKA, Junko MORIKAWA, Yukitaka KATO: Compacted block of magnesium hydroxide – expanded graphite for heat storage/output enhancement in thermochemical energy storage systems; Sorption Friends' Meeting, 15 September, 2015, Milazzo, Italy.

Jun Kariya, Junichi Ryu, Yukitaka Kato: Reaction Performance of Calcium Hydroxide and Vermiculite Composite for Chemical Heat Storage Application; Proc. of The 13th International Conference on Energy Storage (GREENSTOCK 2015), 19 May, 2015, Beijing, P. R. China.

Y. Kato: Evaluation of Carbon Recycling Energy Process Driven by Nuclear Power; ANS National Meeting, 2015 Winter, 11 November, 2015, Washington DC, USA.

T. Terauchi, H. Iguchi, J. Kariya, K. Fujioka, Y. Kato: Change in the hydration reactivity of calcium chloride by support composite; SCEJ 81st Annual Meeting, ZA359, 15 March, 2016, Kansai University, Osaka.

T. Terauchi, Y. Kato: Change in the hydration of calcium chloride by mixing with expanded graphite; JSME ICMS 2015 Winter Meeting, 5 Nov., 2015, Tokyo Tech.

Y. Kato: Passivity of Heat Utilization by Thermochemical Energy Storage; 2015 Japan Refrigeration and Air Conditioning Society Annual Meeting, C325, 23 (20-23) October, 2015, Tokyo,

Kaoruko Yamamoto, Yukitaka Kato, Junichi Ryu: Dehydration kinetics of composite hydroxide material made from mechano-cehmical method; SCEJ 47th Autumun Meeting, M314, 11 September, 2015, Sapporo.

J. Kariya, J. Ryu, Y. Kato: Development of CaO/H2 thermochemical energy storage material; Japan Heat Transfer Sympodium, C133, 3 June, 2015, Fukuoka

Y. Kato, (Invited Lecture): Contribution of Carbon Recycling technology on Low-Carbon Society; 28th Environmental Engineering Union Meeting, 15 May, 2015, Tokyo.

Yun Gao, Minoru Takahashi, Masao Nomura: Experimental Study on Diffusion of Ni in Lead-bismuth Eutectic (LBE); Energy Procedia, Vol. 71 (2015) pp.313–319.

Minoru Takahashi, Mihail Mihalache, Radu Secareanu, Alexandre Chapelat: Fundamental Study on Heavy Metal Freezing Behavior for Stop of Water Leakage from LWR Containment Vessel; Progress in Nuclear Energy, Vol. 82, pp.184-190, 2015.

Dan Tri Le, Minoru Takahashi: Improvement of Critical Heat Flux Performance by Wire Spacer; Journal of Energy and Power Engineering, Vol.9, No.10, pp.844-851, 2015, doi:10.17265/1934-8975/2015.010.002.

Yun Gao, Minoru Takahashi, Masao Nomura: Characteristics of Iron and Nickel Diffusion in Molten Lead-bismuth Eutectic; Mechanical Eng. J., Vol. 2, No.6 (2015), [DOI: 10.1299/mej.15-00149].

Tri Dan Le, Noriaki Inaba, Minoru Takahashi: Critical Heat Flux Behavior of Heater Pin with and Without Wire spacer in Boiling Two-Phase Flow; The 23nd International Conference on Nuclear Engineering (ICONE23), May 17-21, 2015, Chiba, Japan. ICONE23-1728.

Pribadi Mumpuni Adhi, Minoru Takahashi: Parametric Study on Electromotive Force of Oxygen Sensor in Lead-Bismuth Eutectic; The 23nd International Conference on Nuclear Engineering (ICONE23), May 17-21, 2015, Chiba, Japan. ICONE23-1951.

Minoru Takahashi: Comparison of Innovative Direct Contact Type LFR with Conventional LFR and SFR; The 23nd International Conference on Nuclear Engineering (ICONE23), May 17-21, 2015, Chiba, Japan. ICONE23-1862.

Yun Gao, Minoru Takahashi, Carlo Cavallotti, Guido Raos: Molecular dynamics of liquid metal alloys for Generation IV nuclear reactor; MOLSIMENG meeting, Millan, 18 September 2015.

Le Tri Dan, Noriaki Inaba, Minoru Takahashi: Experimental Study on Critical Heat Flux Behavior in Single Fuel Pin with and without Wire Spacer; 11th National Conference on Nuclear Science and Technology, VINANST 11 (http://vinanst11.vinatom.gov.vn/en/), Danang, Vietnam, August 5-7, 2015.

Radu Secareanu, Minoru Takahashi, Riccardo Mereuc, Ilie Prisecarua: Breakup and Solidification Behaviour of Liquid Metal Jet in Water Environment; 24th International

Conference Nuclear Energy for New Europe, Portoroz, Slovenia, September 14-17, 2015.
Yun Gao, Minoru Takahashi, Masao Nomura, and Takashi Nozawa: Characteristics of Nickel and Iron Diffusion in Molten Pb-17Li Alloy; 12th International Symposium on Fusion Nuclear Technology, ISFNT-12, P1.095, Jeju Island, Korea, September 14-18, 2015.

Tri Dan Le, Noriaki Inaba, Minoru Takahashi: Critical Heat Flux in Triangular Pin Bundle with and without Wire Spacer; 2015 Annual Meeting of AESJ, March 20-22, 2015, Ibaraki, Japan, I41.

Yun Gao, Takashi Nozawa, Changho Park, Tatsuya Suzuki, Minoru Takahashi, Masao Nomura: Characteristics of Metal Diffusion in Lead-lithium Alloy in a Capillary Tube; 2015 Annual Meeting of AESJ, Ibaraki, Japan, March 20-22, 2015, F24.

Masamichi Nakagawa, Minoru Takahashi, Toru Kobayashi, Masanori Aritomi: Linear Stability Analysis of High-speed Lithium Film Flows for the Neutron Source in Boron Neutron Capture Therapy (BNCT); 2015 Annual Meeting of Japan Society of Mechanical Engineers, Sapporo, Hokkaido, Japan, September 13-16, 2015.

Masatoshi KONDO, Yuu Nakajima, Mitsuyo Tsuji, Takashi Nozawa: Evaluation of thermal conductivity for liquid lead lithium alloys at various Li concentrations based on measurement and evaluation of density, thermal diffusivity and specific heat of alloys; Fusion Engineering and Design, Vol. 109-111, Part B, pp. 1345-1350, 2015.

Yuu Nakajima, Masatoshi KONDO, Takashi Nozawa: Study on fabrication method of lithium alloys with metal grains; Fusion Engineering and Design, Vol. 98-99, pp. 2009-2014, 2015.

Masatoshi Kondo, Masaomi Ishii, Takeo Muroga. Corrosion of steels in molten gallium (Ga), tin (Sn) and tin lithium alloy (Sn–20Li); Fusion Engineering and Design, Vol. 98-99, pp. 2003-2008, 2015.

Masatoshi KONDO, Yoshimitsu Hishinuma, Takeo Muroga: Experimental study on compatibility of reduced activation ferritic martensitic steel with flowing Pb-17Li (2) Discussions on mechanism of corrosion erosion based on results of metallurgical analysis; 2016 Annual Meeting of Atomic Energy Society of Japan, Sendai, March 26-28, 2016, 3L04.

Park ChangHo, Masatoshi Kondo, Takahshi Nozawa, Hitoyasu TANIGAWA: Study on Quantity Fabrication and Purity Control of Lithium-lead as Fusion Liquid Breeder; 2016 Annual Meeting of Atomic Energy Society of Japan, Sendai, March 26-28, 2016, 3L03.

Pribadi Adhi, Masatoshi Kondo, Minoru Takahashi: Performance of solid electrolyte oxygen sensor with solid Fe/Fe_3O_4 reference electrode for liquid lead-bismuth eutectic; 2016 Annual Meeting of Atomic Energy Society of Japan, Sendai, March 26-28, 2016, 1H07.

Masatoshi Kondo, Masatomi Ishi, Takeo Muroga: Experimental study on compatibility of reduced activation ferritic martensitic steel with flowing Pb-17Li: Effect of flowing conditions and temperature gradient; 2016 Annual Meeting of Atomic Energy Society of Japan, Shizuoka, September 9-11, 2015, N17.

Masatoshi KONDO: It's liquid but not water –current status and issues of the next generation blanket and divertor R&D; 32the of the annual meeting of the Japan Society of Plasma Science and Nuclear Fusion Research, Nagoya, Japan, November 24-27, 2015, S5-5.

K. Takao, K. Arakawa, T. Mori, M. Harada, Y. Ikeda: Outer-Sphere Extraction of Uranyl(VI) from HNO3(aq) to 1-Butyl-3-methylimidazolium Nonafluorobutanesulfonate Ionic Liquid −Towards Decontamination of Uranium Wastes−; Bulletin of Chemical Society of Japan, Vol.88, pp.1746-1751 (2015).

T. Suzuki, K. Takao, T. Kawasaki, M. Harada, M. Nogami, Y. Ikeda: Correlation between Intermolecular Hydrogen Bonds and Melting Points of Uranyl Nitrate Complexes with Cyclic Urea Derivatives; Polyhedron, Vol.96, pp.102-106 (2015).

T. Mori, K. Takao, K. Sasaki, T. Suzuki, T. Arai, Y. Ikeda: Homogeneous Liquid-Liquid- Extraction of U(VI) from HNO3 Aqueous Solution to Betainium Bis(trifluoromethylsulfonyl)imide Ionic Liquid and Recovery of Extracted U(VI); Separation and Purification Technology, Vol.155, pp.133-138 (2015).

M. Nishikawa, S. Sawamura, A. Haraguchi, J. Morikubo, K. Takao, T. Tsubomura: Highly Emissive Copper(I) Complexes Bearing Diimine and Bis(diphenylphosphinomethyl)-2,2-dimethyl-1,3-dioxolane; Dalton Transactions, Vol.44, pp.411-418 (2015).

K. Takao, Y. Kawata, M. Nogami, M. Harada, Y. Morita, K. Nishimura, Y. Ikeda: Precise Determination of Precipitation Yield of Uranyl Nitrate with N-Alkylated 2-Pyrrolidone Derivatives; Journal of Nuclear Science and Technology, Vol.52, pp.294-298 (2015).

H. Sagara, M. Katayama, K. Takao, C.-Y. Han, M. Saito: Challenges of Nuclear Security Educational Course Establishment as a Graduate School Program In Tokyo Institute of Technology; The 3rd Japan-China Academic Symposium on Nuclear Fuel Cycle (ASNFC2015), December 2-5, 2015, Tokyo Japan.

K. Takao, K. Arakawa, T. Mori, M. Harada, Y. Ikeda: Studies on Extraction Behaviour of U(VI) to [bmim][NfO] Ionic Liquid and Its Recovery Using Hydrogen Peroxide;

First SACSESS International Workshop towards Safe and Optimized Separation Processes, A Challenge for Nuclear Scientists, April 22-24, 2015, Warsaw, Poland.

T. Mori, K. Takao, Y. Ikeda, T. Kawasaki: Fundamental Studies on Establishment of Rational Treatment and Disposal System for Radioactive Wastes Generated in Fukushima NPP Accident: (46) Dissolution Behavior of Uranium Oxides in Ionic Liquids; Annual Meeting of Atomic Energy Society of Japan, September, 2015, Shizuoka Univ. I05.

S. Ikeda, T. Mori, K. Takao, Y. Ikeda: Microwave-Assisted Homogeneous Liquid-Liquid Extraction of Platinum Group Elements Using Thermomorphic [Hbet][Tf2N] Ionic Liquid; Annual Meeting of Atomic Energy Society of Japan, September, 2015, Shizuoka Univ. E12.

K. Arakawa, K. Takao, M. Harada, Y. Ikeda: Study on Extraction and Recovery of Uranyl Ion Using [BMI][NfO] Ionic Liquid; Annual Meeting of Atomic Energy Society of Japan, March, 2015, Ibaraki Univ. D28.

K. Takao: Catalytic Activity of Lewis Acidic Uranyl(VI) Complex in Nucleophilic Acyl Substitution; The 65th Conference of Japan Society of Coordination Chemistry, September, 2015, Nara Women's Univ. 3Fb-04.

M. Saeki, D. Matsumura, T. Yomogida, T. Taguchi, T. Tsuji, S. Kusano, T. Miyazaki, K. Takao, H. Ohniwa, N. Nakajima: A XAFS Study on Effect of Addition of Molybdenum on Photo-induced formation of Palladium Fine Particles; Annual Meeting of Japan Society for Molecular Science, September 16-19, 2015, 1B02.

N. Kozai, S. Suzuki, N. Aoyagi, F. Sakamoto, T. Ohnuki: Radioactive Fallout Cesium in Sewage Sludge Ash Produced after the Fukushima Daiichi Nuclear Accident; Water Research, Vol. 68, 616-626 (2015).

T. Saito, T. Terashima, N. Aoyagi, S. Nagao, N. Fujitake, T. Ohnuki: Physicochemical and ion-binding propeties of highly aliphatic humic substances extracted from deep sedimentary groundwater; Environmental Science: Process & Impacts, Vol. 17, 1386-1395(2015).

M Kaneko, H. Iwata, H. Shiotsu, S. Masaki, Y. Kawamoto, Y. Nakamatsu, J. Imoto, G. Furuki, A. Ochiai, K. Nanba, T. Ohnuki, R.C. Ewing, S. Utsunomiya: Radioactive Cs in the severely contaminated soils near the Fukushima Daiichi Nuclear Power Plant; Frontiers in Energy Research, Vol. 3, 37(2015).

T. Ohnuki, F. Sakamoto, S. Yamasaki, N. Kozai, H. Shiotsu, S. Utsunomiya, N. Watanabe, T. Kozaki: Effect of minerals on accumulation of Cs by fungus Saccaromyces cerevisiae; J. Environ. Radioact. Vol. 144, 127-133(2015).

T. Ohnuki, M. Jiang, F. Sakamoto, N. Kozai, S. Yamasaki, Q. Yu, K. Tanaka, S. Utsunomiya, X. Xia, K. Yang, J. He: Sorption of trivalent cerium by a mixture of microbial cells and manganese oxides: Effect of microbial cells on the oxidation of trivalent cerium; Geochim. Cosmochim. Acta, Vol. 163, 1-13(2015).

Q. Yu, T. Ohnuki, K. Tanaka, N. Kozai, S. Yamasaki, F. Sakamoto, Y. Tani: Fungus-promoted transformation of lanthanides during the biooxidation of divalent manganese; Geochimica Cosmochimica Acta, Vol. 174, 1-12(2016).

Toshihiko Ohnuki, Fuminori Sakamoto, Nafumi Kozai, Kazuhiro Shiina, Kenji Tanaka, Jun Namekawa, Shinya Yamasaki: Remediation of Contaminated Forest by Spent Mushroom Bed; 5th East Asia Forum on Waste Management, Taichun, Taiwan, Oct. 25-28, 2015, S6-D3.

T. Ohnuki: Biogenic REEs nano particle formation and its mobilty in environments; Goldschmidt Conference 2015, Prague, Czhek, August 16-21, 2015, 2323.

T. Mullan, L. E. Macaskie, J. Hriljac, T. Ohnuki, S. Handley-Sidhu, The efficiency of calcium phosphate biominerals for the remediation of complex radioactive contaminated waters, Goldschmidt Conference 2015, Prague, Czhek, August 16-21, 2015, 2208.

T. kato, T. Ohonuki, T. Saito, Q. Yu: Sorption of Co2+ to biogenic Mn oxides produced by MnO4- reduction; Goldschmidt Conference 2015, Prague, Czhek, August 16-21, 2015, 1528.

T. Ohnuki, N. Kozai, F. Sakamoto, T. Saito, Q. Yu, M. Yamashita, T. Horiike,S. Utsunomiya, Coprecipitation of Radioactive Strontium in Sea Water during Formation of Biogenic Calcite, Migration 2015, Santa-Fe, USA, September 13-18, 2015, PB4-8.

T. Ohnuki, F. Sakamoto, N. Kozai, S. Yamasaki, Q. Yu, Accumulation of radioactive cesium in edible mushroom, The International Chemical Congress of Pacific Basin Scieties 2015, Honolulu, USA, December 15-20, 2015, 2289075.

T. Ohnuki, F. Sakamoto, N. Kozai, Developent of suppression materials against accumulation of radioactive cesium by edible mushroom, 2015 Fall Meeting of the Atomic Energy Society of Japan, Shizuoka, September 9-11, 2015, H40.

T. Kato, T. Ohnuki, T. Saito, Q. Yu, Elucidation of microbial reduction of permanganate, and absorption behavior of heavy metals, 2015 2016 Annual Meeting of the Atomic Energy Society of Japan, Shizuoka, September 9-11, 2015, 3A11.

Gentaro Fujii, Junichi Ryu, Katsumi Yoshida, Toyohiko Yano, Yukitaka Kato: Possibility of Application of Solid

Oxide Electrolysis Cell on a Smart Iron-making Process Based on an Active Carbon Recycling Energy System; ISIJ International, Vol. 55, No.2, pp.387-391 (2015).

Katsumi Yoshida, Hiroyuki Akimoto, Toyohiko Yano, Masaki Kotani, Toshio Ogasawara: Mechanical Properties of Unidirectional and Crossply SiCf/SiC Composites Using SiC Fibers with Carbon Interphase Formed by Electrophoretic Deposition Process; Progress in Nuclear Energy, Vol. 82, pp.148-152 (2015).

Areerak Rueanngoen, Masamitsu Imai, Katsumi Yoshida, Toyohiko Yano: Microstructure of Low-Dose Neutron Irradiated Si3N4 and SiAlON Ceramics after Thermal Annealing; Progress in Nuclear Energy, Vol. 82, pp.142-147 (2015).

Hiroshi Konishi, Mohd Idzat Idris, Masamitsu Imai, Katsumi Yoshida, Toyohiko Yano: Neutron Irradiation Effects of Oxide Sintering Additives for SiCf/SiC Composites; Energy Procedia, Vol. 71, pp.306-312 (2015).

Mohd Idzat Idris, Hiroshi Konishi, Masamitsu Imai, Katsumi Yoshida, Toyohiko Yano: Neutron Irradiation Swelling of SiC and SiCf/SiC for Advanced Nuclear Applications; Energy Procedia, Vol. 71, pp.328-336 (2015).

Katsumi Yoshida, Hideki Hyuga, Naoki Kondo, Hideki Kita: Surface Modification of Graphite Powder with Lanthanum Ultraphosphate by Chemical Process and Its Oxidation Resistance; Advanced Powder Technology, Vol. 26, pp.901-906 (2015).

Katsumi Yoshida: Recent Development of Ceramics-Based Continuous Fiber-Reinforced Composites; Bulletin of the Ceramic Society of Japan, Vol. 50, No. 6, pp.469-473 (2015).

Masafumi Akiyoshi, Ikuji Takagi, Toshimasa Yoshiie, Xu Qui, Koichi Sato and Toyohiko Yano: Effect of annealing on thermal conductivity in ceramics irradiated by electrons and neutrons; Energy Procedia, Vol.71, pp.320-327 (2015).

Yosuke Okubo, Toyohiko Yano, Katsumi Yoshida, Takuya Aoki, Toshio Ogasawara: Fabrication of SiC Fiber-reinforced SiC matrix composites by low temperature melt infiltration method using Si-Hf and Si-Y alloy ; Mechanical Properties and Performance of Engineering Ceramics and Composites IX, pp.101-111, John Weily &Sons, (2015)

Mohd Idzat Idris, Saisyun Yamazaki, Katsumi Yoshida and Toyohiko Yano: Recovery behavior of high purity cubic SiC polycrystals by post-irradiation annealing up to 1673K after low temperature neutron irradiation; J. Nucl. Mater., 465, 814-819 (2015)

Katsumi Yoshida, Chin-Chet See, Satoshi Yokoyama, Makoto Takahashi, Toyohiko Yano: Development of Porous SiC Ceramics Based on In-Situ Grain Growth; 3rd Conference on The Serbian Society for Ceramic Materials, June 17, 2015, Belgrade, Serbia, I-18.

Katsumi Yoshida, Toru Tsunoura, Yosuke Okubo, Toyohiko Yano, Takuya Aoki, Toshio Ogasawara: Fabrication of High Performance SiC Fiber-Reinforced SiC-Based Matrix Composites by Low Temperature Melt Infiltration Method Using Si-Hf and Si-Y Alloys; The 11th Pacific Rim Conference of Ceramic Societies (PACRIM 11), Jeju, Korea, August 31, 2015, MoI1-2.

Katsumi Yoshida, Hiroyuki Akimoto, Naoki Mizuta, Toyohiko Yano, Masaki Kotani, Toshio Ogasawara: Formation of Carbon and Boron Nitride Interphases for SiCf/SiC Composites by Electrophoretic Deposition Method; The 11th Pacific Rim Conference of Ceramic Societies (PACRIM 11), Jeju, Korea, August 31, 2015, MoD2-3.

Toru Tsunoura, Yosuke Okubo, Katsumi Yoshida, Toyohiko Yano, Toshio Ogasawara: Oxidation Behavior of Monolithic HfSi2 and SiCf/SiC-Based Matrix Composite Fabricated by Melt-Infiltration Method Using Si-Hf Alloy; The 11th Pacific Rim Conference of Ceramic Societies (PACRIM 11), Jeju, Korea, September 1, 2015, TuI1-2.

Mohd Idzat Idris, Masamitsu Imai, Katsumi Yoshida, Toyohiko Yano: Recovery Behavior of NITE SiC by Post-Irradiation Annealing up to 1673 K; The 11th Pacific Rim Conference of Ceramic Societies (PACRIM 11), Jeju, Korea, September 4, 2015, FrI1-3.

Yan You, Masamitsu Imai, Katsumi Yoshida, Toyohiko Yano: Recovery Behavior of Fast Neutron-Irradiated B4C Pellets by Post-Irradiation Annealing; The 11th Pacific Rim Conference of Ceramic Societies (PACRIM 11), Jeju, Korea, September 4, 2015, FrI1-4.

Mohd Idzat Idris, Katsumi Yoshida, Toyohiko Yano: Defects Annihilation Behavior of Neutron-Irradiated SiC Ceramics Densified by Liquid-Phase-Assisted Methods by Post-Irradiation Annealing; 17th International Conference on Fusion Reactor Materials (ICFRM-17), Aachen, Germany, October 14, 2015, Po3-52.

Toyohiko Yano, Hiroshi Konishi, Mohd Idzat Idris, Katsumi Yoshida: Neutron Irradiation Effects and recovery of Al2O3, Y2O3 and Yttrium Aluminum Garnet as Sintering Additives for SiC/SiC Composites; 17th International Conference on Fusion Reactor Materials (ICFRM-17), Aachen, Germany, October 14, 2015, Po3-66.

Toru Tsunoura, Yosuke Okubo, Katsumi Yoshida, Toyohiko Yano, Takuya Aoki, Toshio Ogasawara: Dry and Wet Oxidation Behavior of SiCf/SiC-Based Composites

Fabricated by Melt-Infiltration Method Using Si-Hf Alloy; The 9th International Conference on the Science and Technology for Advanced Ceramics (STAC-9) and The 9the Symposium on Transparent Oxide and Related Materials for Electronics and Optics (TOEO-9), Tsukuba, Japan, October 19, 2015, 1PS-15.

Katsumi Yoshida, Tetsu Kikuhara, Toyohiko Yano, Masaki Kotani, Takuya Aoki, Toshio Ogasawara: Carbon-Interphase Formation on Amorphous SiC Fibers in SiCf/SiC Composites by Electrophoretic Deposition Process; 14th Japan International SAMPE Symposium & Exhibition (JISSE14), Kanazawa, Japan, December 8, 2015, 148.

Toru Tsunoura, Yosuke Okubo, Katsumi Yoshida, Toyohiko Yano, Takuya Aoki, Toshio Ogasawara: Oxidation Behavior of SiCf/Si-C-Hf Composites Fabricated by Melt Infiltration Method Using Si-Hf Alloy; The 6th Japan Conference on Composite Materials (JCCM-6), Tokyo, March 4, 2015, 1D-03.

Mohd Idzat Idris, Masamitsu Imai, Katsumi Yoshida, Toyohiko Yano: Recovery Behavior of High Purity SiC Polycrystals by Post-Irradiation Annealing up to 1673K after Low Temperature Neutron Irradiation; 8th Student Meeting of the Kanto-Koetsu Division of the Atomic Energy Society of Japan, Tokyo, March 6, 2015, A-6.

Katsumi Yoshida, Toru Tsunoura, Toyohiko Yano: Fabrication and Characterization of YOF Ceramics; Annual Meeting of The Ceramic Society of Japan, 2015, Okayama, March 19, 2015, 2C33.

Toru Tsunoura, Yosuke Okubo, Katsumi Yoshida, Toyohiko Yano, Toshio Ogasawara, Takuya Aoki: Oxidation Behavior of HfSi2 with Boron Addition; Annual Meeting of The Ceramic Society of Japan, 2015, Okayama, March 19, 2015, 2C34.

Yan You, Toyohiko Yano, Katsumi Yoshida, Liang Sun: Characterization of Neutron-Irradiated B4C Control-Rod Material for Fast Reactor; 2015 Annual Meeting of the Atomic Energy Society of Japan, Hitachi, March 21, 2015, C38.

Makoto Takahashi, Katsumi Yoshida, Toyohiko Yano: Effect of Aluminum and Boron Additives on Microstructure of Porous SiC Ceramics with In-situ Grain Growth; 28th Fall Meeting of The Ceramic Society of Japan, Toyama, Japan, September 16, 2015, 1D01.

Tetsu Kikuhara, Katsumi Yoshida, Toyohiko Yano, Masaki Kotani, Toshio Ogasawara: Interphase Formation Process for Low-Conductive SiC Fibers by Electrophoretic Deposition Method; 28th Fall Meeting of The Ceramic Society of Japan, Toyama, Japan, September 17, 2015, 2C05.

Toru Tsunoura, Yosuke Okubo, Katsumi Yoshida, Toyohiko Yano, Takuya Aoki, Toshio Ogasawara: Oxidation Behavior of SiCf/SiC-Based Composites Fabricated by Melt Infiltration Method using Si-Hf Alloy in Steam-Containing Atmospheres; 28th Fall Meeting of The Ceramic Society of Japan, Toyama, Japan, September 17, 2015, 2D23.

Katsumi Yoshida, Toru Tsunoura, Toyohiko Yano, Takuya Aoki, Toshio Ogasawara: Steam Oxidation Behavior of HfSi2; 28th Fall Meeting of The Ceramic Society of Japan, Toyama, Japan, September 17, 2015, 2D24.

Mohd Idzat Idris, Masamitsu Imai, Katsumi Yoshida, Toyohiko Yano: The Influence of Sintering Additives on Neutron-Irradiated NITE SiC of Their Recovery Behavior; 2015 Fall Meeting of the Atomic Energy Society of Japan, Shizuoka, September 11, 2015, J45.

Yamato Sugitatsu, Toyohiko Yano, Katsumi Yoshida: Fabrication of Porous Ceramics using Natural Minerals as Radioactive Nuclides Absorbents and Their Cesium Absorption Characteristics; 2015 Fall Meeting of the Atomic Energy Society of Japan, Shizuoka, September 10, 2015.

Mohd Idzat Idris, Saisyun Yamazaki, Katsumi Yoshida, Toyohiko Yano: Effects of sintering additives on defects annihilation mechanism of neutron-irradiated NITE SiC by post-irradiation annealing; The 3rd Japan-China Academic Symposium on Nuclear Fuel Cycle", 2015. Dec. 2-5, Tokyo Japan, 1B37

H. Sagara, K. Matsumoto, I. Yamauchi, K. Nakao, C. Y. Han, T. Onishi, S. Koyama and M. Saito; Feasibility study of the fast breeder reactor blanket as a target of plutonium denaturing and TRU transmutation for enhancement of proliferation resistance and actinide management in the future fuel cycle, Prog. Nucl. Energy, Vol. 82, P. 92–97, July 2015.

H. Sagara, M. Katayama, K. Takao, C. Y. Han, and M. Saito; Challenges of Nuclear Security Educational Course Establishment as a Graduate School Program in Tokyo Institute of Technology, The 3rd Japan-China Academic Symposium on Nuclear Fuel Cycle(ASNFC2015), 2nd Dec.-5th, Tokyo, 2015.

Chi Young HAN, Hiroshi Sagara, and Masaki Ozawa; Feasibility of Nd Creation from Pr in Spent Nuclear Fuel by Neutron Irradiation of High Temperature Gas Cooled Reactor, The 3rd Japan-China Academic Symposium on Nuclear Fuel Cycle(ASNFC2015), 2nd Dec.-5th, Tokyo, 2015.

Tomooki Shiba, Hiroshi Sagara, Hirofumi Tomikawa; Passive Gamma Spectrometry of Low-Volatile FPs for Accountancy of Special Nuclear Material in Molten Core Material of Fukushima Daiichi Nuclear Power Plant

–Evaluation of Detector Response from Various Hypothetical Fuel Canister," Proc. INMM Ann. Mtg., July 12-16, 2015.

Rie Fujioka, Hiroshi Sagara and Chi Young Han; Effect of fast reactor fuel cycle strategies on TRU material balance and non-proliferation features (1) Strategies for rapid conversion of separated Pu to spent fuel form" AESJ 2016 spring meeting, 3001, 2016.

Takeshi Aoki, Hiroshi Sagara, Chi Young Han; Feasibility study of TRISO fuel for efficient Pu incineration and 3S feature enhancement (2) Nuclear security and non-proliferation assessment against threats of material diversion, Institute of Nuclear Material Management Japan Chapter Annual Meeting, Tokyo, 15-16 Oct. 2015.

Kazuki Nakahara, Hiroshi Sagara, Chi Young Han; Applicability of accompanying FP passive gamma measurement to special nuclear material estimation in fuel debris (3)- Proposal of simple burnup estimation techniques –, Institute of Nuclear Material Management Japan Chapter Annual Meeting, Tokyo, 15-16 Oct. 2015.

Rie Fujioka, Hiroshi Sagara, Han Chi Young, Effect of fast reactor fuel cycle strategy on TRU material balance and non-proliferation feature (2)The high burnup single-burning scenario, Institute of Nuclear Material Management Japan Chapter Annual Meeting, Tokyo, 15-16 Oct. 2015.

Soo Jun Barng, Hiroshi Sagara; Construction of fundamental nuclear characteristic databases of all fissionable actinide nuclides, Institute of Nuclear Material Management Japan Chapter Annual Meeting, Tokyo, 15-16 Oct. 2015.

Rei Kimura, Hiroshi Sagara, Satoshi Chiba、Development of nuclear fuel material isotopic composition measurement method based on #3606 the photonuclear reaction (1) Principle Confirmation, Institute of Nuclear Material Management Japan Chapter Annual Meeting, Tokyo, 15-16 Oct. 2015.

T. Shiba, H. Sagara, T. Hiyama, H. Tomikawa, Current status of accompanying FP passive gamma measurement to special nuclear material quantification in fuel debris, Institute of Nuclear Material Management Japan Chapter Annual Meeting, Tokyo, 15-16 Oct. 2015.

H. Sagara, C. Y. Han, Non-proliferation and Nuclear Security Education in Tokyo Tech, AESJ 2015 Fall Meeting, TN26 2015, invited.

Tetsuo Sawada: The Nuclear Power Problem: Junior High School Dialogue and Summit for Final Disposal of HLW; GLOBAL2015, September 21-24, Paris, France, GLOBAL2015-5323.

Tetsuo Sawada: Analysis of the structure of Genshiryoku-mura toward a paradigm shift of consensus building (5) – The prototype of Genshiryoku-mura -; 2016 Annual Meeting of Atomic Energy Society of Japan, Sendai, March 26-28, 2016, 3B07.

Tetsuo Sawada: Analysis of the structure of Genshiryoku-mura toward a paradigm shift of consensus building (4) – Complementary structure among Univ. of Tokyo, Osaka Univ. and Tokyo Inst. Tech.; 2015 Autumn Meeting of Atomic Energy Society of Japan, Shizuoka, September 9-11, 2015, M31.

Yoshiyuki Oguri, Kotaro Kondo, Jun Hasegawa, Kazuhiko Horioka: Numerical Analysis of the Hydrodynamic Behavior of Ion-Beam-Heated Uranium Targets for Equation-of-State Studies under Extreme Conditions; Energy Procedia, Vol.71, pp. 244-251 (2015).

Kamontip Ploykrachang, Jun Hasegawa, Kotaro Kondo, Hitoshi Fukuda, Yoshiyuki Oguri: Design of a Proton-induced Quasimonochromatic Micro-XRF Setup for Wet Biological Samples; Energy Procedia, Vol.71, pp. 252-260 (2015).

Kotaro Kondo, Jun Hasegawa, Kazuhiko Horioka, Yoshiyuki Oguri: Velocity Measurement of Electromagnetically-Driven Shock Wave to Produce a Dissociated Hydrogen Target for Beam Interaction Experiment; Energy Procedia, Vol.71, pp. 268-273 (2015).

Tamotsu Toriyama, Satoshi Suzuki, Katsunori Kawasaki, Yasuo Takagi, Masayuki Nagai, Hitoshi Fukuda, Kotaro Kondo, Yoshiyuki Oguri: Effect of Vacuum Drying in Target Preparation from Potassium Hydroxide Solution on the Spectra of Rutherford Backscattering Spectroscopy; Energy Procedia, Vol.71, pp. 274-281 (2015).

Tomoyuki Matsuda, Shingo Enomoto, Yoko Kebukawa, Takeo Kaneko, Hitoshi Fukuda, Yoshiyuki Oguri, Satoshi Yoshida, Kensei Kobayashi: Formation of Complex Amino Acid Precursors from Possible Interstellar Media by Particles Irradiation; 2015 International Chemical Congress of Pacific Basin Societies (PAC CHEM), December 15-20, 2015, Honolulu, Hawaii, USA.

Kotaro Kondo, Masafumi Kumaki, Jun Tamura, Yoshiyuki Oguri, Takeshi Kanesue, Masahiro Okamura: Laser Pulse-Width Dependence of Charge State Distributions in a Picosecond Laser Ion Source; 2015 Fall Meeting of the Atomic Energy Society of Japan, Shizuoka, September 9-11, 2015, P36

Naoto Hagura, Koh-ichi Mochiki, Yoshiyuki Oguri, Kotaro Kondo, Hitoshi Fukuda, Noriyosu Hayashizaki: Development of a Compact Cold-Cathode PIG Negative-Ion Source for Electrostatic Tandem Accelerators (2) Beam Extraction and Mass Spectrometry

Experiment; 2015 Fall Meeting of the Atomic Energy Society of Japan, Shizuoka, September 9-11, 2015, P37.

Yuchao Hu, Kotaro Kondo, Yoshiyuki Oguri, Hitoshi Fukuda: Performance Evaluation of a Syringe-Needle Type Proton-Induced X-ray Source by Geant4 Monte Carlo Simulation; 2015 Fall Meeting of the Atomic Energy Society of Japan, Shizuoka, September 9-11, 2015, P44.

Yuchao Hu, Kotaro Kondo, Hitoshi Fukuda, Yoshiyuki Oguri: Quantitative Evaluation of the Intensity of a Syringe-Needle Type Proton-Induced X-ray Source by Emittance Measurement of the Primary Proton Beam and Geant4 Simulation; 2016 Annual Meeting of the Atomic Energy Society of Japan, Sendai, March 26-28, 2016, 2M06.

Satoshi niida, Tomohiro Yokozuka, Kotaro Kondo, Yoshiyuki Oguri: Temporal Evolution Measurement of Electromagnetically-Driven Plasmas for Development of an Atomic Hydrogen Target with High Dissociation Degree; 2016 Annual Meeting of the Atomic Energy Society of Japan, Sendai, March 26-28, 2016, 2M23.

Yuya Kato, Naoto Hagura, Yoshiyuki Oguri, Kotaro Kondo, Hitoshi Fukuda, Noriyosu Hayashizaki: Development of a Compact Cold-Cathode PIG Negative-Ion Source for Electrostatic Tandem Accelerators - Optimization of the Magnetic Field Strength for Plasma confinement in the Discharge Chamber; 2016 Annual Meeting of the Atomic Energy Society of Japan, Sendai, March 26-28, 2016, 2M08.

Yoshiyuki Oguri, Wenkai Teng, Kotaro Kondo, Hitoshi Fukuda: PIXE Analysis of Trace Element Migration from Hydroponic Nutrient Solution to Crops; 30th Symposium on PIXE in Japan, Takasaki, October 27-30, 2015, #3-4

Yuchao Hu, Hitoshi Fukuda, Yoshiyuki Oguri: Evaluation of the X-ray Distribution of a Syringe-Needle Type Proton-Induced X-ray Source by Geant4 Simulation; 30th Symposium on PIXE in Japan, Takasaki, October 27-30, 2015, #5-2

Ken-ichi Tanaka, Jun Ueno, Masataka Adachi and Satoshi Chiba: Improvement of a calculation procedure of neutron-flux distribution for radioactivity inventory estimation for decommissioning of nuclear power plants, Progress in Nuclear Energy 85 (2015) 254-270.

H.Makii, S.Ota, T.Ishii, Y.Wakabayashi, K.Furutaka, K.Nishio, I.Nishinaka, S.Chiba, M.Igashira and A.Czeszumska: Development of a measurement system for the determination of (n,γ) cross-sections using multi-nucleon transfer reactions, Nucl. Instr. Meth. A 797, 83-93(2015).

K.Nishio, K.Hirose, R.Leguillon, H.Makii, I.Nishinaka, R.Orlandki, J.Smallcombe, K.Tsukada, S.Chiba}, T.Ohtsuki, R.Tatsuzawa and N.Takaki: Fission study of actinide nuclei using multi-nucleon transfer reactions, Physics Procedia {¥bf 64} (2015) 140-144.

F.A.Ivanyuk, S.Chiba and Y.Aritomo: The Scission Point Configuration and the Multiplicity of Prompt Neutrons, Physics Procedia 64 (2015) 28-33.

Y.Aritomo, S.Chiba and K.Nishio: Independent fission yields studied based on Langevin equation, Progress in Nuclear Energy, 85 (2015) 568-572.

Tsugio Yokoyama, Yuki Tanoue, Atsunori Terashima, Masaki Ozawa: Production of Rhenium by Transmuting Tungsten Metal in Fast Reactors with Moderator; Journal of Energy and Power Engineering Vol.10, No.3, pp.159-165 (2016).

Chikako Ishizuka, Satoshi Chiba, Alexander V. Karpov, Yoshihiro Aritomo: Dynamical approach to isotopic-distribution of fission fragments from actinide nuclei; The 5th International Workshop on Compound-Nuclear Reactions and Related Topics, October 19-23, 2015, Tokyo, JAPAN, CNR*15.

Satoshi Chiba, Ryohei Shioya, Chikako Ishizuka: Assessing Accuracy of Independent Fission Yield of 235 U by Aggregate Decay Properties; 2015 ANS Winter Meeting and Nuclear Technology Expo, November 8-12, 2015, Washington, DC, U.S.A.,

Chikako Ishizuka, Satoshi Chiba, Yoshihiro Aritomo, Fedir Ivanyuk: Improvement of fission reaction method based on the Langevin model; 2015 Autumn Meeting of Atomic Energy Society of Japan, Shizuoka, September 9-11, 2015.

Chikako Ishizuka, Yoshihiro Aritomo, Alexander V. Karpov, Satoshi Chiba: Improvement of the charge distribution based on the Langevin model; 2016 Autum Meeting of The Physical Society of Japan, Osaka, September 25-28, 2015.

Chikako Ishizuka, Yoshihiro Aritomo, Alexander V. Karpov, Satoshi Chiba: Dynamical Approach to Isotpic-Distribution of Fission Fragments from Actnide Nuclei; The 5th International Workshop on Compound-Nuclear Reactions and Related Topics, October 19-23, 2015, Tokyo, JAPAN, CNR*15.

Chikako Ishizuka, Yoshihiro Aritomo, Alexander V. Karpov, Satoshi Chiba: Isotopic distribution of 235U+n→ 236U” at low E* using 4D-Langevin calculation; 2015 Nuclear data workshop, Tokai, November 19-20, 2015.

Chikako Ishizuka, Satoshi Chiba, Nicolae Carjan: Charge polarization and nuclear elongation at scission; 2016

Annual Meeting of Atomic Energy Society of Japan, Sendai, March 26-28, 2016.

Chikako Ishizuka, Satoshi Chiba, Nicolae Carjan: Charge polarization and nuclear elongation at scission; 2016 Annual Meeting of The Physical Society of Japan, Sendai, March 19-22, 2016.

Tsugio Yokoyama, Yuki Tanoue, Atsunori Terashima, Masaki Ozawa: Rhenium Production from Tungsten in Fast Reactors; 2015 Fall Meeting of the Atomic Energy Society of Japan, Shizuoka, September 9-11, 2015, A10.

Atsunori Terashima, Leila Safavi-Tehrani, Mikael Nilsson, Masaki Ozawa: Predictive Simulation on Nuclear Transmutation of Rare Earth Elements and Evaluation of the Reliability by Nuclear Analysis of PIE at UC Irvine TRIGA® Reactor; The 3rd Japan-China Academic Symposium on Nuclear Fuel Cycle (ASNFC 2015), Tokyo, Japan, December 2-5, 2015, 2B-13.

Tsugio Yokoyama, Yuki Tanoue, Atsunori Terashima, Masaki Ozawa: Optimizing the Transmutation Rate of Tungsten to Rhenium by Using Zirconium Hydride Moderators in Fast Reactors; The 3rd Japan-China Academic Symposium on Nuclear Fuel Cycle (ASNFC 2015), Tokyo, Japan, December 2-5, 2015, 2B-15.

Atsunori Terashima, Toshitaka Kaneshiki, Masao Nomura, Masaki Ozawa: A Fundamental Study on Separation of Platinum Group Elements from High Level Liquid Waste by Using Crown Ether Resins; The Fourth International Education Forum on Environment and Energy Science, Maui, Hawaii, USA, December 6-10, 2015, D137.

Atsunori Terashma, Leila Safavi-Tehrani, Mikael Nilsson, Masaki Ozawa: Basic Research on the Element Transmutation of All the Fission Products Using Nuclear Reactors, (3)Validation of MVP-BURN Code by Neutron Activation Analysis in UCI-TRIGA® Reactor; 2016 Annual Meeting of the Atomic Energy Society of Japan, Miyagi, March 26-28, 2016, 2O15.

Atsunori Terashma, Masaki Ozawa: Basic Evaluation of Resource Availability of All Fission Products by Partitioning and Transmutation; Student's Poster Session: 2016 Annual Meeting of the Atomic Energy Society of Japan, Miyagi, March 27, 2016, 23.

Keisuke Tajima, Atsushi Nezu, Haruaki Matsuura, Hiroshi Akatsuka: Experimental Study on a Weakly-Ionized Rarefied Arc-Jet Flowing Supersonically along a Mirror and Cusp Magnetic Field; International Journal of Plasma Environmental Science and Technology, Vol. 9, No. 1, pp. 7-12 (2015).

Yoshihiro Shimizu, Yuuske Kittaka, Atsushi Nezu, Haruaki Matsuura, Hiroshi Akatsuka: Excited State Distributions of Hydrogen Atoms in the Microwave Discharge Hydrogen Plasma and the Effect of Electron Energy Probabilistic Function; IEEE Transactions on Plasma Science, Vol. 43, No. 5, pp. 1758-1768 (2015).

Hao Tan, Atsushi Nezu, Hiroshi Akatsuka: Kinetic Model and Spectroscopic Measurement of NO (A, B, C) States in Low-Pressure N_2-O_2 Microwave Discharge; Japanese Journal of Applied Physics, Vol. 54, No. 9, 096103 (2015).

Hao Tan, Atsushi Nezu, Hiroshi Akatsuka: Spectroscopic Investigation of the NO C $^2\Pi$ De-Excitation Process by Collision with O_2 X $^3\Sigma_g^-$ in a Low-Pressure N_2-O_2 Mixture Microwave Discharge, Japanese Journal of Applied Physics, Vol. 55, No. 1, 01AH04 (2015).

Hao Tan, Atsushi Nezu, Hiroshi Akatsuka: Vibrational and Rotational Temperatures of NO A $^2\Sigma^+$ Metastable State in N_2-O_2 Mixture Microwave Discharge; The 42nd IEEE International Conference on Plasma Science (ICOPS2015), May 25-28, Antalya, Turkey, p. 45.

Ampan Laosunthara, Satoshi Tsuno, Takeshi Nakahagi, Hiroshi Akatsuka: Hybrid Simulation of Weakly-Ionized Rarefied Arc-Jet Flowing Supersonically along Diverging Magnetic Field; The 42nd IEEE International Conference on Plasma Science (ICOPS2015), May 25-28, Antalya, Turkey, p. 46.

Yurina Honda, Atsushi Nezu, Haruaki Matsuura, Hiroshi Akatsuka: Spectroscopic Measurement of Fulcher-α Band of Microwave Discharge H_2/D_2 Plasmas, 32nd International Conference on Phenomena in Ionized Gases (32nd ICPIG), July 26-31, 2015, Iasi, Romania, P2-18.

Ampan Laosunthara, Satoshi Tsuno, Hiroshi Akatsuka: Numerical Study on Anisotropic Ion Temperature in Weakly Ionized Plasma Flowing Supersonically along Open Field Line; ICAEME and 2nd ACEIAT 2015, August, 2015, Thonburi, Thailand, pp. 89 - 91.

Hiroshi Akatsuka: Plasma Diagnostics Using Optical Emission Spectroscopy; The 10th Asian-European International Conference on Plasma Surface Engineering (AEPSE2015), September 20-24, 2015, Jeju, South Korea, Tutorial-I, Fundamentals and Processes, pp. 51-99.

Hiroshi Akatsuka: Possibility of Electron Temperature and Density Monitoring of Argon Plasma by Intensity Ratio Measurement of Ar I Lines; The 10th Asian-European International Conference on Plasma Surface Engineering (AEPSE2015), September 20-24, 2015, Jeju, South Korea, p. 94.

Hiroshi Akatsuka, Yoshinori Tanaka: Discussion on Electron Temperature of Low-Pressure Discharge Oxygen Plasma with Non-Maxwellian EEDF Based on Statistical Physics; 68th Annual Gaseous Electronics Conference/9th International Conference on Reactive Plasmas/33rd Symposium on Plasma Processing

(68-GEC/9-ICRP/33-SPP), UF3-1, October 12-16, 2015, Honolulu, Hawaii, USA, Bulletin of the American Physical Society, Vol. 60, No. 9, pp. 148-149 (2015).

Hao Tan, Atsushi Nezu, Hiroshi Akatsuka: Spectroscopic Examination of Molecular Spectra in Mixture Gaseous Microwave Discharge (N_2-O_2 and N_2-H_2); 68th Annual Gaseous Electronics Conference/9th International Conference on Reactive Plasmas/33rd Symposium on Plasma Processing (68-GEC/9-ICRP/33-SPP), GT1-57, October 12-16, 2015, Honolulu, Hawaii, USA, Bulletin of the American Physical Society, Vol. 60, No. 9, p. 41 (2015).

Hao Tan, Atsushi Nezu, Hiroshi Akatsuka: Spectroscopic Observation of NO (A, B, C) States and their Chemical Kinetics in Low-Pressure N_2-O_2 Microwave Discharge; 3rd ISNPEDADM 2015 (New Electrical Technologies for Environment), October 26-29, 2015, Reunion, France.

Hiroshi Akatsuka, Eiko Tanaka, Kentaro Ando, Atsushi Nezu, Daisuke Kuwahara, Shunjiro Shinohara: Approximate Monitoring of Electron Temperature and Density of Argon-Based Plasma by Line-Intensity Ratio Measurement with Collisional Radiative Model; 2015 International Symposium on Dry Process (37-DPS), pp. 95-96, November 5-6, 2015, Awaji, Japan, P-68.

Jun-Seok Oh, Maito Kakuta, Hiroshi Furuta, Hiroshi Akatsuka, Akimitsu Hatta: Production Efficiency of RONS in Plasma Activated Water by Using Micro-sized Atmospheric-Pressure Plasma Jet; 2015 International Symposium on Dry Process (37-DPS), pp. 189-190, November 5-6, 2015, Awaji, Japan, P-63.

Hiroshi Akatsuka, Hao Tan, Atsushi Nezu: Spectroscopic Observation of γ, β and δ Bands of NO Excited States and Relevant Excitation Kinetics in Low-Pressure N_2-O_2 Microwave Discharge; The Joint Symposium of the 9th Asia-Pacific International Symposium on the Basics and Applications of Plasma Technology (APSPT-9) and the 28th Symposium on Plasma Science for Materials (SPSM-28), December 12-14, 2015, Nagasaki, Japan, 12PM-C-1.

Jun Takeda, Atsushi Nezu, Hiroshi Akatsuka: Experimental Study on Effect of Electric field on Plasma Flow with Electrons Magnetized and Ions Nonmagnetized; The Joint Symposium of the 9th Asia-Pacific International Symposium on the Basics and Applications of Plasma Technology (APSPT-9) and the 28th Symposium on Plasma Science for Materials (SPSM-28), December 12-14, 2015, Nagasaki, Japan, P1-21.

Ampan Laosunthara, Hiroshi Akatsuka: Numerical Study on Space Potential in Expanding Arc-jet Plasma Flowing Supersonically through Open Field Line; The Joint Symposium of the 9th Asia-Pacific International Symposium on the Basics and Applications of Plasma Technology (APSPT-9) and the 28th Symposium on Plasma Science for Materials (SPSM-28), December 12-14, 2015, Nagasaki, Japan, P1-22.

Ampan Laosunthara, Hiroshi Akatsuka: Study on Non-thermal Equilibrium of Ion on Weakly Ionized Plasma Flowing Supersonically through Open Field Lines; Joint Technical Meeting on "Plasma Science and Technology", "Electrical Discharges" and "Pulsed Power Technology", IEE Japan, Sapporo, June 4-6, 2015, PST-15-008, ED-15-026, PPT-15-008, pp. 39-42.

Yoshinori Tanaka, Hiroshi Akatsuka: Statistical-Mechanical Discussion on Electron Temperature of Non-Maxwellian EEDF Plasma; Joint Technical Meeting on "Plasma Science and Technology", "Electrical Discharges" and "Pulsed Power Technology", IEE Japan, Sapporo, June 4-6, 2015, PST-15-036, ED-15-054, PPT-15-036, pp. 43-48.

Hiroshi Akatsuka, Hao Tan, Atsushi Nezu, Haruaki Matsuura: Optical Emission Spectroscopic Observation of Low-pressure N_2-O_2 Mixture Plasma and its Excitation Kinetics in a Lab-Scale Discharge Experiment; The Annual Meeting of the Spectroscopical Society of Japan, Tokyo, June 1-3, 2015, p. 2.

Ryutaro Yamashiro, Atsushi Nezu, Hiroshi Akatsuka: Characteristics of Nitrogen Arc-Jet Plasma Flowing through Open-Magnetic-Field; Technical Meeting on "Plasma Science and Technology", IEE Japan, Higashi-Hiroshima, August 10-11, 2015, PST-15-050, pp. 25-30.

Hiroshi Akatsuka, Yoshinori Tanaka: Reconsideration of Electron Temperature of Plasmas with Non-Maxwellian EEDF Based on Statistical-Thermodynamical Discussion; The 76th Japan Society of Applied Physics (JSAP) Autumn Meeting, Nagoya, September 13-16, 2015, 13p-1F-4, p. 07-004.

Hao Tan, Atsushi Nezu, Hiroshi Akatsuka: Vibrational and Rotational Temperature Dependence of NH in Microwave N_2-H_2 Mixture Gas Discharge; The 76th Japan Society of Applied Physics (JSAP) Autumn Meeting, Nagoya, September 13-16, 2015, 15a-2V-2, p. 07-038.

Hiroshi Akatsuka: On the Possibility of Simplified Monitoring of Electron Temperature and Density of Low-Pressure Argon Plasma by Line-Pair Intensity-Ratio Measurement with CR-Model Analysis; 2015 Annual Conference of Fundamentals and Materials Society IEE Japan, Kanazawa, September 17-18, 2015, p. 219.

Haruaki Matsuura, Atsushi Nezu, Hiroshi Akatsuka, Nobuaki Sato: Pyrochemical Treatment of Fuel Debris Using Selective Fluorination and Molten Salt Electrolysis (4) Fluorination behavior of Uranium-Zirconium Mixed Oxide with various Compositions; 2015 Fall Meeting of

Atomic Energy Society of Japan, Shizuoka, September 9-11, 2015, E05.

Ampan Laosunthara, Hiroshi Akatsuka: Numerical Study on Potential Formation of Weakly Ionized Plasma Flowing Supersonically Through Open Field Line; The 32nd Annual Meeting of Japan Society of Plasma Science and Nuclear Fusion Research, Nagoya, November 24-27, 2015, 24aD04P.

Eiko Tanaka, Jun'ya Sato, Hiraku Iwaya, Tomoya Yamase, Hiroshi Akatsuka, Keiji Sawada, Motoshi Goto, Daisuke Kuwahara, Shunjiro Shinohara: Wide Area Plasma Spectroscopy Using Small Helicon Device (SHD); The 32nd Annual Meeting of Japan Society of Plasma Science and Nuclear Fusion Research, Nagoya, November 24-27, 2015, 26aD17P.

Hiroshi Akatsuka, Yoshinori Tanaka: Statistical-Mechanical Discussion on Temperatures of Non-Equilibrium Plasma; The 32nd Annual Meeting of Japan Society of Plasma Science and Nuclear Fusion Research, Nagoya, November 24-27, 2015, 27aC04.

Jun Takeda, Atsushi Nezu, Hiroshi Akatsuka: Experimental Study on Effect of Electric Field on Plasma Flow with Electrons Magnetized and Ions Nonmagnetized; 2016 National Convention I.E.E. Japan, Sendai, March 16-19, 2016, vol. 1, p. 187.

Hiroshi Akatsuka, Yoshinori Tanaka: Statistical-Mechanical Discussion on Electron Temperature of Plasmas with Non-Maxwellian EEDF (2) N_2 Plasma; 71st Annual Meeting of the Physical Society of Japan, Sendai, March 19-22, 2016, Vol. 71, No. 1, p. 967.

Jun S, Jung Y-S, Suh HN, Wang W, Kim MJ, Oh YS, Lien E, Shen X, Matsumoto Y, McCrea P, Li L, Chen J, Park J-I: LIG4 mediates Wnt signaling-induced radioresistance; Nat. Commun., Vol.7, pp.10994, 2016.

Sharma MK, Imamichi S, Fukuchi M, Samartha RM, Tomita M, Matsumoto Y: In cellulo phosphorylation of XRCC4 Ser320 by DNA-PK induced by DNA damage; J. Radiat. Res., Vol.57, pp.115-120, 2016.

Björkman A, Du L, Felgentreff K, Rosner C, Kamdar RP, Kokaraki G, Matsumoto Y, Davies EG, van der Burg M, Notarangelo LD, Hammarström L, Pan-Hammarström Q: DNA-PKcs is involved in immunoglobulin class switch recombination in human B-cells; J. Immunol., Vol.195, pp.5608-5615, 2015.

Fukuchi M, Wanotayan R, Liu S, Imamichi S, Sharma MK, Matsumoto Y: Lysine 271 but not lysine 210 of XRCC4 is required for the nuclear localization of XRCC4 and DNA ligase IV; Biochem. Biophys. Res. Commun., Vol.461, pp.687-694, 2015.

Samartha RM, Samartha M, Matsumoto Y: Utilization of Cytogenetic Biomarkers as Tool for Assessment of Radiation Injury and Evaluation of Radiomodulatory Effects of Various Medicinal Plants; Drug Design, Development and Therapy, Vol.9, pp.5355-5372, 2015.

Yoshihisa Matsumoto, Mikoto Fukuchi, Sicheng Liu, Shoji Imamichi, Mukesh K Sharma: Regulation of XRCC4/DNA Ligase IV Complex in DNA Double-strand Break Repair; 15th International Congress of Radiation Research, Kyoto, May 25-29, 2015, 3-D-OS-11-04.

Yoshihisa Matsumoto: Recognition and Repair of DNA Double-strand Breaks – Molecular Mechanisms and Implication in Medicine; International Workshop on Ionizing and Non-ionizing Radiation Influence on Structure and Biophysical Properties of Living Cells, Tsughkadzor (Armenia), September 25-27, 2015, Session 2 (Plenary Talk).

Yoshihisa Matsumoto: Mechanisms of the repair of DNA double-strand breaks; YITP & YIPQS Workshop Biological & Medical Science based on Physics: Radiation and phyiscs, Physics on medical science, Modeling for biological system, Kyoto, November 5-7, 2015, Session 3-1: Biological effects of radiation.

M. Nakase, K. Takeshita, T. Kobayashi, H.shiwaku, T. Yaita: Structure and complexation studies on 2,2'-bipyridyl and trivalent lanthanides; Separation Science and Technology, Vol.50, pp.2832-2835, 2015.

Yuji Miyazaki, Shin-ichi Suzuki, Toru Kobayashi, Tsuyoshi Yaita, Yusuke Inaba, Kenji Takeshita, Atsunori Mori: Synthetic Design of TPEN Derivatives for Selective Extraction of Trivalent Minor Actinides against Lanthanides; Chemistry Letters, Vol.44, No.12, pp.1626–1636, 2015.

Takuya Kawamura, Kenji Takeshita: Development of Copolymer Gel-Silica Composite with High Hexavalent Nitrogen-donor Ligand Content for the Establishment of Practical Gel-liquid Extraction Process; Chemistry Letters, Vol.45, No.2, pp.155-157, 2015.

Hideharu Takahashi, Keita Kanazawa, Tatsuya Fukuda, Takeshi Ogata, Yusuke Inaba, Kenji Takeshita: Fundamental Study on Cs Recovery Technology from Plant-based Waste by Hydrothermal Treatment Process Using Subcritical Water and Adsorption Coagulation-sedimentation Process; Journal of the Society for Remediation of Radioactive Contamination in the Environment, Vol.3, No.4, pp.199-205, 2015.

Xiangbiao Yin, Hideharu Takahashi, Yusuke Inaba, Kenji Takeshita: Desorption of Cesium Ions from Vermiculite with Sea Water by Hydrothermal Process; Chemistry Letters, Vol.45, No.3, pp.256–258, 2015.

Junichi Munesawa, Noboru Ito, Ryoichi Ogata, Soya Inoue, Yusuke Inaba, Miki Harigai: Development of Cesium Recovery System for High Efficiency and Volume Reduction - Behavior of Cesium salt in Combustion Treatment of Prussian Blue -; Journal of the Society for Remediation of Radioactive Contamination in the Environment, Vol.4, No.1, pp.35-44, 2016.

Kenji Takeshita, Hideharu Takahashi, Yusuke Inaba: 6. Recovery of Tritium from Contaminated Water by H2/H2O Exchange Process with Electrolyzer; Journal of plasma and fusion research, Vol.92, No.1, pp.39-44, 2016.

Yusuke Inaba, Yusuke Sakai, Keita Kanazawa, Miki Harigai, Hiroshi Oaki, Kenji Takeshita: Development of a Granulation Method for Prussian Blue by Thin-film Gel Coating; Chemistry Letters, Vol.45, No.7, pp.776-778, 2016. (Accepted: March 31, 2016)

Kenji Takeshita, Yusuke Inaba, Hideharu Takahashi: Development of Separation Process of PGMs and Molybdenum from High-level Liquid Waste; The Tenth International Conference on Methods and Applications of Radioanalytical Chemistry (MARC X), Honolulu, USA, April 12-17, 2015, 560.

Shinta Watanabe, Yuki Sawada, Masato Nakaya, Masahito Yoshino, Tatsuya Kameyama, Tsukasa Torimoto, Yusuke Inaba, Hideharu Takahashi, Kenji Takeshita, Jun Onoe: Many-Body effects on the UV-Vis Spectra of Prussian Blue Nanoparticles; The 13th Annual Meeting of Society of Nano Science and Technology, Sendai, May 11-13, 2015, O-13.

Tetsuji Yano, K. Watanabe, K. Mori, T. Amagasa, R. Nakata, R., J. Ogata, T. Kishi, K. Takeshita, Y. Miura, N. Kanehira, : Laboratory-scale cold cap analysis for liquid-fed ceramic melter using high-temperature X-ray CT; 2015 Glass and Optical Materials Division Annual Meeting (GOMD-DGG2015), Miami, USA, May 17-21, 2015.

Kenji Takeshita, Yusuke Inaba, Hiroshi Oaki, Tsuyoshi Yaita, Shinichi Suzuki, Atsunori Mori: Separation of Minor Actinides and Lanthanides by Thermosensitive Gel Immobilizing Multidentate Podand-type Ligand; The 32th Symposium on Rare Earths of the Rare Earth Society of Japan, Kagoshima, May 21-22, 2015, 1B-11.

Kenji Takeshita, Hideharu Takahashi, Yusuke Inaba, Junichi Munasawa: Establishment of high-efficiency, high-volume reduction cesium recovery system (From Cs concentrated recovery to immobilization of Cs in glass) – (1)Outline of system and volume reduction effect -; The 4th Annual Meeting of the Society for Remediation of Radioactive Contamination in Environment, Tokyo, July 8-9, 2015, S5-1.

Hideharu Takahashi, Imari Takatsuka, Yusuke Inaba, Kenji Takeshita: Establishment of high-efficiency, high-volume reduction cesium recovery system (From Cs concentrated recovery to immobilization of Cs in glass) - (2)Study on Advancement of Cs Separation from Polluted Soil by Hydrothermal Treatment -; The 4th Annual Meeting of the Society for Remediation of Radioactive Contamination in Environment, Tokyo, July 8-9, 2015, S5-2.

Yusuke Inaba, Miki Harigai, Kenji Takeshita, Junichi Munasawa: Establishment of high-efficiency, high-volume reduction cesium recovery system (From Cs concentrated recovery to immobilization of Cs in glass) - (6)Vitrification of Cesium Salt and Fundamental Study of Immobilization -; The 4th Annual Meeting of the Society for Remediation of Radioactive Contamination in Environment, Tokyo, July 8-9, 2015, S5-6.

Masahiko Nakase, Toru Kobayashi, Kenji Takeshita, Hideaki Shiwaku, Tsuyoshi Yaita: Study on Complex Structure and Interaction of Phenanthroline Amide Derivatives –Lanthanide (III) by Synchrotron Radiation XAFS; The 18th Annual XAFS Meeting of the Japanese XAFS Society (JXAFS18), Tsukuba, July 29-31, 2015, 1C11.

Hirotaka Sawada, Shinta Watanabe, Makoto Nakatani, Masahito Yoshino, Jun Onoe, Yusuke Inaba, Hideharu Takahashi, Kenji Takeshita: Adsorption Spectrum Analysis of Ferrocyanide Nano Particles by First-principles Calculation (I); The 28th DV-Xa Annual Meeting, Yamagata, August 5, 2015, OS-1.

Shinta Watanabe, Hirotaka Sawada, Makoto Nakatani, Masahito Yoshino, Jun Onoe, Yusuke Inaba, Hideharu Takahashi, Kenji Takeshita: Adsorption Spectrum Analysis of Ferrocyanide Nano Particles by First-principles Calculation (II); The 28th DV-Xa Annual Meeting, Yamagata, August 5, 2015, OS-2.

Miki Harigai, Yusuke Inaba, Hideharu Takahashi, Yaolu Zou, Kenji Takeshita: Separation of cesium by synthesized Prussian blue analogs; The 47th Autumn Meeting of the Society of Chemical Engineers, Sapporo, September 9-11, 2015, ZC2P03.

Takuya Kawamura, Kenji Takeshita: Adsorption and recovery of Cd by Chromatographic Agent coating TPEN-NIPA-Gel with high TPEN content; The 47th Autumn Meeting of the Society of Chemical Engineers, Sapporo, September 9-11, 2015, ZC2P04.

Yang Hongrui, Akihiko Yamauchi, Yusuke Inaba, Kenji Takeshita: Development of Crown Ether-NIPA Gel for Absorption of Strontium; The 47th Autumn Meeting of the Society of Chemical Engineers, Sapporo, September 9-11, 2015, ZC2P05.

Hideharu Takahashi, Imari Takatsuka, Yusuke Inaba, Kenji Takeshita: A Study on the Advancement of Cs Separation

Process from Polluted Soil Using Subcritical Water; 2015 Fall Meeting of the Atomic Energy Society of Japan, Shizuoka, September 9-11, 2015, H42.

Masahiko Nakase, Toru Kobayashi, Hideaki Shiwaku, Tsuyoshi Yaita, Kenji Takeshita: Fundamentals of size recognition of lanthanides(III) ions by multidentate N-donor and N,O-heterodonor ligands; 2015 Fall Meeting of the Atomic Energy Society of Japan, Shizuoka, September 9-11, 2015, J31.

Kenji Takeshita, Ippei Amamoto, Yasuo Ayame, Takashi Onishi, Jun Onoe, Koichi Narita: Development of Recovery Process of Platinum-group Metals from HLLW for Stable Production and Volume Reduction of Homogeneous Vitrified Object: (1)Overview; 2015 Fall Meeting of the Atomic Energy Society of Japan, Shizuoka, September 9-11, 2015, E21.

Yusuke Inaba, Hideharu Takahashi, Kenji Takeshita, Jun Onoe: Development of Recovery Process of Platinum-group Metals from HLLW for Stable Production and Volume Reduction of Homogeneous Vitrified Object: (2) Synthesis and Sorption Tests of Ferrocyanides for Separation of Platinum Group Metals and Molybdenum; 2015 Fall Meeting of the Atomic Energy Society of Japan, Shizuoka, September 9-11, 2015, E22.

Ippei Amamoto, Hidekazu Kobayashi, Yasuo Ayame, Kazuo Utsumi, Kenji Takeshita, Jun Onoe, Sachiko Nagayama, Yoshio Hasegawa: Development of Recovery Process of Platinum-group Metals from HLLW for Stable Production and Volume Reduction of Homogeneous Vitrified Object: (3) Synthesis of ceramics support materials and their sorption characteristics; 2015 Fall Meeting of the Atomic Energy Society of Japan, Shizuoka, September 9-11, 2015, E23.

Yuki Sawada, Shinta Watanabe, Masato Nakaya, Jun Onoe, Yusuke Inaba, Hideharu Tachibana, Kenji Takeshita: Development of Recovery Process of Platinum-group Metals from HLLW for Stable Production and Volume Reduction of Homogeneous Vitrified Object: (4) Infrared attenuated total reflection spectroscopic and density-functional studies on the structuralproperties of ferrocyanide nanoparticles; 2015 Fall Meeting of the Atomic Energy Society of Japan, Shizuoka, September 9-11, 2015, E24.

Yuki Sawada, Shinta Watanabe, Masato Nakaya, Tatsuya Kameyama, Tsukasa Torimoto, Jun Onoe, Yusuke Inaba, Hideharu Takahashi, Kenji Takeshita: Development of Recovery Process of Platinum-Group Metals from HLLW for Stable Production and Volume Reduction of Homogeneous Vitrified Object: (5) UV-visible diffuse reflectance spectroscopic and density-functional studies on the electronic structures of ferrocyanide nanoparticles; 2015 Fall Meeting of the Atomic Energy Society of Japan, Shizuoka, September 9-11, 2015, E25.

Shinta Watanabe, Yuki Sawada, Masato Nakaya, Masahito Yoshino, Takanori Nagasaki, Jun Onoe, Yusuke Inaba, Hideharu Takahashi, Kenji Takeshita: Development of Recovery Process of Platinum-group Metals from HLLW for Stable Production and Volume Reduction of Homogeneous Vitrified Object: (6) First-principles Many-electron Calculation Study on the UV-Visible Diffuse Reflectance Spectra of Ferrocyanides Nanoparticles; 2015 Fall Meeting of the Atomic Energy Society of Japan, Shizuoka, September 9-11, 2015, E26.

Yoshio Nakano, Kota Kawai, Makoto Nishikawa, Kenji Takeshita, Satoshi Komamine, Norio Kanehira: Basic research programs for the next generation vitrification technology (8) Dynamics of cold cap formation in vitrification process; 2015 Fall Meeting of the Atomic Energy Society of Japan, Shizuoka, September 9-11, 2015, F43.

Kota Kawai, Yoshio Nakano, Makoto Nishikawa, Kenji Takeshita, Satoshi Komamine, Norio Kanehira: Basic research programs for the next generation vitrification technology (9) Solubility and diffusion behavior of metal nitrates in borosilicate glass in cold-cap; 2015 Fall Meeting of the Atomic Energy Society of Japan, Shizuoka, September 9-11, 2015, F44.

Makoto Nishikawa, Kota Kawai, Yoshio Nakano, Kenji Takeshita, Satoshi Komamine, Norio Kanehira: Basic research programs for the next generation vitrification technology (10)Effect of borosilicate glass on thermal decomposition behavior of metal nitrates in vitrification process; 2015 Fall Meeting of the Atomic Energy Society of Japan, Shizuoka, September 9-11, 2015, F45.

Kenji Takeshita, Shunsuke Kozono, Yusuke Inaba: Basic Studies for Developing Rational Treatment and Disposal System of Radioactive Wastes Generated by Fukushima Dai-ichi Nuclear Accident (45)Tritium Recovery from Contaminated Water by Trickle-bed Type H2-H2O Chemical Exchange Process; 2015 Fall Meeting of the Atomic Energy Society of Japan, Shizuoka, September 9-11, 2015, I04.

Kenji Takeshita, Yusuke Inaba, Hideharu Takahashi, Jun Onoe, Hirokazu Narita: Development of Separation Process of PGMs and Mo from High - level Liquid Waste for the Stable Operation of Vitrification Process ; GLOBAL 2015 （21st International Conference & Exhibition: "Nuclear Fuel Cycle for a Low-Carbon Future"）, Paris, France, September 21-24, 2015, 5387.

Kota Kawai, Tatsuya Ffukuda, Yoshio Nakano, Kenji Takeshita, Yoshiyuki Miura, Norio Kanehira: Thermal decomposition analysis of simulated high-level liquid waste in cold-cap; GLOBAL 2015 （21st International Conference & Exhibition: "Nuclear Fuel Cycle for a Low-Carbon Future"）, Paris, France, September 21-24, 2015, 5161.

Koudai Mori, Shinya Ohashi, Tetsuo Kishi, Tetsuji Yano, Kenji Takeshita, Yoshiyuki Miura, Norio Kanehira: Evaluation of Precipitation/Crystallization Behaviors in Borosilicate Glasses Highly-Loaded with Pseudo High-Level Radioactive Waste Prepared by A New Combinatorial Method; 11th International Symposium on Crystallization in Glasses and Liquids (Crystallization 2015), Niigata, October 11-14, 2015.

Masahiko Nakase, Toru Kobayashi, Hideaki Shiwaku, Tsuyoshi Yaita, Kenji Takeshita: Relation between structure and coordination strength of lanthanide(III)-ligand complexes and size recognition; 2015 Annual Combined Meeting of Japan Society of Ion Exchange and Japan Association of Solvent Extraction, Ishikawa, October 23-24, 2015, SO-01.

Shinta Watanabe, Toshikazu Sato, Masato Nakaya, Jun Onoe, Tomoko Yoshida, Kenji Takeshita: Study on adsorption mechanism of metal ions on ferrocyanide nano particles (1) Spectroscopic analysis of chemical form of palladium in nitric acid aqueous solution; 2015 Annual Combined Meeting of Japan Society of Ion Exchange and Japan Association of Solvent Extraction, Ishikawa, October 23-24, 2015, IO-09.

Yuki Sawada, Shinta Watanabe, Masato Nakaya, Masahito Yoshino, Takanori Nagasaki, Tatsuya Kameyama, Tsukasa Torimoto, Jun Onoe, Yusuke Inaba, Hideharu Takahashi, Kenji Takeshita: Study on adsorption mechanism of metal ions on ferrocyanide nano particles (2) Ultraviolet-visible absorption spectrum analysis of ferrocyanide nano particles; 2015 Annual Combined Meeting of Japan Society of Ion Exchange and Japan Association of Solvent Extraction, Ishikawa, October 23-24, 2015, IO-10.

Yusuke Inaba, Hideharu Takahashi, Miki Harigai, Kenji Takeshita, Jun Onoe: Separation of Platinum-group Metals and Molybdenum from Simulated High-level Liquid Waste by Ferrocyanide Metal Compounds; 2015 Annual Combined Meeting of Japan Society of Ion Exchange and Japan Association of Solvent Extraction, Ishikawa, October 23-24, 2015, IO-14.

Takuya Kawamura, Kenji Takeshita: Adsorption and recovery of Soft metal ions by Chromatographic Agent coating Nitrogen-donor Ligand-NIPA-Gel with high Ligand content; 2015 Annual Combined Meeting of Japan Society of Ion Exchange and Japan Association of Solvent Extraction, Ishikawa, October 23-24, 2015, SP-18.

Michal CIBULA, Yusuke Inaba, Kenji Takeshita, Koichi Narita: Extraction of Pd(II) from Nitric Acid Solutions Using Thiodiglycolamides; 2015 Annual Combined Meeting of Japan Society of Ion Exchange and Japan Association of Solvent Extraction, Ishikawa, October 23-24, 2015, SP-28.

Yusuke Sakai, Keita Kanazawa, Yusuke Inaba, Kenji Takeshita: Adsorption of Cs by Porous Silica Coating Thin-film Polymer Gel with Prussian Blue; 2015 Annual Combined Meeting of Japan Society of Ion Exchange and Japan Association of Solvent Extraction, Ishikawa, October 23-24, 2015, IO-16.

J. Onoe, S. Watanabe, M. Nakaya, Y. Sawada, M. Yoshida, Y. Inaba, T. Nagasaki, H. Matsuda, H. Takahashi, K. Takeshita, T. Kameyama, T. Torimoto: Structural and electronic properties of Prussian blue nanoparticles used as an absorbent for disposal of high-level radioactive nuclear liquid wastes; 3rd Euro-Mediterranean Conference on Materials and Renewable Energis (EMCMRE-3), Marrakech, Morocco, November 2-6, 2015.

Shinya Ohashi, Koudai Mori, Yoshiaki Hiramatsu, Tetsuo Kishi, Daiki Atarashi, Tetsuji Yano, Kenji Takeshita, Yoshiyuki Miura, Norio Kanehira: Investigation of new borosilicate glass matrices with high loading capacity of high-level radioactive wastes by combinatorial method; The 56th Symposium on Glasses and Photonic Materials, Aichi, November 12-13, 2015.

Takuya Kawamura, Kenji Takeshita : Recovery of Soft metal ion in Nitric Acid Solution by Chromatographic Agent coated by TPEN-NIPA Copolymer Gel with High TPEN Content; ASNFC2015, Tokyo, December 2-4, 2015, 1B-14.

Yusuke Sakai, Keita Kanazawa, Yusuke Inaba, Kenji Takeshita: Adsorption of Cs by Porous Silica Coated with Thin - film Polymer Containing Iron(III) Ferrocyanide; ASNFC2015, Tokyo, December 2-4, 2015, 2A-21.

Xiangbiao Yin, Hideharu Takahashi, Miki Harigai, Kenji Takeshita : Desorption of Cesium from Vermiculite by Hydrothermal Process Using Sea Water; ASNFC2015, Tokyo, December 2-4, 2015, 2B-25.

Toshikazu Sato, Shinta Watanabe, Hirotaka Sawada, Makoto Nakatani, Masahito Yoshino, Takanori Nagasaki, Jun Onoe, Tomoko Yoshida, Kenji Takeshita: Chemical form of Pd ion in nitric acid: Analysis by UV-Vis/ XAFS spectroscopic and first-principles calculation; The 47th workshop of Atomic Energy Society of Japan Chubu Office, Aichi, December 9, 2015, 9p10.

Hirotaka Sawada, Shinta Watanabe, Makoto Nakatani, Masahito Yoshino, Takanori Nagasaki, Tatsuya Kameyama, Tsukasa Torimoto, Jun Onoe, Yusuke Inaba, Hideharu Takahashi, Kenji Takeshita, Hideki Masuda: Spectroscopic and theoretical analysis for structures and electronic state of ferrocyanide nanoparticles; The 47th workshop of Atomic Energy Society of Japan Chubu Office, Aichi, December 9, 2015, 9a09.

Yusuke Sakai, Keita Kanazawa, Yusuke Inaba, Kenji

Takeshita: Development of noble granulation method for Prussian Blue by thin-film gel coating method; The 11th seminar of The Reprocessing and Recycle Technology Division, Tokyo, December 11, 2015, 12-1.

Kota Kawai, Yoshio Nakano, Kenji Takeshita, Takayuki Nagai, Hidekazu Kobayashi, Ippei Amamoto, Yasuo Ayame: Elucidation for thermal decomposition behaviour of the high-level radioactive liquid waste; Effect on the thermal decomposition reaction of lanthanoid/alkali metal nitrates caused by ruthenium; The 11th seminar of The Reprocessing and Recycle Technology Division, Tokyo, December 11, 2015, 12-7.

Shunsuke Kozono, Kenji Takeshita, Yusuke Inaba: Recovery of Tritium from waste water generated by Fukushima NPP accident.; The 11th seminar of The Reprocessing and Recycle Technology Division, Tokyo, December 11, 2015, 12-8.

Takuya Kawamura, Kenji Takeshita: Sorption and Recovery of Soft-Metals (MA) using gelextraction method; The 11th seminar of The Reprocessing and Recycle Technology Division, Tokyo, December 11, 2015, 12-9.

M.Nakase, T.Kobayashi, K.Takeshita, H.Shiwaku, T.Yaita: Size recognition properties of multidentate N-donor ligands for f-series elemets; The International Chemical Congress of Pacific Basin Societies 2015, Honolulu, USA, December 15-20, 2015.

Masahiko Nakase, Toru Kobayashi, Kenji Takeshita, Tsuyoshi Yaita: Approach of gel-liquid extraction from solvent extraction toward the effective recognition and separation of f-elements; 2016 JAEA Synchrotron radiation symposium「New Developments in Synchrotron Radiation Science and Material Science」, Hyougo, Febrary 25-26, 2016, P25.

Toru Kobayashi, Masahiko Nakase, Shinichi Suzuki, Hideaki Shiwaku, Tsuyoshi Yaita: Ionic size recognition mechanism of 4f,5f-element by oxygen-nitrogen heterodonor ligand,; 2016 JAEA Synchrotron radiation symposium「New Developments in Synchrotron Radiation Science and Material Science」, Hyougo, Febrary 25-26, 2016, P22.

Kenji Takeshita, Shunsuke Kozono, Yusuke Inaba, Hideharu Takahashi: Recovery of Tritium from waste water by H2-H2O Hydrogen-isotope Exchange Process using trickle-bed reactor; The 14th research program of the Society of Isotope Science, Tokyo, March 11, 2016.

Kenji Takeshita, Yusuke Inaba, Hideharu Takahashi: Recovery of Tritium from Contaminated Water generated by Fukushima Daiich NPP Accident; The 81st Autumn Meeting of the Society of Chemical Engineers, Japan, Osaka, March 13-15, 2016, M320.

Kenji Takeshita, Hideharu Takahashi, Yusuke Inaba, Miki Harigai, Junichi Munasawa: Cleanup Technologies of Contaminated Soil generated by Fukushima Daiichi NPP Accident; The 81st Autumn Meeting of the Society of Chemical Engineers, Japan, Osaka, March 13-15, 2016, M319.

Yusuke Inaba, Miki Harigai, Hideharu Takahashi, Zou Yaolu, Kenji Takeshita, Junichi Munasawa: Volume reduction recovery of cesium by Prussian blue analogs; The 81st Autumn Meeting of the Society of Chemical Engineers, Japan, Osaka, March 13-15, 2016, H222.

Hideharu Takahashi, Yusuke Inaba, Miki Harigai, Junichi Munasawa, Kenji Takeshita: Development of Cs Recovery Process from Contaminated Soil Using Subcritical Water; The 81st Autumn Meeting of the Society of Chemical Engineers, Japan, Osaka, March 13-15, 2016, M317.

Takuya Kawamura, Kenji Takeshita: Separation and recovery of soft metal ion by Gel-liquid extraction using Chromatography; The 81st Autumn Meeting of the Society of Chemical Engineers, Japa Osaka, March 13-15, 2016, ZAA338.

Yusuke Sakai, Keita Kanazawa, Yusuke Inaba, Hiroshi Oaki, Kenji Takeshita: Adsorption of Cs by Iron(III) Ferrocyanide Granulated by Thin-film Gel Coating Method; The 81st Autumn Meeting of the Society of Chemical Engineers, Japan, Osaka, March 13-15, 2016, ZAA337.

Koudai Mori, Shinya Ohashi, Tetsuo Kishi, Tetsuji Yano, Kenji Takeshita, Yoshiyuki Miura, Norio Kanehira: Study of Al2O3/B2O3 ratio effect on a filling behavior of High-Level Radioactive Waste by Combinatorial Method; Annual Meeting 2016, The Ceramic Society of Japan, Tokyo, March 14-16, 2016, 1D23.

Shinta Watanabe, Hirotaka Sawada, Makoto Nakatani, Masahito Yoshino, Takanori Nagasaki, Tatsuya Kameyama, Tsukasa Torimoto, Jun Onoe, Yusuke Inaba, Hideharu Takahashi, Kenji Takeshita: The optical properties of ferrocyanaide nanoparticles used as an adsorbate for disposal of high-level radioactive nuclear waste liquids; The 96th Annual Meeting of The Chemical Society of Japan, Kyoto, March 24-27, 2016

Yusuke Inaba, Hideharu Takahashi, Miki Harigai, Zou Yaolu, Ria Mishima, Kenji Takeshita, Jun Onoe: Development of Recovery Process of Platinum-group Metals from HLLW for Stable Production and Volume Reduction of Homogeneous Vitrified Object(7) Absorption Study of Ferrocyanides for Separation of Platinum Group Metals and Molybdenum; 2016 Annual Meeting of the Atomic Energy Society of Japan, Sendai, March 26-28, 2016, 1G01.

Ippei Amamoto, Hidekazu Kobayashi, Yasuo Ayame, Takamitsu Ishidera, Kazuo Utsumi, Kenji Takeshita, Jun Onoe, Sachiko Nagayama, Yoshio Hasegawa: Development of Recovery Process of Platinum-group Metals from HLLW for Stable Production and Volume Reduction of Homogeneous Vitrified Object (8) Synthesis of ceramics support materials using some of the third period elements (Al and Si) and their sorption characteristics; 2016 Annual Meeting of the Atomic Energy Society of Japan, Sendai, March 26-28, 2016, 1G02.

Shinta Watanabe, Hirotaka Sawada, Toshikazu Sato, Makoto Nakatani, Masahito Yoshino, Tomoko Yoshida, Yusuke Inaba, Hideharu Takahashi, Kenji Takeshita, Jun Onoe: Development of Recovery Process of Platinum-group Metals from HLLW for Stable Production and Volume Reduction of Homogeneous Vitrified Object:(9) XAFS/UV-Vis spectroscopic and first-principles calculation studies both on the chemical form of Pd ion in nitric acid and on the adsorption of Pd ion to Prussian Blue nanoparticles; 2016 Annual Meeting of the Atomic Energy Society of Japan, Sendai, March 26-28, 2016, 1G03.

Makoto Nishikawa, Kota Kawai, Yoshio Nakano, Kenji Takeshita: Development of Recovery Process of Platinum-group Metals from HLLW for Stable Production and Volume Reduction of Homogeneous Vitrified Object (10) Visualization for solubility and diffusion behavior of simulated high-level liquid waste components into borosilicate glass; 2016 Annual Meeting of the Atomic Energy Society of Japan, Sendai, March 26-28, 2016, 1G04.

Michal Cibula, Yusuke Inaba, Kenji Takeshita, Koichi Narita: Development of Recovery Process of Platinum-group Metals from HLLW for Stable Production and Volume Reduction of Homogeneous Vitrified Object (11) Extraction of Platinum Group Metals from Nitric Acid Solutions Using Thiodiglycolamides (TDGA) and Tertiary Amines; 2016 Annual Meeting of the Atomic Energy Society of Japan, Sendai, March 26-28, 2016, 1G05.

Hideharu Takahashi, Yusuke Inaba, Miki Harigai, Junichi Munasawa, Kenji Takeshita: Development of Volume Reduction System of Cs Contaminated Soil - Overview of Fundamental Study from Separation to Vitrification -; 2016 Annual Meeting of the Atomic Energy Society of Japan, Sendai, March 26-28, 2016, 2F08.

Miki Harigai, Yusuke Inaba, Hideharu Takahashi, Kenji Takeshita, Junichi Munasawa: Preparation of Vitrified Glass for Cesium-Containing Metal Salt from Burning Material of Cs-Adsorbing Prussian Blue ; 2016 Annual Meeting of the Atomic Energy Society of Japan, Sendai, March 26-28, 2016, 2F09.

Toru Kobayashi, Masahiko Nakase, Shinichi Suzuki, Hideaki Shiwaku, Tsuyoshi Yaita: Ion size recognition mechanism of 4f, 5f-element by oxygen-nitrogen heterodonor ligand; 2016 Annual Meeting of the Atomic Energy Society of Japan, Sendai, March 26-28, 2016, 2F-17.

Takuya Kawamura, Kenji Takeshita: Separation and recovery of soft metal ions by Copolymer Gel-Silica Composite with High TPEN Content for Gel-liquid Extraction Process; 2016 Annual Meeting of the Atomic Energy Society of Japan, Sendai, March 26-28, 2016.

Xiangbiao Yin, Hideharu Takahashi, Miki Harigai, Kenji Takeshita: Desorption of Cesium Ions from Vermiculite with Sea Water by Hydrothermal Process; 2016 Annual Meeting of the Atomic Energy Society of Japan, Sendai, March 26-28, 2016.

Kota Kawai, Makoto Nishikawa, Yoshio Nakano, Kenji Takeshita, Yoshiyuki Miura, Norio Kanehira: Study on interactions between borosilicate glass and molybdenum contained in a high-level liquid waste; 2016 Annual Meeting of the Atomic Energy Society of Japan, Sendai, March 26-28, 2016, 1G15.

Shunsuke Kozono, Yusuke Inaba, Kenji Takeshita: Basic Studies for Developing Rational Treatment and Disposal System of Radioactive Wastes Generated by Fukushima Dai-ichi Nuclear Accident (52) Recovery of Tritium from Contaminated Water by Trickle-bed Reactor; 2016 Annual Meeting of the Atomic Energy Society of Japan, Sendai, March 26-28, 2016.

Kyohei Yoshinaga, Augusto Hernandez Solis, Henrik Sjöstrand, Kenji Takeshita: Development of thermal-hydraulic module of DONJON for BWR simulation; 2016 Annual Meeting of the Atomic Energy Society of Japan, Sendai, March 26-28, 2016.

Yoshio Nakano, Kota Kawai, Makoto Nishikawa, Kenji Takeshita, Satoshi Komamine, Norio Kanehira: Basic research programs for the next generation vitrification technology (8) Dynamics of cold cap formation in vitrification process; 2016 Annual Meeting of the Atomic Energy Society of Japan, Sendai, March 26-28, 2016.

BULLETIN OF THE
LABORATORY FOR ADVANCED NUCLEAR ENERGY

Vol.1 2016

平成29年２月　印刷

編集兼発行者　東京工業大学科学技術創成
研究院先導原子力研究所
責任者　矢野豊彦
〒152-8550 東京都目黒区大岡山2丁目12-1
電話　03－5734－3052
FAX　03－5734－2959

印刷所　昭和情報プロセス㈱
東京都港区三田５－14－９

Printed by
SHOWA JOHO PROCESS
Minato-ku, Tokyo, Japan